Moderate Temperature Synthetic Graphitization of Petroleum Coke with Magnesium and Raney Nickel Alloy

A Thesis Submitted to the Committee on Graduate Studies in Partial Fulfillment of the Requirement for the Degree of Master of Science in the Faculty of Arts and Science

TRENT UNIVERSITY

Peterborough, Ontario, Canada

Materials Science M.Sc. Graduate Program

January 202

Abstract

Moderate Temperature Synthetic Graphitization of Petroleum Coke with Magnesium and Raney Nickel Alloy

Nethma Dissanayake Mudiyanselage

Petroleum coke (petcoke) is a waste by-product of the upgrading process in the oil refining industry. It has limited utility in other areas of application.[1] High carbon content (over 85 wt.%), low ash content, and softness make petcoke a potentially valuable precursor for graphitization, where amorphous carbon can be transformed into graphitic carbon. The synthetic production of graphite is gaining more interest due to the increasing demand for battery materials.[2,3] Without metal moderators, achieving graphitization requires significantly high temperatures (> 2500 °C). Magnesium (Mg) has been identified as a promising reactant because of its efficacy in promoting graphitization and its relatively simple removal from the final product.[3–5] The optimized conditions of magnesium-assisted graphitization showed an electrical conductivity of (3552.0 ± 78.5) S/m at 10 mA. Furthermore, bimetallic metal mediators can exhibit improved catalytic activity in graphitization due to the synergistic effect.[3,6,7] Raney nickel alloy (Ni-Al alloy) contains 50 wt.% nickel and 50 wt.% aluminum. Individually, nickel and aluminum have shown efficacy in graphitization.[8] However, no research has been conducted on the efficacy of Raney nickel alloy as a metal mediator in petcoke graphitization.

We present our work on the graphitization of petcoke and its derived activated carbon using magnesium and Ni-Al alloy at 1000 °C and 1500 °C, respectively. This study assesses the effects of heating time, temperature, and precursor particle size on the degree of graphitization. Additionally, magnesium was completely removed after the graphitization process, and the residual Raney nickel alloy percentage was minimal.

Keywords

Petroleum coke, activated carbon, magnesium, Raney nickel alloy, synthetic graphitization

Acknowledgements

First and foremost, I sincerely thank my supervisor, Professor Andrew Vreugdenhil, for his unwavering guidance, kindness, and faith in my work. His advice and feedback have been invaluable, and working under his supervision has greatly shaped this journey. I am especially grateful for his understanding and tremendous support in helping me overcome the challenges I faced as an international student.

I also wish to thank my thesis committee members, Professor Brad Easton and Professor Carlo Bradac, for their time, valuable feedback, and contributions that greatly enhanced this research.

My colleagues at Trent Inorganic Materials Research Laboratory (IMRL) made this journey more enjoyable through their friendship, collaboration, and inspiring discussions. I am grateful to our lab manager, Oliver Strong, for his unwavering support in maintaining a positive laboratory environment. I also thank my lab peers, Teagan Carr, Kyle Reyes, Tylor Roy, Hamant France, Anjali, and Liam Gillett for fostering such a welcoming and peaceful atmosphere. Additionally, I would like to thank Paul Pede from Carbonix Inc. for his support throughout my research.

I sincerely thank Reza Alipour and Elmira Nazari in the Electrochemical Materials Lab at Ontario Tech University, led by Prof. Brad Easton, for their help with characterizations and valuable discussions. I also appreciate Shaheen Akhtar from the PowerGeolab at Trent University for generously supporting the use of their instruments. Additionally, I want to thank Assistant Professor Huy Dang for providing access to the SEM and Queen's University for their support with TEM analysis.

To my family, I am eternally grateful for your love, patience, and encouragement. My parents and brother have been my constant strength, and I dedicate this achievement to you. Your blessings from thousands of miles away strengthened me to stay focused despite the burden of homesickness.

To my love, Lalendra—your unwavering support, patience, and belief in me have been my greatest anchor. This achievement is as much yours as it is mine. Thank you for dedicating yourself to my dreams and creating a space of comfort, both emotionally and financially.

Finally, to everyone who has contributed in big or small ways—thank you. Your support has meant the world to me.

Contents

List of Figures

List of Tables

List of Equations

List of Abbreviations and Symbols

List of Abbreviations

Petcoke	Petroleum coke
AC	Activated carbon
Mg	Magnesium
RNi	Raney nickel
MgPC	Graphitized petcoke with magnesium
MgAC	Graphitized activated carbon with magnesium
RNi AC	Graphitized activated carbon with Raney nickel alloy
SEM	Scanning electron microscope
XRD	X-ray diffraction
XPS	X-ray photoelectron spectroscopy
TEM	Transmission electron microscopy
2D	Two-dimensional / a peak labelled in Raman spectroscopy
Fe	Iron
Co	Cobalt
Ni	Nickel
Ca	Calcium
V	Vanadium
Mo	Molybdenum
W	Tungsten
Be	Beryllium
Cu	Copper
Zn	Zinc
Cr	Chrominum
Ga	Gallium
Zr	Zirconium
Ag	Silver
Pt	Platinum
Si	Silicon
P	Phosphorus
S	Sulfur
La	Lanthanum
Ce	Cerium
Pr	Prseodymium
Wt%	Weight percentage
FWHM	The full width at half maximum
G%	Graphite percentage
I_D/I_G	Intensity ratio of D peak and G peak in Raman spectroscopy
BSE	Backscattered electrons
SE	Secondary electrons
ET detector	Everhart–Thornley detector
MT	Metric Ton
IUPAC	International Union of Pure and Applied Chemistry
ICP-OES	Inductively Coupled Plasma Optical Emission spectroscopy

CMC	Sodium carboxymethyl cellulose
NIST	National Institute of Standards and Technology
CNTs	Carbon nanotubes
Atomic%	Atomic percentage

List of Symbols

σ	Sigma
$\boldsymbol{d_{002}}$	d-spacing between two stacked layers in graphite
°C	Degrees of Celsius
Å	Angstrom
α	Alpha
β	Beta
Θ	Angle of incidence
$\boldsymbol{\lambda}$	Wavelength of the X-rays
$\boldsymbol{n}$	An integer representing the order of diffraction
$\mathbf{L_c}$	The crystallite height of graphite
$\mathbf{L_a}$	The crystallite width of graphite
K	A predetermined scale factor
ρ	Resistivity
V	Voltage
$\boldsymbol{\pi}$	~3.14
I	Current
σ	Conductivity
P	Pressure
Pa	Pascal
hυ	The energy of the photon
$\mathbf{E_b}$	The binding energy of the electron to the atom
$\mathbf{E_{res}}$	The kinetic energy of the released electron
Ø	The amount of thermodynamic work required to remove an electron from the surface of a material
psi	Pound per square
°	Degrees
$\mathbf{T_m}$	Melting point
S	Conductance

1. Introduction

1.1. Graphite

Graphite is a carbon allotrope characterized by a crystalline structure composed of stacked two-dimensional graphene layers. These carbon atoms exhibit sp^2 hybridization, which influences the in-plane electrical conductivity of graphite. Graphene layers are bound via weak Van der Waals forces, allowing them to slide easily over one another. Each atom bonds to three neighbors through strong covalent σ-bonds.[9–13]

The 2H polytype, which is the most common form of graphite, has a hexagonal stacking pattern of ABAB (Figure 1.1a). The layer spacing in this structure is approximately 0.335 nm, and the distance between adjacent carbon atoms is about 0.142 nm. The unit cell parameters for ideal hexagonal graphite are typically given as a=2.456 Å and c=6.696 Å.[14] Rhombohedral graphite (Figure 1.1b), also known as the 3R polytype, is a less common variation that stacks in an ABCABC pattern.[3,15,16] This form is less thermodynamically stable and is believed to be a stacking fault in the hexagonal structure. When heated above 1600 °C or subjected to specific processing conditions, it tends to revert to the more stable ABAB stacking and usually coexists with hexagonal graphite.[17]

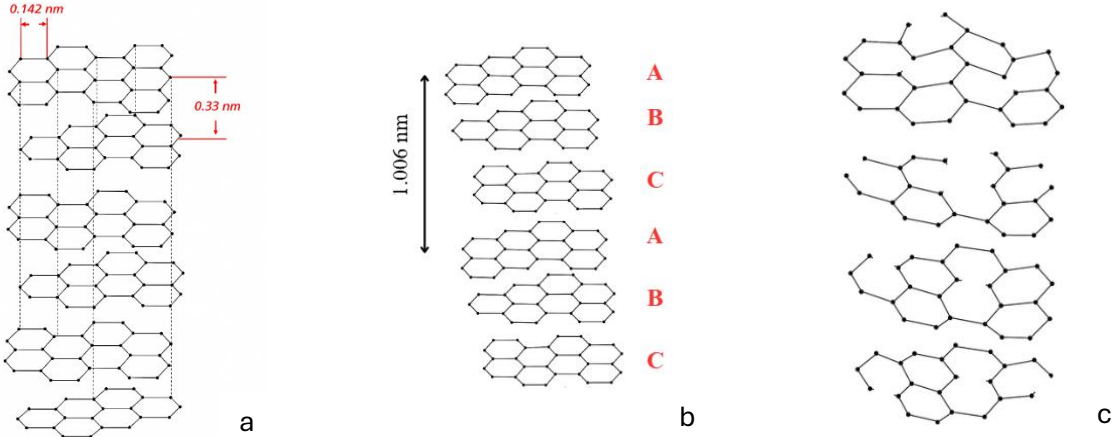

Figure 1.1: Schematic illustration of a) ABAB, b) ABCABC, and c) turbostratic graphite structure

Strong covalent bonds within each graphene sheet and relatively weak van der Waals interactions between adjacent layers define graphite's layered structure. The material can undergo structural changes along its basal planes due to variations in bonding strength. Turbostratic graphite (Figure 1.1c), a disordered variant of the typical hexagonal form, exemplifies a modified structure.

The graphene layers in both turbostratic and hexagonal graphite maintain a consistent interlayer spacing. However, the main difference lies in their stacking arrangement. Turbostratic graphite is characterized by random translational and rotational misalignments between layers, while hexagonal graphite exhibits a well-ordered ABAB stacking pattern. These periodicity disruptions cause irregularities in the interlayer spacing and eliminate long-range order.

Experimental findings indicate that turbostratic graphite can exhibit localized changes in layer spacing and curvature. Its broader range of interlayer distances, usually measured by X-ray diffraction (XRD) between 0.3400 nm and 0.3440 nm, results from these features. In contrast, ideal hexagonal graphite displays a more uniform spacing of about 0.3354 nm.[3,17,18] It is crucial to understand that the interlayer spacing determined by XRD is an average value influenced by the sample's degree of conversion between turbostratic and hexagonal domains.[14]

Although its structure is idealized, real graphite often contains defects such as vacancies, stacking faults, and disclinations. These imperfections, along with trace impurities such as hydrogen and oxygen, can significantly impact its chemical reactivity and performance in various applications.[3,14,19,20]

Graphite exists in both natural and synthetic forms, differing in structure and properties. Natural graphite is mined from deposits using standard methods, while synthetic graphite is produced by graphitizing carbon-rich materials such as petcoke, coal tar, hydrocarbons, and wood.[1,2,21,22] China, India, Brazil, Sri Lanka, and Madagascar are among the major producers of natural graphite. The growing demand from the battery industry significantly increases the production of synthetic graphite.[10,22]

Our work includes a metal-assisted graphitization process for producing synthetic graphite, which will be comprehensively discussed in the following sections.

1.2. Synthetic Graphitization

1.2.1. Conventional synthetic graphitization

Synthetic graphite is typically produced through graphitization, a heat treatment that transforms amorphous carbon (Figure 1.2 c) into a more ordered structure.[23] This process takes place in an inert environment, where carbonaceous precursors are heated to high temperatures (2500 - 3000) °C. Before graphitization, organic materials undergo a pre-carbonization step to decompose non-carbon elements, during which the organic precursor is heated in an inert environment to about 1300 °C (pyrolysis).[2,3,24,25] The working temperature is gradually increased to reach a specific graphitization level, at which the sample is held for a set period. Turbostratic graphite (Figure 1.2b) generally begins to form at 1800 °C, creating small crystallites within the carbon material. Turbostratic carbon contains stacked graphene layers that closely resemble pristine graphite. However, these crystalline domains can either be randomly oriented around the normal (aligned along different axes) or show short-range structural organization.[3]

Consequently, turbostratic graphite exhibits a greater interlayer spacing and a smaller in-plane crystallite size compared to ordered graphite (Figure 1.2a). The process of converting turbostratic graphite to pristine graphite is expected to begin above 2000 °C in conventional graphitization, where graphene 2D planes become perfectly aligned and stacked layer by layer. The degree of graphitization is mainly controlled by the dwell time, working temperature, and the type of carbon precursor. Additionally, this process removes contaminants such as sulfur and hydrogen from the carbon precursor at around 1200 °C to 1300 °C, which helps produce pure graphite.[3,14,19]

Traditional metal-free graphitization can take weeks to convert amorphous carbon into crystalline carbon.[26] Metals can decrease the graphitization temperature and time by forming intermediate carbon-metal bonds or by dissolving carbon in the molten metal, which facilitates the reorganization of carbon atoms in a crystalline manner.[2,3,24,25]

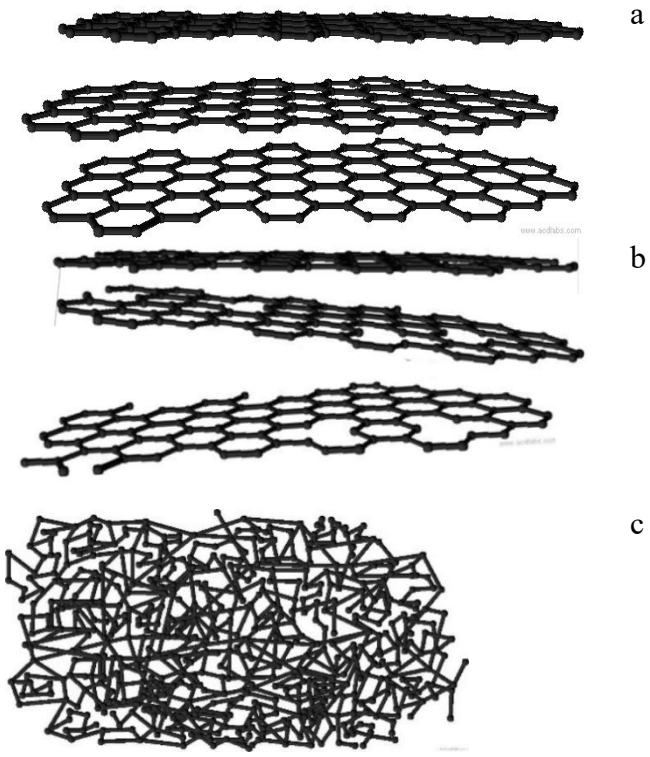

Figure 1.2: Schematic diagram of a) ordered graphite, b) turbostratic, c) amorphous carbon.

1.2.2. Metal-assisted synthetic graphitization

Metals are used in synthetic graphitization to facilitate the conversion of disordered carbon atoms into the highly ordered structure of graphite. Without metal mediators, the process requires extremely high temperatures (>2500 °C)[19] and energy, which increases the cost of scaling up.[27–29]

Graphitization with metal reactants is affected by several factors, including the type of carbon precursor, particle size, the ratio of carbon to metal, the metal's speciation (such as pure element, chloride, oxide, etc.), mixing processes, and graphitizing temperature.[3,29] The impact of IV−VIII transitional metals on the graphitization process has been extensively studied[26,30] notably using iron (Fe),[14,18,19,30–35] cobalt (Co),[29] and nickel (Ni)[6,27–29,36–38] elements and their dissolved solutions or oxides.

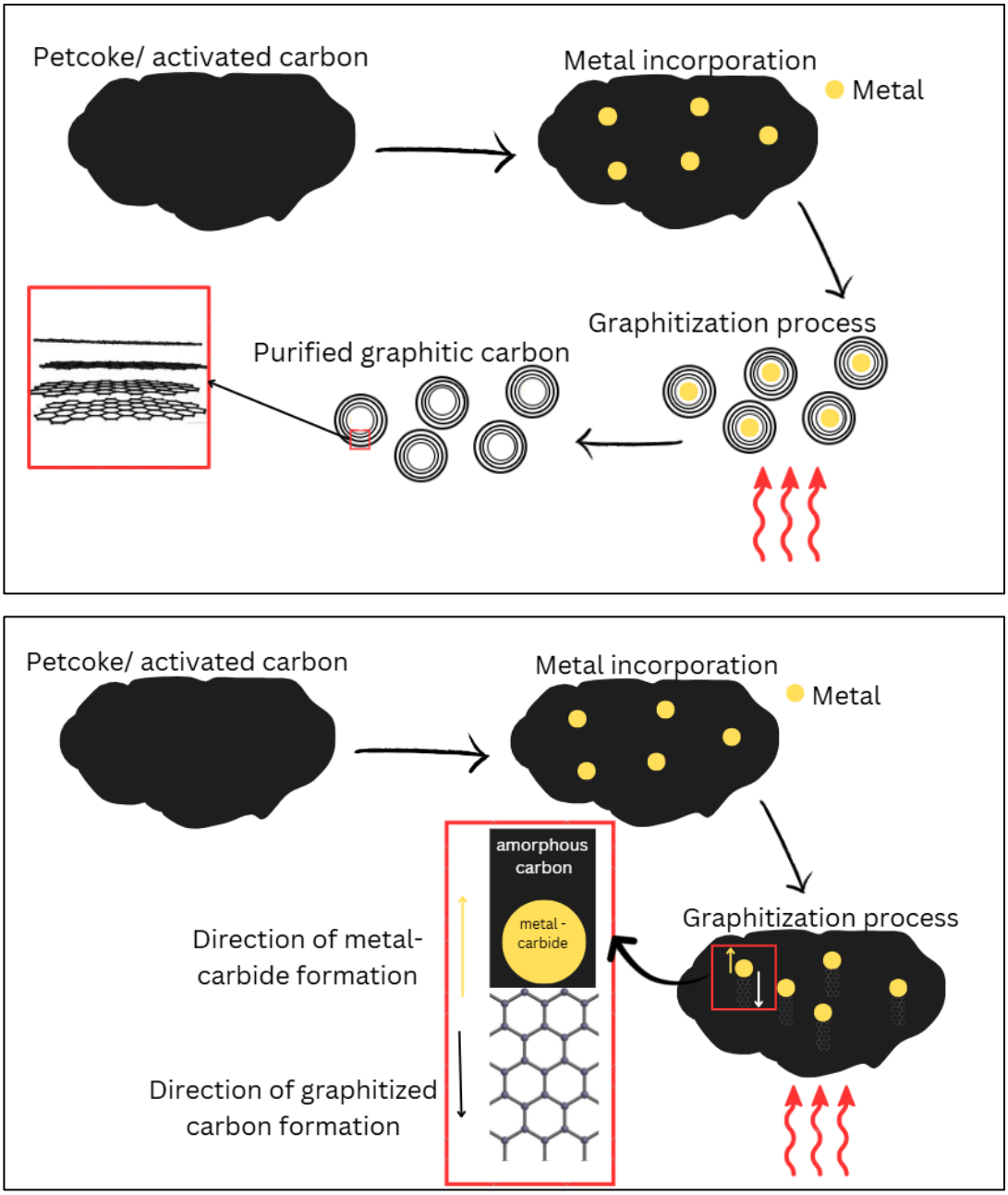

Figure 1.3: Schematic diagrams of a) carbon dissolution precipitate mechanism and b) formation of intermediate carbon-metal bonds mechanism, adapted from the graphical abstract of Reference[21] and Figure 5 in Reference.[24]

In 1978, Asao-Ya and Sugio-Tani suggested that graphitization involving late transitional metals occurs through the carbon dissolution and precipitate mechanism, while elements such as calcium

(Ca), vanadium (V), molybdenum (Mo), and tungsten (W) display carbide formation and decomposition mechanism.[19] However, transition metals do not strictly follow the above process.[21]

Aurora Gomez-Martin et al. explained two types of metallic graphitization processes of iron, based on the temperature range used. They suggested that the carbon dissolution precipitate mechanism governs the graphitization at higher temperatures (above their melting point), where carbon is precipitated in an orderly manner due to the supersaturation of carbon in molten iron (Figure 1.3a). In this scenario, molten metal acts like a solvent, dissolving carbon into solution. When the molten metal becomes saturated with carbon, it begins to precipitate carbon crystals more systematically. This mechanism is effective because it facilitates carbon atoms to rearrange themselves with less energy, forming graphitic layers as carbon leaves the metal matrix.[19,30,31] On the other hand, the carbide formation-decomposition mechanism dominates at lower temperatures. In the carbide decomposition process, metal-carbide liquid droplets (e.g., Fe_xC_y) dissolve amorphous carbon structures (Figure 1.3b).[31]Here, metal atoms react with carbon to form metal carbides (e.g., Fe_xC_y), which then serve as intermediates. These carbide phases break down the disordered carbon structure and guide its reassembly into graphitic domains. The transition from amorphous carbon to crystalline graphite results in a decrease in the system's free energy. Consequently, the process of graphitization is driven by the lower free energy of crystalline carbon.[3,29] Additionally, both mechanisms can potentially coexist within the same carbon-metal system.[5]

After the graphitization process, the metal should be removable,[3] and recoverable for practical use. Previous research has pointed out the challenges of removing transition metal mediators, especially iron, which is very difficult to extract after use.[14,17–19,30–33,39]

1.2.3. Metallic and non-metallic mediators used in graphitization

Certain metals can effectively reduce the energy input required for graphitization to as low as 600 °C for non-graphitizable precursors.[39] A wide variety of chemical species, including elemental metals, alloys, metal oxides, salts, and organometallic compounds, are used as catalysts in graphitization. However, early research mainly focused on elemental catalysts.[24,27,36] Zhao et al. provided a thorough overview of metal mediators used in graphitization up to 2018.[41] Building on their work, I've updated Table 1.1 to include recent studies.

Table 1.1: Metal mediators used in graphitization, organized in the format of an incomplete periodic table.

Ia	IIa											IIIa	IVa	Va	VIa
Li	Be											B	C	N	O
	42											43–45			
Na	Mg											Al	Si	P	S
46,47	3,20,48–51	IIIb	IVb	Vb	VIb	VIIb		VIIIb		Ib	IIb	42,48,52	53–55	56	57
K	Ca	Sc	Ti	V	Cr	Mn	Fe	Co	Ni	Cu	Zn	Ga	Ge	As	Sn
	58–60		53,61–63	64, 65	63	66,67	14,18, 19,24, 30–35,63, 66,68–70	39, 71–76	6,8,16,36 – 39,62,63, 66,72–74,77,78	63	79, 80	81			
Rb	Sr	Y	Zr	Nb	Mo	Tc	Ru	Rh	Pd	Ag	Cd	In	Sn	Sb	Te
			54,61, 82–84		16,61 ,84,85					86					
Cs	Ba	La-Lu	Hf	Ta	W	Re	Os	Iy	Pt	Au	Hg	Tl	Pb	Bi	Po
					62				62						

La	Ce	Pr
88,89	88	88,90,91

The graphitization process of carbon materials is being studied for various substances that could serve as catalysts. The catalysts examined include alkali metals such as sodium (Na), alkaline earth metals like magnesium (Mg), beryllium (Be), and calcium (Ca), as well as transition metals such as iron (Fe), cobalt (Co), nickel (Ni), copper (Cu), zinc (Zn), vanadium (V), chromium (Cr), manganese (Mn), gallium (Ga), zirconium (Zr), molybdenum (Mo), silver (Ag), tungsten (W), and

platinum (Pt). Research on non-metallic and metalloid materials for graphitization includes silicon (Si), phosphorus (P), and sulfur (S). Researchers are also exploring light rare earth elements, including lanthanum (La), cerium (Ce), and praseodymium (Pr) for their potential as catalysts. The requirements for precursors and carbon structures influence how these metals and non-metals are applied, whether as elemental powders, oxides, carbides, sulfates, or alloys. Graphitization processes involving simultaneous dissolution-precipitation and carbide formation-decomposition reactions improve crystallinity and promote faster carbon reorganization, as described previously in the literature.[24,31,41]

Transition metals, especially iron (Fe), cobalt (Co), and nickel (Ni), continue to show the highest preference for acting as graphitization catalysts according to available research. Graphitization process operates between 800 °C[92] and 1800 °C,[41] although high crystallinity demands may need temperatures as high as 2800 °C.[93] The synergistic effects of multi-metal systems have attracted significant attention. Combinations such as Fe-Co-Ni,[73] Ni–Mo,[16] and Fe-Co[93] outperform individual metal systems by providing better catalysis, which leads to lower-temperature graphitization and more ordered carbon structures.

A few research projects used silicon (Si) as a catalyst for graphitization by converting it into silicon carbide (SiC) through a carbide formation-decomposition process. This process requires extremely high temperatures of 2700 °C for SiC to break down before transforming into a graphitic form.[53,54] The process requires higher temperatures than most transition metals, making it less suitable for moderate temperature applications.

The degree of graphitization depends on the specific application requirements, balancing high conductivity with structural integrity and thermal stability. Various research studies provide both qualitative and quantitative evidence of the catalytic properties of metallic and non-metallic elements. A detailed comparative assessment of each catalyst is necessary to determine their efficacy in achieving complete graphitization.

The graphitization of carbon precursors at high temperatures can potentially occur without the need for catalysts,[53,54] raising questions about whether certain elements genuinely serve as catalysts or merely occur alongside thermal effects. Our investigation of Raney nickel alloy and magnesium (Mg) as metal mediators in our graphitization process assessed both elemental and bimetallic systems to understand their role in graphitization under controlled conditions.

1.2.3.1. Magnesium

Magnesium is a readily used alkaline earth metal in chemistry, with a relatively low melting point of 650 °C.[11] The lower melting point of magnesium could lead to lower graphitization temperatures, as molten magnesium promotes the dissolution and precipitation of carbon. Compared to group VIII transition metals, only a few studies have used magnesium in carbon graphitization. Zhao, L. et al. demonstrated the potential for removing magnesium after graphitization of various precursors. They targeted applications in lithium-ion batteries by achieving a high degree of graphitization at 1000 °C using glucose as the carbon precursor. Both XRD and Raman analyses revealed structural characteristics similar to those of commercial graphite after 20 hours of graphitization. The catalytic role of magnesium in significantly lowering the energy barrier for graphitization is demonstrated by the fact that, without magnesium, the same glucose-based sample required temperatures as high as 2850 °C to achieve comparable graphitic properties.[12] In their subsequent research, they attempted to graphitize hard carbon using magnesium vapor, but the vapor did not prove as effective as magnesium metal powder.[3]

Fu Yang et al. introduced magnesium as a metal mediator to graphitize anthracite coal.[5] Magnesium alters the surface morphology of carbon during the graphitization process while increasing the degree of graphitization at a specific metal-to-carbon precursor ratio of 1:1 by weight ratio.[94] At 1100 °C, the highest graphitic properties were observed. Two hours were chosen as the dwell time for the entire graphitization process. However, according to Raman and XRD analysis, the use of magnesium did not significantly improve the level of graphitization, unlike glucose.[41] The shorter dwell time could be one reason. Additionally, since 1100 °C is slightly above magnesium's boiling point (1091 °C), a decrease in magnesium might affect the effectiveness of graphitization. Importantly, they observed that impurities in the precursor caused MgO to form during the graphitization process.[25] Interestingly, M. H. RuÈmmeli et al. observed that surface defects in metal oxides, which serve as nucleation sites for carbon layers similar to those found in magnesium oxide (MgO) nano powders, promote the growth of graphitic carbon during chemical vapor deposition (CVD). This aligns with the broader mechanism in which, even without metal catalysts, oxide surfaces, especially those with imperfections, actively facilitate the formation of ordered carbon structures.[95] Zhang, C. et al. reported similar observations. Magnesium citrate graphitizing coal tar pitch exhibited a slight improvement in graphitization at 900 °C over 2 hours. [20] Interestingly, studies consistently report that magnesium is much easier to remove after

graphitization than transition metals, which makes post-treatment / purification simpler and straightforward.[40]

The graphitization of petcoke using magnesium as the metal reactant has not been explored previously according to the existing literature.

1.2.3.2. Raney nickel alloy

The Raney nickel alloy contains 50 wt.% nickel and 50 wt.% aluminum, making it a potential bimetallic mediator for graphitization.[6,35,37] Nickel has demonstrated its efficacy in the graphitization process of amorphous carbon[6,8,35–38] while aluminum has been used less often in graphitization.[41,51,80] Recent studies demonstrated the improved performance of multi-metallic mediators in graphitization.[91] When used in graphitization, the Ni–Al alloy can function as a bimetallic catalyst. This alloy usually contains a heterogeneous mixture of intermetallic phases in its as-cast form, such as Al_3Ni, Al_3Ni_2, AlNi, and Al-Al_3Ni eutectic structures.[76] When added to alloy systems, nickel exhibits increased catalytic activity for graphitization, possibly due to synergistic interactions and improved carbon solubility.[36]

Based on the synergistic effect of nickel and aluminum's catalytic activity, it is hypothesized that a nickel–aluminum alloy (Ni-Al) could enhance the graphitization of petroleum coke. According to existing literature, no studies have specifically investigated the use of Raney nickel alloy in graphitization, making this a novel approach worthy of exploration.

1.2.4. Microwave graphitization

Microwaves operate within electromagnetic radiation frequencies from 300 MHz to 30 GHz. Energy transfer occurs through electromagnetic waves instead of traditional methods such as conduction or convection. This process results in volumetric heating, where energy is absorbed directly by the material, causing a rapid increase in temperature. The authors compare this to conventional heating methods, noting that microwaves can heat materials like food or carbon much faster because they penetrate and excite molecules internally rather than just at the surface.[96–107]

Microwave-assisted graphitization has emerged as a promising alternative, offering rapid volumetric heating, reduced energy consumption, and shorter reaction times. The microwave irradiation process interacts directly with carbon materials, creating localized heating that speeds up the transformation process. Microwave heating works through dipolar polarization and ionic

conduction mechanisms, which differ significantly from traditional thermal conduction.[98,104,108,109] Studies have shown that the graphitization process takes place at lower temperatures and shorter durations when microwave heating is combined with transition metal catalysts like nickel, cobalt, and iron.[96,101] The microwave ON/OFF heating cycles provide additional benefits to catalytic graphitization because they facilitate multiple dissolution-precipitation cycles that promote the rapid formation of ordered carbon structures.[101]

The effectiveness of microwave graphitization has been shown across different carbon sources, including activated carbon,[96] coal-derived carbon,[98] and graphite mineral resources.[104,105] Ji et al. (2022) used fir wood to produce carbon materials while achieving better graphitic structures through CoFe and NiFe alloy incorporation. The microwave absorption, along with the dielectric properties during the graphitization process, increased as the graphite content increased without needing metal addition.[99] Głowniak et al. (2021) researched microwave-based nanoporous carbon synthesis while demonstrating that metal-free graphitization works with precursors containing inorganic salts or through chemical activation (e.g., KOH-based).[97]

Transition metals are crucial in catalyzing graphitization under microwave conditions. Nickel is a commonly used catalyst in microwave graphitization across various studies. Joni et al. (2018) achieved 98% graphitization of carbon through nickel sulfate treatment during five minutes of microwave exposure. The analysis of XRD and Raman data showed highly crystalline graphite formation, which resulted in performance comparable to commercial graphite.[105] Microwave-assisted graphitization using Co, Fe, Ni, and Cr salts has also been studied, although these metals demonstrated lower catalytic efficiency compared to the pure elements. The microwave-based graphitization methods using these salts demonstrated reduced efficiency as catalysts compared to their elemental forms. Additionally, the presence of remaining oxides and incomplete graphitization limited their overall operational capabilities.[105]

Future research should aim to optimize precursor design, select appropriate catalysts, and tailor microwave parameters to develop carbon materials for specific applications.[96,98,104,105] The investigation of magnesium as a metal mediator in microwave-assisted graphitization could yield important results because there is limited research on this topic in the current literature.

1.3. Petroleum coke (Petcoke)

Petcoke is a solid with a high carbon content (>85 wt.%) that is produced as a byproduct during oil refining. Its composition also includes sulfur (5-7 wt.%), oxygen, hydrogen (~3.5 wt.%), nitrogen (0.2-1.5 wt.%), and other minor elements, depending on the refinery process.[3] At ambient temperature, petcoke remains inactive, while the crystallite size increases at higher temperatures (~ 1400 °C), driven by the increased thermodynamic stability of larger crystallites.[13] Petcoke is an amorphous, soft, graphitizable carbon that consists of small crystals roughly aligned in parallel (isotropic), which assists the graphitization process. In non-graphitizing, hard carbon, these grains are randomly oriented (anisotropic).[17,23,30] Petcoke is heated to over 2500 °C in an inert environment, transforming amorphous carbon into a crystalline structure. Notably, petcoke does not require a pre-pyrolysis process due to its high carbon content. Figure 1.4 illustrates the structural arrangement of both graphitizing (Figure 1.4a) and non-graphitizing (Figure 1.4b) forms of carbon.

Figure 1.4: Schematic diagrams of (a) graphitizing and (b) non-graphitizing carbons.

Previous work in our research group revealed that sulfur removal from petcoke is not effective using only chemical or heat treatment. Oliver K.L. Strong et al. investigated the potential of pre-activation treatment of petcoke with KOH followed by an acid wash, which has significant potential to remove a considerable amount of sulfur from petcoke.[3] Therefore, activated carbon derived from petcoke was also used in this study to compare the efficacy of graphitization with raw petcoke and purified petcoke.

1.4. Motivation

Transition metals, including iron (Fe), demonstrate effective catalytic properties that enhance graphitization efficiency, as reported in research findings.[14,17–19,24,30–33] However, their practical use is often limited by the challenge of removing residual metal particles from the final graphite

product.[14] The purity level and scalability, along with downstream processing, become challenging because high-purity graphite requirements remain unfulfilled.

Research needs to identify catalyst alternatives that deliver equivalent outcomes and simple methods for metal extraction. The potential of magnesium as a graphitization catalyst has attracted recent interest, but its efficacy on different precursors remains largely unexplored.[3,20,49,50] Notably, Zhao et al. (2017) researched magnesium removal from glucose-derived carbon systems after graphitization to produce high-purity graphite in their study.[3] Building on this insight, our work hypothesized that magnesium could improve graphitization levels at moderate temperatures by adding it to activated carbon or petroleum coke precursors. The research aims to develop a practical method for producing high-purity graphite through effective magnesium removal, which addresses the main challenge associated with iron-based transition metal catalysts.

Magnesium is a single-metal mediator that could be potentially utilized in the graphitization of petroleum coke and activated carbon. Research demonstrates that synthetic graphitization becomes more efficient with multi-metallic systems.[16,85] Building on this insight, we identified Raney nickel alloy as an unexplored metal mediator for graphite synthesis. Composed of aluminum and nickel in a 1:1 ratio, Raney nickel alloy offers the synergistic effect of two metals that have independently demonstrated strong catalytic potential in graphitization processes.[76,109,110]

Our research aims to explore the potential synergistic effects of the Al-Ni alloy during graphitization, with a specific focus on its performance and ease of post-treatment removal. Raney nickel acts as a catalyst in hydrogenation reactions due to its widespread use in the field.[111] Research on its initial alloy under graphitization conditions will open opportunities to improve metal-assisted transformations of petroleum coke and other carbon-rich materials into graphite.

This thesis explores the efficacy of magnesium and Raney nickel alloy in the graphitization of petroleum coke and activated carbon, as well as their removal efficiency after the graphitization process. Chapter 2 provides a comprehensive discussion of the characterization techniques employed in this investigation. Chapter 3 investigates the efficacy of magnesium in graphitizing petcoke and activated carbon under various processing conditions. Chapter 4 explores the graphitization effects of Raney nickel alloy on activated carbon. Chapter 5 provides a comprehensive analysis of the removability of magnesium and Raney nickel alloy following the graphitization process.

1.5. Thesis objectives

1. Investigate the influence of monometallic and bimetallic mediators in graphitization and optimize process parameters.
2. Evaluate the morphological and structural properties of graphitized activated carbon derived from petcoke.
3. Optimize the metal removal in the post-graphitization process.

2. Experimental Techniques

2.1. X-ray diffraction (XRD)

X-ray diffraction (XRD) crystallography provides crucial details for understanding material structures. The scattered beams create interference patterns that form a diffraction pattern. The main function of XRD involves directing an X-ray beam at the sample and measuring the angles and intensities of the diffraction rays. Analyzing XRD data reveals detailed information about the material's structure by indicating both crystallinity levels and interlayer distances.[112]

The widespread use of X-rays as radiation sources exists because they offer affordable access to high-flux production. The scattering process exhibits both elastic and coherent features. The material's atomic density or Fourier-transformed charge density becomes visible through the diffraction pattern. The diffraction technique is effective for analyzing single-crystal materials, polycrystalline materials, thin films, and amorphous materials. The method operates without damaging the material (non-destructive) while providing precise information about the entire structure.[113]

The X-ray diffractometer has three main parts: a radiation source, a sample stage in a sealed environment, and a detector. A sealed diode vacuum tube generates X-rays by colliding high-speed electrons with a heavy metal target made of copper (Cu). The tungsten filament, called the cathode, produces electrons that gain high-speed energy through a strong voltage before striking the copper target, or anode. Beryllium is used for X-ray diffraction sample windows because it offers low attenuation while remaining solid and transparent.[113,114]

The collision between an energetic electron and a copper atom results in the ejection of an electron from the K shell, creating a vacancy. This innermost shell vacancy is usually filled by electrons moving from the outer L or M shells. The energy transition of electrons to lower states produces X-ray photons with distinct energies, known as characteristic X-rays. The wavelength of these X-rays is specifically calculated using the wavelength-energy equation 2.1.

Equation 2.1: The wavelength-energy equation

$$\lambda = \frac{hc}{\Delta E}$$

The Planck constant (h), vacuum speed of light (c), and energy difference (ΔE) between states define this equation. The copper target produces X-rays, which include $K_{\alpha 1}$ and $K_{\alpha 2}$ lines from the L shell at 1.54051 Å and 1.54433 Å wavelengths, along with K_{β} from the M shell at 1.39 Å. The K_{β} radiation is eliminated using a monochromator or a nickel film filter, while software corrections remove the $K_{\alpha 2}$ radiation.

Bragg's law: the X-rays diffract constructively according to Equation 2.2. When they hit a crystal lattice at a particular angle, the path length difference between adjacent crystal planes equals an integer multiple of the X-ray wavelength.[113,115–117]

Equation 2.2: Bragg's law:

$$2dsin\Theta = n\lambda$$

Where d is the spacing between crystal planes, θ is the angle of incidence, λ is the wavelength of the X-rays, and n is an integer representing the order of diffraction. Figure 2.1 depicts a constructive diffraction of X-rays obeying Bragg's law.

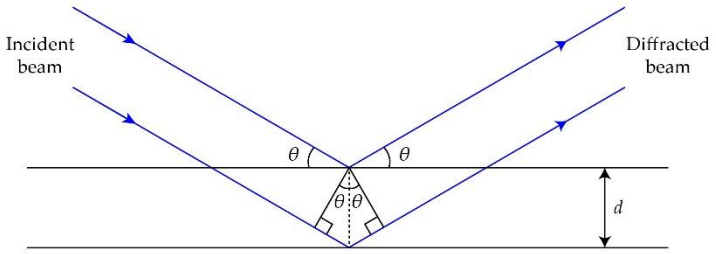

Figure 2.1: Constructive diffraction associated with Bragg's law.

The d-spacings of a crystal can be calculated using Miller indices. Single crystals exhibit one diffraction angle, while powders are diffracted at various angles, producing a ring of scattering. The width of the diffraction peaks reflects the quality of the crystal's crystallinity. For example, the spectrum of an ideal crystal shows only one vertical line. Non-ideal crystals display a broader single peak, whereas polycrystalline crystals produce a series of peaks that often overlap.[116]

In the context of interpreting the XRD spectrum of graphite, the (002) peak indicates diffraction from stacked graphene planes that are parallel to each other along the C-axis. The sharp (100)

small peak is also present in the XRD spectrum of graphite, reflecting the in-plane atomic structure of graphene.

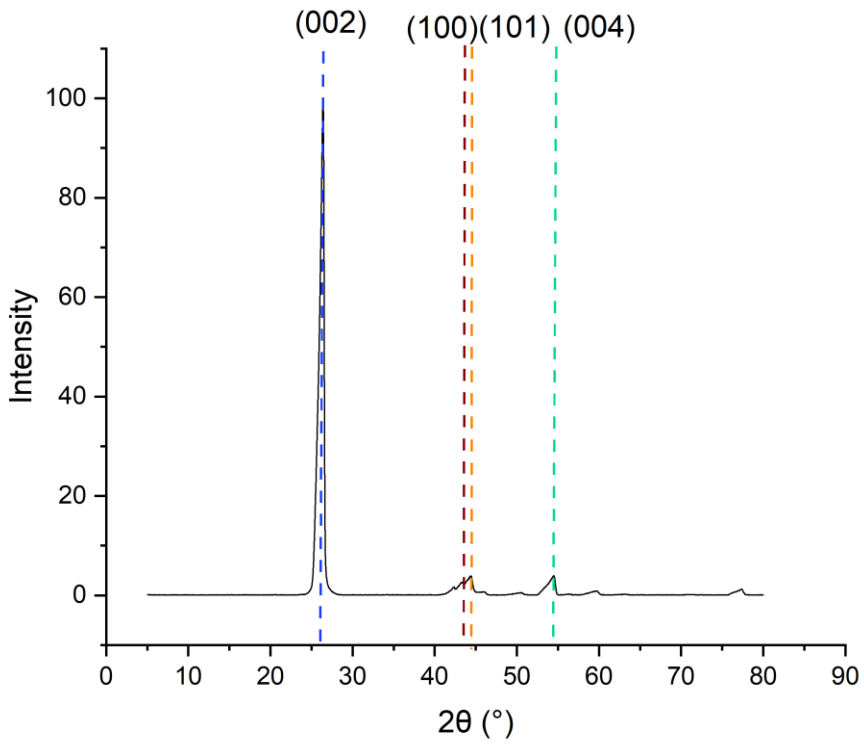

Figure 2.2: XRD of commercial synthetic graphite (Sigma Aldrich).

Oya and Marsh introduced a peak classification terminology related to synthetic graphite. Based on this, the (002) peak can be further described by the G-effect, T-effect, and A-effect. The G-effect refers to the complete graphitization process, which results in the formation of ordered graphite. It presents a sharp (002) peak in XRD at approximately 26.5°, corresponding to an interlayer spacing nearly equal to the ideal graphite's theoretical value of 0.3350 nm. A (002)-peak observed near the 26° angle indicates the structural characteristics of turbostratic graphite produced by the T-effect. The d-spacing value of turbostratic carbon exceeds 0.3400 nm. A broad (002) peak around 25.5° is caused by the A-effect and signifies a failure to form graphite.[27]

The crystallite height (L_c) and the crystallite width (L_a) are important parameters to calculate in graphitized carbons. Therefore, XRD spectra were fitted using Voigt profiles, which combine Lorentzian and Gaussian peak functions. The full width at half maximum (FWHM) and peak

positions of the fitted (002) and (100) peaks were used in the Scherrer equation; Equations 2.3 and 2.4 are used to determine the L_c and L_a, respectively.

Equation 2.3: Determination of the crystallite height (L_c)

$$L_C = \frac{K\lambda}{B_{(002)} COS\, \theta_{(002)}}$$

Equation 2.4: Determination of the crystallite width (L_a)

$$L_a = \frac{K\lambda}{B_{(100)} COS\, \theta_{(100)}}$$

Where K is a predetermined scale factor, which is 0.90 for L_C and 1.84 for L_a, B is the FWHM of the (002) or (100) fitted peaks, and θ is the incident angle associated with the (002) or (100) fitted peaks.

In this research, XRD patterns were collected using a Bruker D2 Phaser, which features a copper target, and data were gathered using Cu K_α signals with a wavelength of 1.5406 Å operating at 30 kV and 10 mA. Origin 2024b software was used for the non-linear fitting of the XRD spectra.[113–116,118]

2.2. Raman spectroscopy

Raman spectroscopy is a non-destructive characterization technique that is highly useful for analyzing carbon materials, including various types of graphite. A monochromatic laser beam irradiates the sample, and the inelastic scattered light emitted from the sample shifts depending on the molecules it interacts with before reaching the detector.[120] The probability of an excited molecule jumping to a different lower state other than the origin is $1/10^7$. At room temperature, most molecules are in their ground vibrational state. When interacting with incident photons, the scattered photons usually lose energy, resulting in what is known as Stokes scattering. Anti-Stokes scattering occurs when these molecules interact with incident photons, and the scattering process returns them to the ground state, transferring energy to the molecules. Stokes scattering is a dominant phenomenon observed in Raman spectroscopy, as illustrated in Figure 2.3. While the anti-Stokes spectrum is naturally weaker than the Stokes spectrum because of fewer vibrationally excited molecules, this duality makes Raman spectroscopy a versatile and highly informative method for material analysis.[121–123]

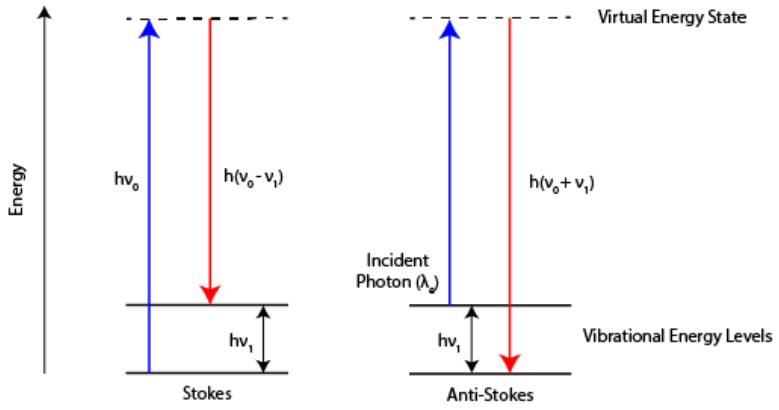

Figure 2.3: Schematic diagram of Stoke and Anti-Stoke scattering.

The energy difference between the excited molecule and the energy released from the initial state corresponds to the vibrational transition detected by the Raman spectrometer. Raman spectroscopy is represented by the Y axis (Intensity) and the X axis (Raman shift).[120]

The Raman spectrum analysis of graphite primarily focuses on the D, G, and 2D characteristic phonon peaks. The 2D peak indicates the presence of graphene layers in samples, enabling differentiation between monolayer, bilayer, and multilayer graphene. It appears near 2700 cm^{-1} and is a second-order Raman process involving two photons with opposite momentum originating from the K point. The sharper G peak (~1582 cm^{-1}) corresponds to in-plane stretching vibrations, reflecting the graphitic nature of the carbon samples. The G peak originates from the high symmetry Γ point and involves the E_{2g} vibration mode. The D peak (~1350 cm^{-1}) relates to the degree of disorder or the presence of defects in the samples. It originates between the K and K' points in the Brillouin zone and is linked to the A_{1g} vibration mode. Further insights into the disorder can be gained by examining the intensity ratio of the D and G peaks (I_D/I_G).[124,125] Researchers have previously observed that the I_D/I_G ratio decreases with increasing degree of graphitization. The D peak is absent in pristine graphite.[120–123,125,126]

In our investigation, Raman spectra of all samples were obtained using a Renishaw inVia Raman microscope. The spectrometer is equipped with a 633 nm laser and an 1800 lines/mm diffraction grating. The carbon samples were placed on a clean glass slide and scanned five times at the maximum laser power of 100 mW. Data acquisition was performed with Renishaw WiRE 3.4 software, and data analysis was conducted in OriginPro 2024b software.

2.3. Scanning electron microscopy (SEM)

SEM is an imaging technique that offers more profound insights into a sample's surface morphology, achieving magnifications ranging from 5× to 300 000×.[127] The wavelength of the probe determines the resolution power of these microscopes.[128,129] In optical microscopes, visible light is the probe, whereas electrons serve as the probe in electron microscopes. Therefore, the De Broglie wavelength is relevant in electron microscopes where a suitable electric potential can accelerate electrons. The electron wavelength is inversely proportional to the square root of the applied voltage. The maximum potential used in SEM is 30 kV, which produces electron wavelengths of nearly 7 pm. In SEM, backscattered (BSE) and secondary electrons (SE) are used to obtain topographical information, while chemical identification is primarily achieved through characteristic X-rays. The backscattered electrons are also known as reemergent beam electrons. The primary source of secondary electrons is inelastic scattering interactions, and SEs are generated by releasing valence electrons due to the energy of the incident beam. The ejection of SEs typically occurs within a few nanometers of the sample surface, making them highly sensitive to surface features. Backscattered electrons (BSE) originate from elastic scattering interactions and strongly depend on the atomic number of the elements in the specimen. While heavier elements scatter electrons more efficiently, the resultant images are brighter, providing atomic contrast.[128]

The optics and the sample of the SEM are kept in a vacuum. The vacuum prevents electron scattering and contamination of the electron guns and other related components. The electron gun, lens system (including condenser lens, apertures, and objective lens), specimen stage, and scanning unit (scanning coils, signal detection, processing system) are the main components of an SEM.[127–130]

In this work, SEM images were captured using the FlexSEM 1000 II scanning electron microscope. SEM samples were prepared by placing the powdered carbon products on a sticky

carbon tape, which was then exposed to a pressurized airflow to remove excess and improperly attached particles.

2.4. Transmission electron microscopy (TEM)

Transmission electron microscopy (TEM) provides more insights into the morphology, structure, chemistry, and bond types of a specimen. TEM uses higher electric potentials (around 400 kV), resulting in images with greater resolution generated by forward-scattered electrons. The magnification can reach up to 50 million times, allowing visualization at the atomic scale, which is significantly greater than that of an SEM.[131]

The components of TEM are arranged in a column, including an electron source, an illumination system, an image-forming system, and an image acquisition system. Thermionic electron sources and cold field emission guns are the two main types of electron sources in TEM. Electrons are accelerated by lenses and directed to the specimen through condenser lenses. The image-forming system comprises objective lenses, intermediate lenses, projector lenses, objective apertures, and selected area apertures. The image acquisition system mainly uses slow-scan CCD cameras and imaging plates. In TEM, both bright-field and dark-field images can be created. A direct beam forms bright-field images, while scattered beams are used to produce dark-field images. TEM also creates various diffraction patterns. Polycrystalline samples display ring patterns, single-crystalline materials show spot patterns, and Kikuchi lines can be observed due to inelastic electron scattering at small angles with slight energy loss.[132] They are further dispersed to form Kikuchi lines. The thickness of TEM samples should be less than 50 nm for electron transparency. Powdered inorganic samples are suspended in volatile solvents and drop-cast onto the sample holder. An ultramicrotome sections large samples into thin slices.[133]

In this thesis, TEM images were captured using a Bruker electron microscope. Samples for TEM were prepared by grinding to reduce particle size below 100 microns. The prepared thin samples were carefully mounted on TEM grids for observation.

2.5. Four-point probe technique

The ability of a material to conduct current is measured by its electrical conductivity (σ). The movement of electrons at the atomic level influences how electrical conductivity works. The four-point probe technique is widely used to measure the sheet resistivity (ρ/cm^2) of conductive

samples, which overcomes some practical issues associated with the two-point probe method, such as contact resistance, probe resistance, and spreading resistance. Notably, sheet resistivity measures the lateral resistivity of a thin film or coating. As shown in Figure 2.4, four tungsten carbide needles are arranged in an array with equal spacing *d* (m), ensuring that all needles contact the surface of the specimen similarly during measurement. While external needles are connected to a constant electrical current (*I*), the voltage (*V*) between the inner needles is measured using a voltmeter.[134,135]

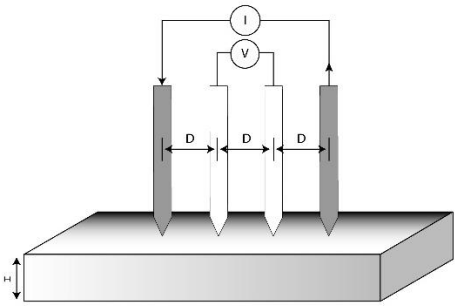

Figure 2.4: Schematic diagram of a four-point probe

Two equations are used to calculate the sheet resistivity based on the relative difference between the thickness of the thin layer (*t*) and the distance between the probe needles (d). If *t*>>*d*, the sheet resistivity is calculated using Equation 2.5 while Equation 2.6 is applicable when *t*<*d*.[134]

Equation 2.5*:* The sheet resistivity, if *t*>>*d*

$$\rho = 2\Pi d(\frac{V}{I})$$

Equation 2.6*:* The sheet resistivity, if *t*<*d*

$$\rho = \frac{\Pi t}{ln\,2}(\frac{V}{I})$$

Where, ρ is the sheet resistivity, *V* is the voltage measured from the inner two needles, *I* is the current passed through the outer two needles, and t is the thickness of the thin film.

The sheet conductivity (σ) and sheet resistivity (ρ) are inversely related, with σ being calculated as the inverse of ρ.

In this work, the electrical conductivities of carbon samples were measured using a Jandel four-point probe. The sample pellets, weighing nearly 0.5 g, were prepared with a hydraulic press to ensure measurement consistency. Sodium carboxymethyl cellulose (CMC) binder 5 wt.% was

mixed with the carbon sample, and the resulting mixture was pelletized under a 2 MT load for 3 minutes.

2.6. Brunauer-Emmett-Teller (BET) technique

The Brunauer-Emmett-Teller (BET) technique is based on nitrogen adsorption isotherms measured at 77 K and is generally used to calculate the specific surface area of samples. Nitrogen is commonly chosen because of its high purity, inert nature, and well-understood adsorption behavior, making it suitable for precise surface area measurements. Additionally, CO_2 adsorption is employed when the pore diameter of the microporous surface area is less than 1 nm.[136] The adsorbate (n^a), measured in mmol g^{-1} or cm^3 g^{-1} is plotted against the change in relative pressure ($p/p°$).

The specific relative pressure has a significant impact on the adsorption process. The t-plot shows the amount of gas adsorbed (V_{ads}) on the sample surface versus the calculated thickness (t) of the adsorbed layer, which is determined by referencing a non-porous standard material at the same relative pressure level. The micropore volume is calculated using a thickness range of 0.354 nm to 0.5 nm, with the y-intercept corresponding to the micropore volume. The Rouquerol BET technique confirms the accuracy of the BET surface area measurements.[137]

The isotherm is further classified into six shapes by IUPAC, as shown in Figure 2.5. The formation of a monolayer is indicated by the type I isotherm, also known as the Langmuir isotherm, which rises rapidly and smoothly to a maximum adsorption value. Type 1 isotherms are typical of microporous materials such as activated carbon. Type 2 isotherms characterize the adsorption behavior of wide or mesoporous surfaces. They include an initial inflection where relative pressure ($p/p°$) is greater than 0.1, followed by a second inflection where it rises quickly, and relative pressure exceeds 0.9. Regions with low adsorption potentials are characterized by the convex shape of the type 3 isotherm. Type 4a shows hysteresis, indicating capillary condensation or multilayer adsorption of the adsorbent from the vapor phase into the pores, forming a condensed liquid due to van der Waals interactions. Desorption occurs through capillary evaporation, meaning some trapped adsorbate remains in deeper pores, which causes delayed desorption. The type 4b isotherm exhibits a nearly absent hysteresis loop, as desorption closely follows the adsorption path. Mesoporous homogeneous surfaces are indicative of type 5 isotherms, where a hysteresis loop

during desorption is caused by gas molecules condensing in the pores. The type 6 isotherm represents non-porous homogeneous surfaces with multilayer adsorption.[138]

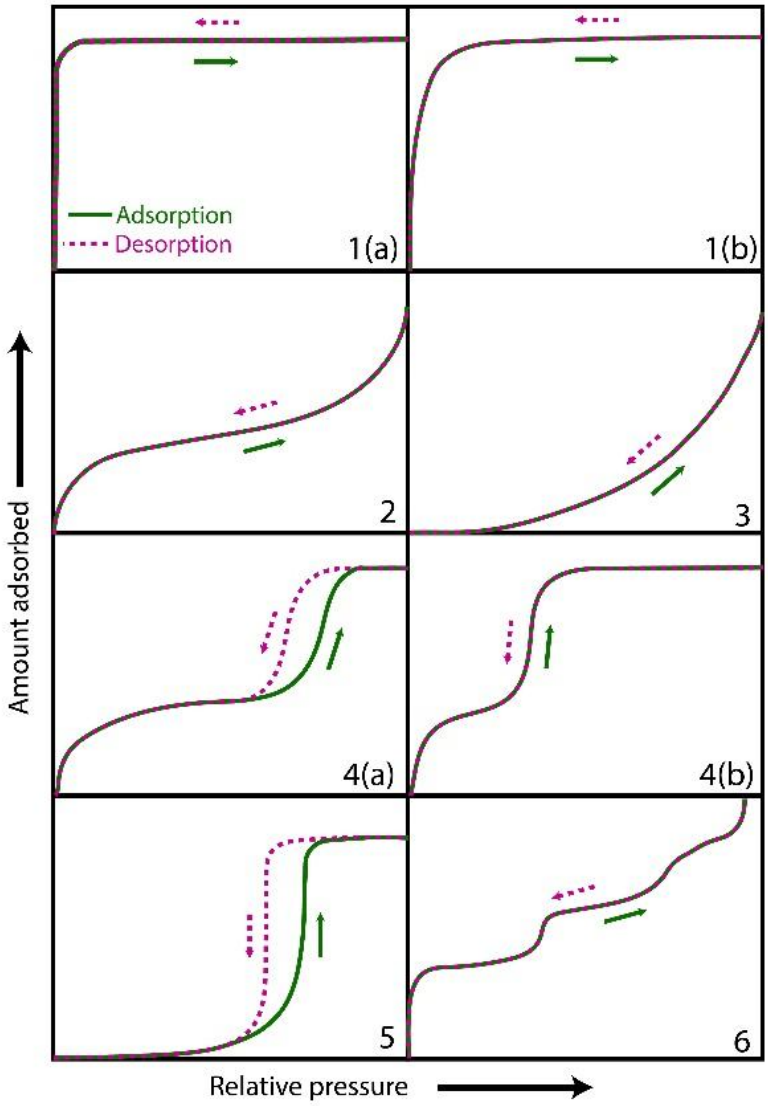

Figure 2.5: IUPAC isotherm shapes.

In this thesis, the Brunauer-Emmett-Teller (BET) equation (Equation 2.7) was primarily used to determine the specific surface area of graphitized carbons.

Equation 2.7: Brunauer-Emmett-Teller (BET) equation

$$\frac{p}{V(p^\circ - p)} = \frac{1}{V_m c} + \frac{(c-1)p}{V_m c\, p^\circ}$$

Where V is the volume of adsorbate ($cm^3\ g^{-1}$), V_m is the volume of gas for monolayer formation, p is the equilibrium pressure, $p°$ is saturated pressure, and c is the BET constant.[139]

The mass of the sample holding tube is determined before adding the sample to analyze the surface area of adsorbates. To remove any molecules from the air that might already be adsorbed to the surface, the sample is degassed with nitrogen at 300 °C. The mass is then measured again. Nitrogen gas is gradually pumped into the tube after it has been cooled in liquid nitrogen. As nitrogen adsorbs to the surface through van der Waals forces, it condenses, causing a pressure change. The volume of nitrogen adsorbed enables the calculation of the monolayer surface area, pore volume, and pore size distribution. The specific surface area was measured using a Micromeritics Tristar II Plus with Tristar II Plus v3.02 software. The samples were analyzed using N_2 adsorption at 77 K.

2.7. X-ray photoelectron spectroscopy (XPS)

X-ray photoelectron spectroscopy is a technique that measures the atomic percent composition and oxidation states of elements, with a lateral resolution of 10 µm to 50 µm.

The configuration of XPS mainly includes an X-ray photon source, a sample holder, an electron energy analyzer, an X-ray energy monochromator, a movable sample holder, focusing lenses for the emitted electron beam, and a high vacuum pump system, as shown in Figure 2.6. An Al or Mg cathode is used to generate a monochromatic X-ray beam. The X-ray beam is reflected onto the sample.

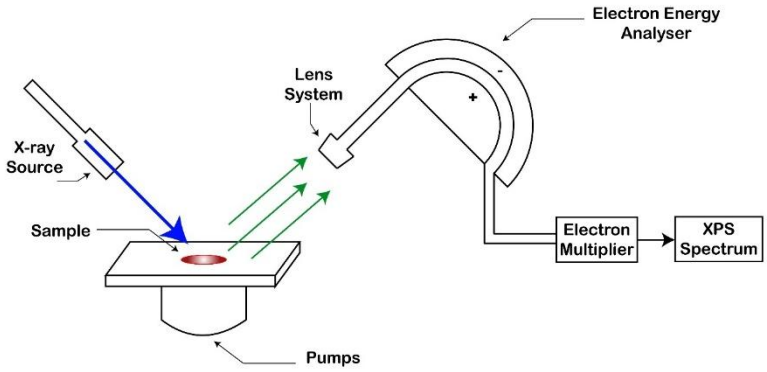

Figure 2.6: Schematic diagram of XPS.

XPS is operated under a high vacuum system (10^{-7}Pa) to ensure that all X-rays reach the surface of the sample without interference from any gases during characterization, and to increase the mean free path of electrons to facilitate their arrival at the detector.

Total energy conservation can be used to study the photoelectric effect. Here, the energy of the photon ($h\upsilon$) equals the sum of the electron's binding energy to the atom (E_b), the kinetic energy of the emitted electron (E_{res}), and the amount of thermodynamic work needed to remove an electron from the surface of a material ($\emptyset$). Equation 2.8 is resolved for E_b.

Equation 2.8: Binding energy calculation

$$E_b = h\upsilon - E_{res} - \emptyset$$

XPS sends X-rays with known energy $h\upsilon$, and the kinetic energy of the emitted electrons (E_{res}) is measured, which allows the calculation of the binding energy (E_b).

Auger electron spectroscopy detects secondary electrons and complements the information from XPS. Auger electron emission occurs when an electron is emitted due to the photoelectric effect, leaving a vacancy. Another electron then fills this vacancy in a higher energy level of the atom, releasing energy as it drops to a lower energy level. This energy can eject an electron (from the same shell) from the atom. The energy of this emitted electron does not depend on the photon's energy but on the energies of the shells involved in the Auger process. Auger-specific spectrometers typically use electron beams instead of photons.

In this thesis, XPS analyses were performed using a Thermo Fisher Scientific K-alpha spectrometer with a monochromatic Al K-alpha source (15 mA, 15 kV). The x-ray spot size was 400 μm, and fitting was conducted with CASA XPS (version 2.31).

3. Magnesium-assisted graphitization of petroleum coke using heat treatments: Efficacy of monometallic mediators in graphitization.

3.1. Introduction

As discussed in Chapter 1, the goal is to find metal mediators that perform as well as iron in metal-assisted graphitization while improving the removal of metals after the process. A thorough review of the literature has identified magnesium as a promising candidate.[3] To evaluate the influence of sulfur contamination in petroleum coke, purified petroleum coke was also used as a carbon precursor. It is noteworthy that the purification of petroleum coke is achieved through an activation process using potassium hydroxide (KOH), resulting in the formation of activated carbon.[1] Consequently, the purified form of petroleum coke is referred to as activated carbon in this thesis.

This chapter describes the methodologies, sample preparation procedures, characterization techniques, and results related to the magnesium-incorporated graphitization. From now on, graphite samples produced from activated carbon-magnesium mixtures are referred to as magnesium-assisted graphitized activated carbon (MgACs) and those prepared from petroleum coke are referred to as magnesium-assisted graphitized petroleum coke (MgPCs), respectively.

3.1.1. Monometallic mediator: Magnesium

Magnesium is a commonly used alkaline earth metal in chemistry, with a low melting point of 650 °C.[11] The lower melting point of magnesium could lead to lower graphitization temperatures. Few studies have used magnesium in carbon graphitization compared to group VIII transition metals. In 1978, Asao Oya and Sugio Otani observed the formation of graphitic structures after graphitizing phenol-formaldehyde resin with magnesium powder at 3000 °C.[139] However, this temperature is sufficient to graphitize the carbon precursor without a metal-assisted mechanism. [140] Zhao, L. et al demonstrated the potential of removing magnesium after graphitization of various precursors. In post-graphitization, 2 g of the mixture (1:1 carbon: magnesium) was treated with 100 ml of 2M HCl and stirred for 12 hours at room temperature. The absence of magnesium or magnesium oxide-associated peaks in XRD analysis and 0.009-0.019 wt.% of residual magnesium in ICP-OES measurements confirmed the successful removal of magnesium after the acid treatment. They attempted to graphitize pyrolyzed glucose using ball-milled carbon-magnesium

alloys and magnesium vapor. Magnesium vapor proved to be an ineffective method for graphitization, resulting in amorphous carbon. Interestingly, XRD analysis revealed the formation of crystalline carbon at 1000 °C after 3 hours, as indicated by a sharp peak at 26.25° and a shoulder peak at 26.7°, corresponding to turbostratic and graphite phases, respectively.[3] Fu Yang et al. introduced magnesium as a metal reactant to graphitize anthracite coal. In their study, magnesium was incorporated at the same ratio as anthracite coal, and the composite was heated at various temperatures for 2 hours with a heating rate of 5 °C /min in argon. XRD analysis showed a sharp (002) peak at a 2θ of 25.83 ° at 1100 °C, indicating the coexistence of both ordered and amorphous carbon. Moreover, the I_D/I_G ratio was 0.48 in the Raman analysis, indicating the depletion in the degree of disorder.[5] Magnesium alters the surface morphology of carbon during the graphitization process while enhancing the degree of graphitization.[93] However, the current literature does not clearly explain the mechanism by which graphitic carbon is produced by magnesium addition. Additionally, a detailed analysis of magnesium removal for optimizing the process has not yet been performed. Notably, the use of magnesium as the metal reactant for graphitizing petroleum coke has not been explored in the available literature.

3.1.2. Effect of carbon precursor particle size on graphitization

The impact of the particle size of the carbon precursor in metal-assisted graphitization has received little attention in the literature. The mechanism of metal-assisted graphitization involves either the formation of metal carbide bonds or the dissolution of carbon into the molten metal, followed by the precipitation of graphite.[3,31,140] In the former mechanism, the size distribution of precursor petroleum coke (petcoke) particles can significantly influence the effectiveness of metal carbide formation due to differences in surface area, which affect the interaction dynamics between carbon and the metal mediator. In the carbon dissolution precipitation mechanism, this study hypothesized that smaller carbon particles can speed up the diffusion of carbon atoms, thereby promoting the precipitation of graphitic carbon. Additionally, the particle size of the carbon precursor may influence the mechanism by changing the energy requirements and providing diverse nucleation sites. Generally, smaller carbon particles have a higher specific surface area[142] and thereby provide more nucleation sites, enabling a more uniform and effective graphitization process. Considering this, we examined the effect of activated carbon particle size on the degree of graphitization in systems containing magnesium.

3.1.3. Seeding technique for enhancing the degree of graphitization

The seeding technique involves adding graphite or crystalline carbon to the precursor carbon material during graphitization. Essentially, the formation of graphite begins with the deposition of carbon atoms, layer by layer, to reach the lowest energy state. These “seeds” can serve as nucleation points, helping to align and order carbon atoms during the graphitization process. It is believed that the seeding method can significantly affect the efficiency and quality of synthetic graphite production.

Several methods can be used to enhance the graphitization process through seeding. The presence of seeds lowers the energy barrier for converting amorphous carbon into a graphitic structure, thereby improving process efficiency. Additionally, seeding can help produce a more uniform and higher degree of crystallinity in the final graphite product. This approach can also potentially reduce the time and energy needed to achieve the desired graphitic structure, making it a valuable technique in synthetic graphite production.

3.2. Experimental

3.2.1. Synthesis of graphitized carbon incorporating magnesium

Activated carbon/petroleum coke was ground for 15 minutes with magnesium powder (20-230 mesh, Sigma-Aldrich) in a 1:1 carbon to magnesium mass ratio using a mortar and pestle. The schematic diagram of the graphitization process is displayed in Figure 3.1. These resulting mixtures were placed in closed stainless-steel crucibles and heated in nitrogen at 1000 °C, 1100 °C, 1200 °C, 1400 °C, and 1600 °C. Graphitization was further optimized by varying dwell times from 30 minutes up to 24 hours at the selected temperature. The heating and cooling rates were set to 40 °C per minute. For the post-graphitization treatment, approximately 2 g of MgACs or MgPCs with magnesium was reacted with 2 M HCl (prepared from 37 wt.% HCl, Sigma Aldrich) and stirred for 1 hour at 70 °C. Afterwards, the products were filtered and washed repeatedly with deionized water until the pH of the supernatant reached about 6.5-7. Finally, the products were air-dried overnight at 120 °C.

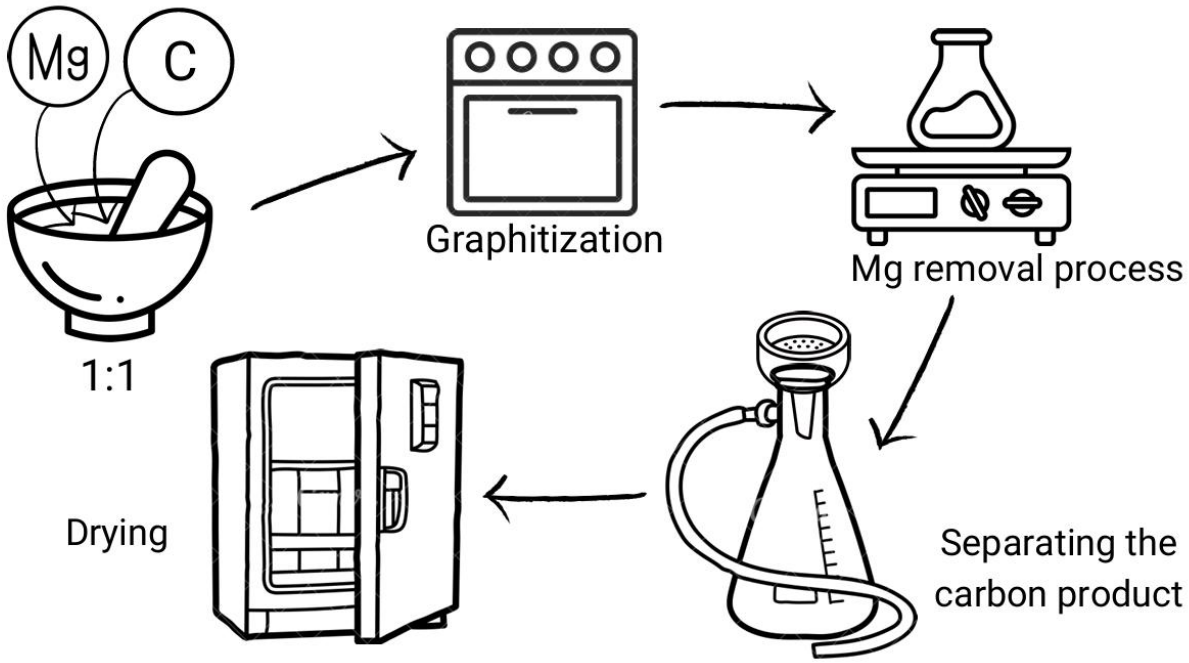

Figure 3.1: Schematic diagram of the graphitization process of petroleum coke / activated carbon with magnesium.

3.2.2. Pelletization and Electrical Conductivity Measurements

In this study, the electrical conductivities of carbon samples were measured after they were pelletized (Figure 3.2). Three pellets were produced from a single composition to measure electrical conductivity. Notably, pellets made from highly disordered carbon materials like activated carbon often break apart during conductivity tests. This may occur because of the high absorption capacity of amorphous carbon, which creates a practical challenge during measurement. Despite this issue, the binder composition remains the same to maintain consistency in the comparison.

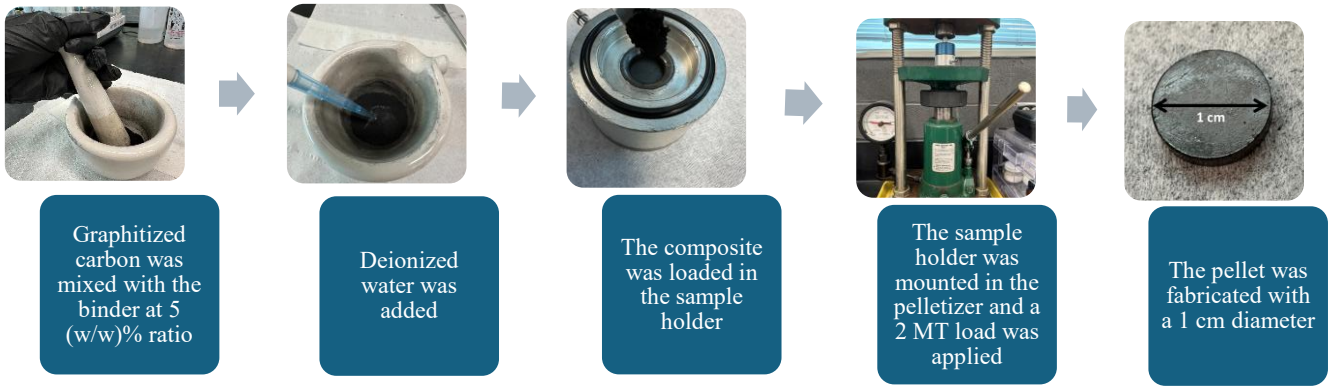

Figure 3.2: The pelletization process.

Electrical conductivity of the pellets was measured using a four-point probe (Jandel, RM3000+) with a supply current of 10 mA.

3.2.3. Seeding technique

The seeding technique was introduced into the graphitization process for the first time to control the nucleation and growth of crystalline structures through synthetic graphitization. Adding carbon atoms to the edge of an existing graphene sheet is more energetically favourable than starting a new sheet.[31] Based on that, the seeding technique was used in the graphitization process. First, activated carbon was mixed with synthetic graphite (Sigma Aldrich) at ratios of 1 wt.%, 3 wt.%, and 5 wt.%. Next, magnesium powder (Sigma Aldrich) was added at a 1:1 carbon to magnesium ratio and ground for 15 minutes using a mortar and pestle. The resulting mixtures were then placed in closed stainless-steel crucibles and heated in nitrogen at 1000 °C for 24 hours. Finally, the graphitization and magnesium removal processes were carried out as described in Section 3.2.1.

3.2.4. Microwave-assisted Graphitization

Samples containing magnesium and activated carbon were prepared following the same protocol described earlier. Activated carbon was thoroughly ground with magnesium powder using a mortar and pestle to ensure uniformity. Two compositions were tested: a 2:1 mass ratio of activated carbon to magnesium, and a 1:1 mass ratio.

Microwave graphitization was performed using a high-temperature microwave furnace equipped with a silicon carbide (SiC) susceptor, which acts as the central heating element. The entire heating process was microwave-driven, with the SiC susceptor absorbing microwave energy and

producing uniform heat within the furnace cavity. The temperature ramp rate was set to 20 °C per minute, and the system was programmed to monitor the bulk cavity temperature in real time using a NIST-traceable dual thermocouple inserted through the top of the unit. This thermocouple provided precise feedback on the overall cavity temperature, although localized heating effects caused by direct microwave interaction with the sample matrix may have occurred.

Aluminum oxide crucibles were used to contain the samples. Before use, these crucibles were thoroughly cleaned with deionized water and pre-ashed at 1050 °C to remove any residual contaminants. Each crucible was partially covered with CEM quartz fiber lids, which are permeable to gas flow. This setup minimized material loss during heating while allowing continuous nitrogen flow into the crucible. An inert atmosphere was maintained throughout the process using nitrogen gas, supplied at a constant pressure of 40 psi via a regulated inlet. The nitrogen flow remained uninterrupted during both the heating and cooling phases. The furnace cavity was not opened until the bulk temperature dropped below 200 °C, ensuring safe handling and preventing oxidation of the samples.

This method maintained controlled thermal conditions and minimized contamination or oxidation, allowing for consistent assessment of the structural evolution of carbon materials during microwave-induced graphitization.

3.2.5. Characterization

The synthesized products were characterized using several techniques: Raman spectroscopy, X-ray diffraction (XRD), Brunauer-Emmett-Teller (BET) surface analysis, X-ray photoelectron spectroscopy (XPS), scanning electron microscopy (SEM), transmission electron microscopy (TEM), and four-point probe. These techniques are comprehensively discussed in detail in Chapter 2.

3.2. Results and Discussion

3.2.3. Structural characterization

3.2.3.1. Effect of temperature on the graphitization process

Figure 3.3 illustrates the XRD pattern of petroleum coke and activated carbon before graphitization. Activated carbon displays a characteristic XRD spectrum of non-graphitizable carbon (hard carbon). It features two broad peaks near 25° and 45°, which are typical of disordered hard carbon.[3] The XRD spectrum of petroleum coke shows a broad peak around 25°, indicating the presence of amorphous carbon, along with smaller, sharper peaks of contaminants. A closer view of the (002) peak (Figure 3.3) appears in the spectrum of petroleum coke at approximately 26.4°, which is likely a characteristic feature of soft carbon (graphitizable carbon) containing small graphitic structures.[24] The Raman spectra depicted in Figure 3.4 reveal two overlapping broad peaks characteristic of amorphous carbon.[143]

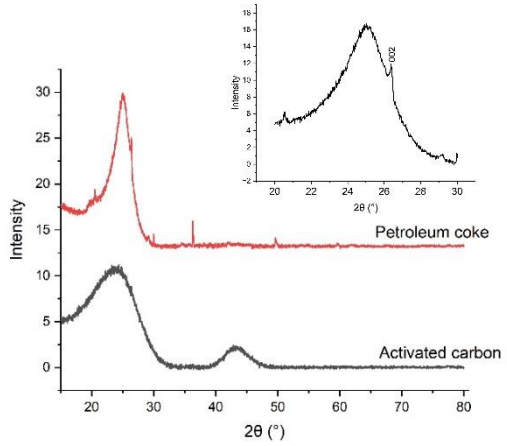

Figure 3.3: XRD spectra of petroleum coke and activated carbon.

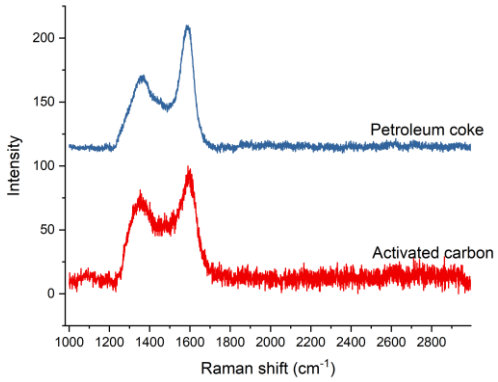

Figure 3.4: Raman spectroscopy of petroleum coke and activated carbon.

Figure 3.5 presents the Raman spectra of graphitized activated carbons (MgACs) at various temperatures over 3 hours. The temperature profiles range from 1000 °C to 1600 °C. The appearance of the 2D peak around 2700 cm^{-1} clearly highlights the formation of graphene structures within the material. The conversion of amorphous carbon to crystalline carbon was observed at 1000 °C, as indicated by the increased sharpness of peaks compared to raw materials (Figure 3.5). Furthermore, the separation of the D band (~1350 cm^{-1}) and G band (~1582 cm^{-1}) is

visible at this temperature, indicating the development of ordered carbon. Despite increasing the heating temperature, the Raman spectra show no significant changes in the I_D/I_G ratio or peak sharpness. Notably, a strong 2D band appears at all temperatures. This discrepancy from the initial expectation is due to the boiling point of magnesium, which is 1091 °C. Above this temperature, magnesium vaporizes and no longer contributes to the graphitization process.

Conversely, as shown in Figure 3.6 and Table 3.1, graphitization of petroleum coke shows a decrease in the I_D/I_G ratio at 1400 °C and 1600 °C. Despite magnesium boiling off at these temperatures, several factors may explain the decrease in the I_D/I_G ratio, accompanied by sharper D and G bands. First, reaching high temperatures at a rate of 4 °C per minute takes considerable time, which doubles during cooling at the same rate. As a result, the metal-carbon composites have more time to arrange their structure before the magnesium evaporates. This may contribute to the slight reduction in the I_D/I_G ratio seen in graphitized activated carbon samples at 1400 °C and 1600 °C, as presented in Table 3.1. Secondly, petroleum coke, being a soft carbon (graphitizable carbon), requires less energy to form ordered structures compared to activated carbon, which shows characteristics of hard carbon (non-graphitizable) according to XRD analysis and has greater porosity.[24] This experiment is non-repeatable because magnesium vapor forms at temperatures above 1091 °C, causing magnesium to deposit on the furnace's ceramic tube and resulting in tube damage.

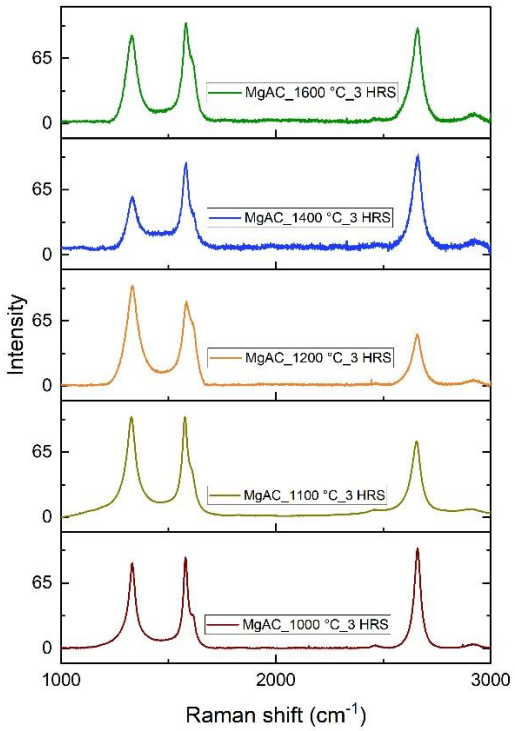

Figure 3.5: Raman spectroscopy analysis of graphitization of **activated carbon** with magnesium at various temperatures.

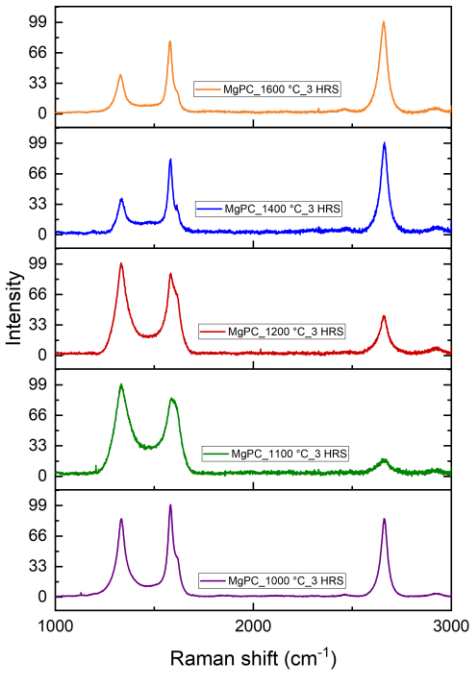

Figure 3.6: Raman spectroscopy analysis of graphitization of **petcoke** with magnesium at various temperatures.

Table 3.1: I_D/I_G ratios of Raman spectroscopy spectra of graphitized activated carbon (MgACs) and petroleum coke (MgPCs) at various temperature profiles

Sample	**I_D/I_G ratio**	**Sample**	**I_D/I_G ratio**
MgAC 1600 °C, 3 hrs	0.78 ± 0.10	MgPC 1600 °C, 3 hrs	0.50 ± 0.17
MgAC 1400 °C, 3 hrs	0.62 ± 0.07	MgPC 1400 °C, 3 hrs	0.47 ± 0.04
MgAC 1200 °C, 3 hrs	1.18 ± 0.07	MgPC 1200 °C, 3 hrs	1.12 ± 0.07
MgAC 1100 °C, 3 hrs	1.06 ± 0.36	MgPC 1100 °C, 3 hrs	1.18 ± 0.05
MgAC 1000 °C, 3 hrs	0.96 ± 0.37	MgPC 1000 °C, 3 hrs	1.24 ± 0.06

3.2.3.2. Effect of dwell time on the graphitization process

The graphitization temperature reached its optimal point at 1000 °C because magnesium's boiling point is 1091 °C; therefore, the working temperature remains below its boiling point. Different time periods, ranging from 30 minutes to 24 hours, were used to treat the metal-carbon composites and enhance graphitization. The Raman spectroscopy of MgAC 1000 °C, 30 minutes sample, shown in Figure 3.7, displays an intense and broader D peak indicating a disordered structure, which is also supported by the I_D/I_G ratio of 1.26 ± 0.14, as shown in Table 3.2. The 2D peak appears in the spectrum after a 30-minute graphitization period. The D peak starts to diminish after 3 hours of graphitization, resulting in an I_D/I_G ratio of 0.96 ± 0.37, although the standard deviation remains high. The D and G peak ratios decrease in MgAC 1000 °C, 6-hour sample, as shown in Figure 3.7, while the ratios continue to fluctuate at 12 hours. The I_D/I_G ratio remains consistent with the 6-hour measurement until it drops to 0.66 ± 0.11 after 24 hours of dwell time. The lowest I_D/I_G ratio observed in graphitized activated carbon occurs when magnesium-assisted graphitization is employed with extended dwell times at moderate temperatures.

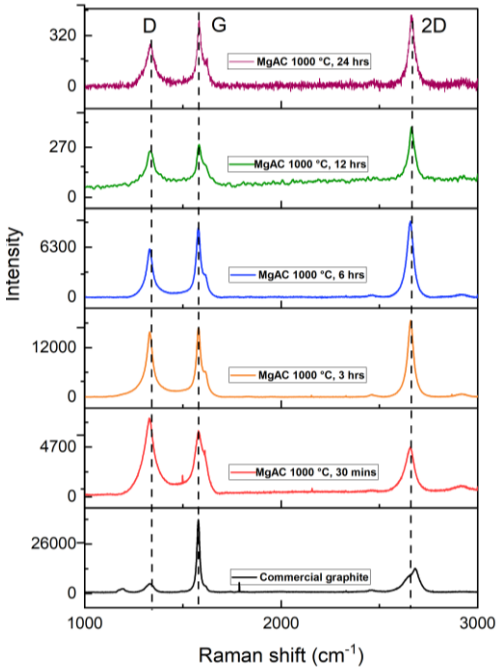

Figure 3.7: Raman spectroscopy analysis of graphitization of activated carbon with magnesium at various dwell times.

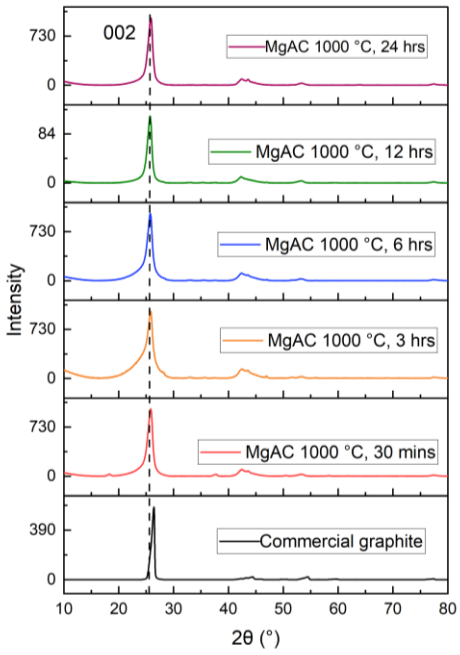

Figure 3.8: XRD analysis of graphitization of activated carbon with magnesium at various dwell times.

Table 3.2: Intensity ratios of D and G peaks of graphitized activated carbon at 1000 °C for various dwell times.

Sample	I_D/I_G ratio
MgAC 1000 °C, 24 hrs	0.66 ± 0.11
MgAC 1000 °C, 12 hrs	0.89 ± 0.07
MgAC 1000 °C, 6 hrs	0.70 ± 0.13
MgAC 1000 °C, 3 hrs	0.96 ± 0.37
MgAC 1000 °C, 30 mins	1.26 ± 0.14
Commercial graphite	0.14 ± 0.05

The XRD results for the same set of samples are presented in Figure 3.8. All samples exhibit a very sharp peak around 26°, which has been identified as the (002) peak. Table 3.3 outlines the average values for d-spacing ($d_{(002)}$), stacking height (L_c), and crystallite size (L_a) for each sample based on three measurements. The MgAC sample at 1000 °C, 30 minutes exhibited a significant stacking height L_c (7.64 ± 0.40) nm even after a short period. Table 3.3 indicates that a crystallite size of up to (20.0 ± 6.56) nm is achieved in only 3 hours at this low temperature. However, these calculated parameters were not consistent throughout subsequent experiments with extended hours. After 24 hours of graphitization (MgAC 1000 °C, 24 hours), both the crystallite size and stacking height stabilized at (20.7 ± 0.45) nm and (8.24 ± 0.14) nm, respectively. The low standard deviation is indicative of a more homogeneous sample or sample set.

Table 3.3: XRD analysis of graphitized activated carbon at 1000 °C for various dwell times.

Sample	**$d_{(002)}$ (nm)**	**L_c (nm) (Stacking height)**	**L_a (nm) (Crystallite size)**
MgAC 1000 °C, 24 hrs	0.3440 ± 0.0001	8.24 ± 0.14	20.7 ± 0.45
MgAC 1000 °C, 12 hrs	0.3445 ± 0.0006	8.40 ± 0.23	18.3 ± 1.95
MgAC 1000 °C, 6 hrs	0.3447 ± 0.0008	8.48 ± 0.28	17.7 ± 2.76
MgAC 1000 °C, 3 hrs	0.3435 ± 0.0007	9.87 ± 1.62	20.0 ± 6.56
MgAC 1000 °C, 30 mins	0.3445 ± 0.0008	7.64 ± 0.40	17.3 ± 2.10

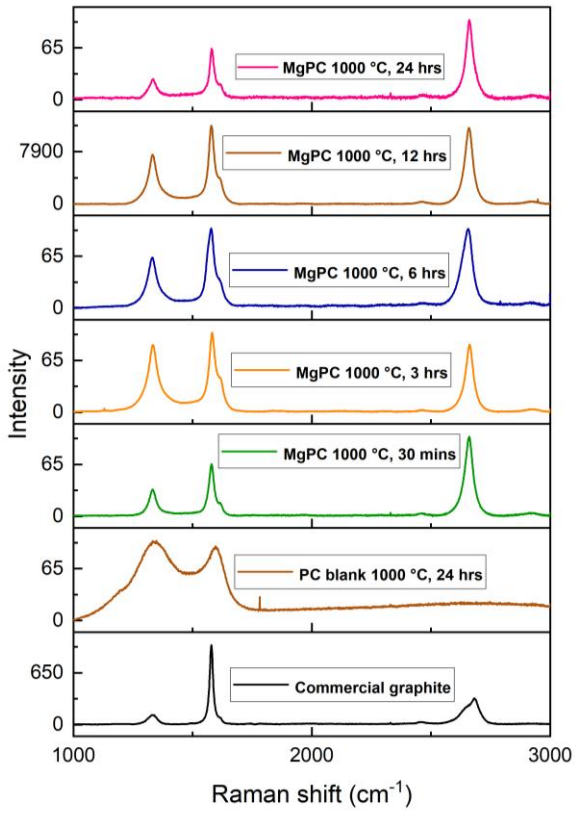

Figure 3.9: Raman spectroscopy analysis of graphitization of petcoke with magnesium at various dwell times.

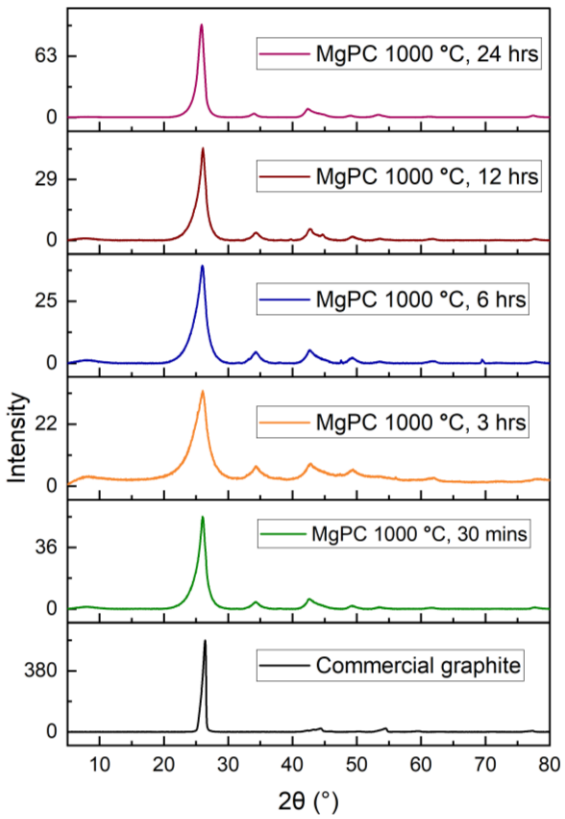

Figure 3.10: XRD analysis of graphitization of petcoke with magnesium at various dwell times.

Table 3.4 : Intensity ratios of D and G peaks of graphitized petroleum coke at 1000 °C for various dwell times.

Sample	**I_D/I_G ratio**
MgPC 1000 °C, 24 hrs	0.61± 0.15
MgPC 1000 °C, 12 hrs	0.67 ± 0.27
MgPC 1000 °C, 6 hrs	0.58 ± 0.22
MgPC 1000 °C, 3 hrs	0.86 ± 0.25
MgPC 1000 °C, 30 mins	0.51 ± 0.17

Table 3.5: XRD analysis of graphitized petroleum coke at 1000 °C for various dwell times.

Sample	**(002) peak position 2θ (°)**	**$d_{(002)}$ (nm)**	**L_c (nm) (Stacking height)**	**L_a (nm) (Crystallite size)**
MgPC 1000 °C, 24 hrs	25.8	0.3450 ± 0.0001	8.5 ± 0.7	17.1 ± 2.7
MgPC 1000 °C, 12 hrs	25.8	0.3456 ± 0.0005	7.2 ± 3.1	16.5 ± 3.5
MgPC 1000 °C, 6 hrs	25.7	0.3468 ± 0.0005	4.8 ± 1.7	13.5 ± 0.0
MgPC 1000 °C, 3 hrs	25.5	0.3485 ± 0.0004	4.1 ± 1.6	15.0 ± 1.2
MgPC 1000 °C, 30 mins	25.6	0.3477 ± 0.0002	6.3 ± 2.0	16.6 ± 3.6
Commercial graphite	26.4	0.3371	15.0	28.2

The effect of dwell time on the degree of graphitization of MgPC was investigated at 1000 °C using the same time profile as MgAC. Raman spectra of MgPC samples graphitized at 1000 °C for different dwell times are depicted in Figure 3.9. It is clear at first glance that an intense 2D peak appears and the D peak diminishes, indicating a decrease in disorder and the formation of thin layers after just 30 minutes at a moderate temperature. The I_D/I_G ratio varied slightly with a significant standard deviation, as shown in Table 3.4. The I_D/I_G ratio was recorded at 0.51 ± 0.17 after 30 minutes and at 0.61 ± 0.15 after 24 hours of graphitization. The narrow range of the I_D/I_G ratio, even at longer dwell times, could be due to the irregular structures in petroleum coke and contaminants like sulfur. On the other hand, MgPC samples exhibit a lower level of disorder compared to MgAC samples. The difference between MgAC and MgPC samples is probably due to the porosity level in graphitized samples, which will be discussed further in Section 3.3.2. The same set of samples was analyzed using XRD to examine the characteristics of their graphitic structure. The XRD spectra of MgPC samples graphitized at 1000 °C for various durations are shown in Figure 3.10. Each spectrum shows a sharper (002) peak, indicating an improvement in the degree of graphitization.

Further analyses are presented in Table 3.5, which provides analyzed values of the d-spacing ($d_{(002)}$), stacking height (L_c), and crystallite size (L_a) for each sample based on three replications. All graphs were fitted with Voigt profiles (combining Lorentzian and Gaussian peak functions) using Origin 2024b software. The L_c and L_a values recorded were (6.3 ± 2.0) nm and (16.6 ± 3.6) nm, respectively, after just 30 minutes of graphitization. The L_c value remained nearly consistent, considering the standard deviation, up to 6 hours. Notably, after 24 hours of graphitization, the L_c value further increased to (8.5 ± 0.7) nm. Here, the lower standard deviation highlights the uniformity of the structure at longer dwell times. Moreover, L_a ranged from (13.5 ± 0.0) nm to (17.1 ± 2.7) nm during the 30-minute to 24-hour dwell period. Overall, there is no significant improvement in either L_a or L_c after 24 hours of graphitization compared to 30 minutes. However, the reduction in standard deviation should be considered when optimizing the graphitization time.

3.2.3.3. Effect of particle size of carbon precursor on the graphitization

The influence of the precursor material's particle size on graphitization was investigated using activated carbon in three particle size distributions. Few studies have explored the impact of metal particle size on the synthetic graphitization process. Hunter et al. investigated the ability of metal nanoparticles to graphitize amorphous carbon at a temperature lower than the melting point (T_m). [31] It is established that molten metal particles exhibit liquid-like characteristics, allowing them to move around amorphous carbon at high temperatures and form crystalline structures. When the size of the molten metal particles exceeds 100 nm, the fused particles inhibit mobility.[144]

However, no study has shown the impact of the particle size of the carbon precursor. Figure 3.11 shows the Raman spectroscopy analysis of graphitized activated carbon samples made from sized activated carbon particles with diameters of < 116.8 µm, 228.6 µm - 381.0 µm, and > 381.0 µm. The magnesium particle size ranged from 53.3 µm to 116.8 µm. Growing graphene sheets encapsulate molten metal particles during the synthetic graphitization process.[31] This highlights the potential significance of particle size. According to the Raman analysis, activated carbons with small particle sizes (AC< 116.8 µm) exhibit a higher degree of disorder: broad peaks, an extremely low 2D peak, and a high I_D/I_G ratio of 1.17 ± 0.15. The size ratios of carbon particles and metal particles, both of which are less than 116.8 µm in this context, make the size ratios nearly equal. The medium-sized activated carbon exhibited the lowest degree of disorder (I_D/I_G ratio: 0.79 ±

0.20). Additionally, the presence of a strong 2D peak indicates the presence of graphene sheets. In comparison, larger activated carbon particles exhibit moderate graphitic features in Raman analysis. The XRD spectra of the samples shown in Figure 3.12 display a sharp (002) peak in the spectrum of the medium-sized activated carbon samples, which aligns with the results of the Raman analysis.

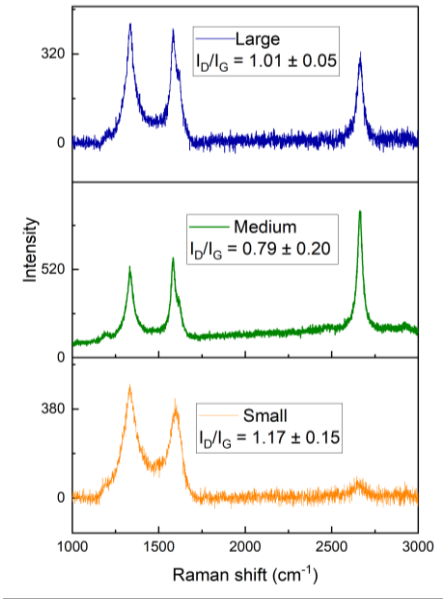

Figure 3.11: Raman spectra of graphitized activated carbons in three particle sizes, which were heated at 1000 °C over 24 hours.

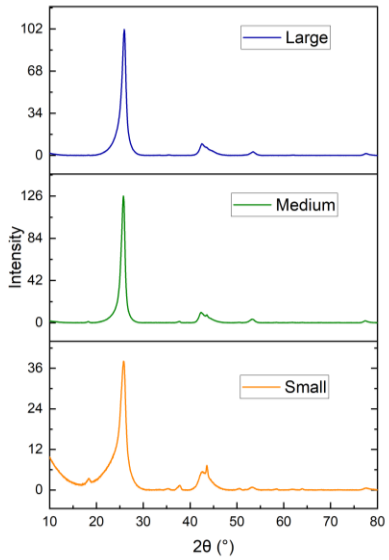

Figure 3.12: XRD analysis of graphitized activated carbons in three particle sizes, which were heated at 1000 °C over 24 hours.

Table 3.6: Crystal structure analysis of graphitized activated carbons in various particle sizes.

Sample	**(002) peak position 2θ (°)**	**$d_{(002)}$ (nm)**	**L_c (nm) (Stacking height)**	**L_a (nm) (Crystallite size)**
MgAC > 0.3810 mm 1000 °C, 24 hrs	26.0	0.3430 ± 0.0006	7.7 ± 0.1	15.6 ± 0.5
0.3810 mm < MgAC< 0.2286 mm_ 1000 °C, 24 hrs	25.8	0.3456 ± 0.0003	8.8 ± 0.0	19.1 ± 0.3
MgAC < 0.1168 mm 1000 °C, 24 hrs	25.8	0.3449 ± 0.0006	5.4 ± 0.1	12.2 ± 0.2

The XRD analysis of the small activated carbons revealed a minimal graphitic structure, as shown in Table 3.6. These small-sized activated carbons exhibited minimal graphitic ordering with magnesium, indicated by a low stacking height (5.4 ± 0.1) nm and small crystallite size (12.2 ± 0.2) nm. The lattice structure data align with Raman results, since medium-sized activated carbons produce the largest crystals, with a stacking height of (8.8 ± 0.0) nm and a crystallite size of (19.1 ± 0.3) nm. Although the crystal structure formation is slightly less developed in large-sized activated carbon particles compared to medium-sized ones, the d-spacing value decreases to (0.3430 ± 0.0006) nm.

Activated carbon particles larger than magnesium particles showed better graphitization outcomes compared to smaller particles. This phenomenon remains without sufficient explanation. Analysis combining TEM with XRD results would provide additional insight into this mechanism.

3.2.3.4. Effect of seeding technique on the graphitization

The section investigated how adding small amounts of graphite to activated carbon before the graphitization process influenced synthetic graphitization. The hypothesis suggests that crystalline carbon will encourage synthetic graphitization by creating additional nucleation sites. Synthetic graphitization forms its initial graphene layer by building successive layers during this process. This approach has the potential to accelerate the graphitization process by providing additional essential nucleation sites.

Raman spectroscopy data for graphitized carbon samples with 0 wt.%, 1 wt.%, 3 wt.%, and 5 wt.% graphite seeding ratios in 1:1 carbon-to-magnesium systems are presented in Figure 3.13. The thermal graphitization was conducted at 1000 °C for 24 hours under a nitrogen atmosphere. The Raman spectroscopy results showed D and G bands, with the D band always being less intense than the G band across all samples, indicating low levels of structural disorder. The peaks become more distinct, showing increased graphitic ordering as the seeding amount increases. Quantitative assessment using the I_D/I_G ratio further supports this trend, indicating improved graphitization as graphite seeding ratios increase, as reported in studies.[18,19,27] The Raman spectra revealed I_D/I_G ratios of 0.7 ± 0.1 for the unseeded sample, while the seeded samples showed ratios of 0.7 ± 0.2, 0.8 ± 0.2, and 0.6 ± 0.2 for 1 wt.%, 3 wt.% and 5 wt.% graphite seeding, respectively. Although these values show minor differences in structural disorder, the overlapping standard deviations

demonstrate that the differences are not statistically significant. The I_D/I_G ratio is inadequate as a reliable indicator for detecting changes in graphitic ordering caused by graphite seeding due to its limited sensitivity. This ratio cannot accurately assess the subtle structural modifications resulting from seeding.

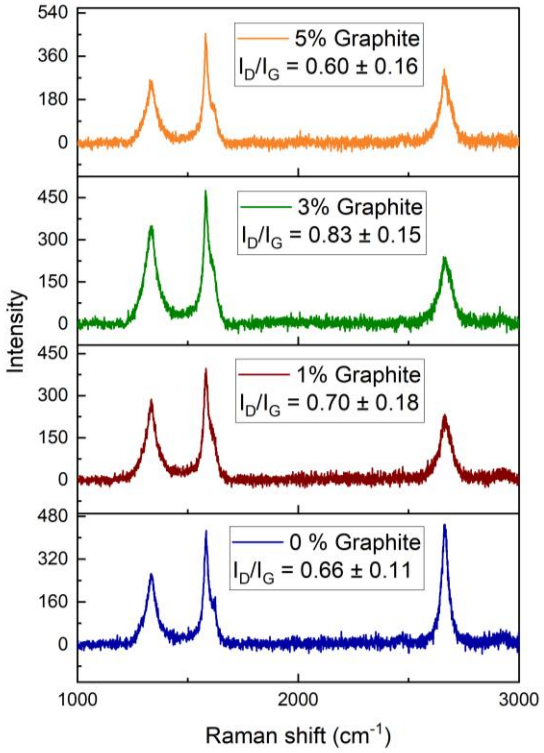

Figure 3.13: Raman spectra of activated carbon graphitized with magnesium at 1000 °C for 24 hours, showing the effect of varying graphite seeding ratios.

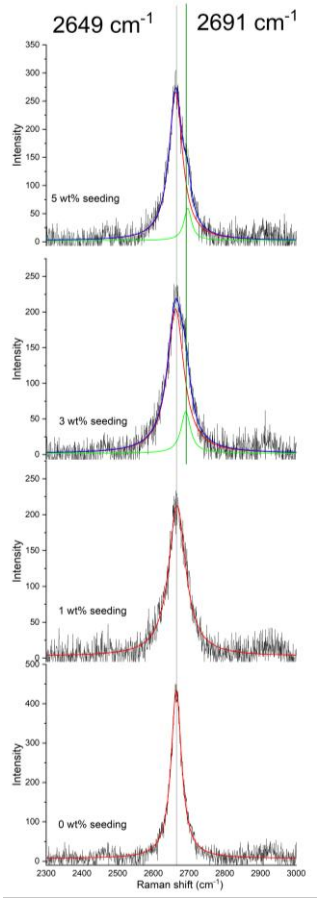

Figure 3.14: 2D bands of graphitic carbon heated with different seeding ratios.

The 2D band in graphitic materials reveals its shape and structural features through changes in stacking order, which become evident in these spectra.[13,145] Significant variations in their spectral profiles are apparent in the Raman 2D bands (Figure 3.14) of graphitized carbon produced with different ratios of graphite seeds. The 2D band shows a single Lorentzian shape without seeding, with a full width at half maximum (FWHM) of about 35 cm^{-1}. According to Eliel et al. the FWHM

of the 2D band in turbostratic carbon is generally around 42 cm^{-1}, while in single-layer graphene it narrows to about 30 cm^{-1}.[146] L.G. Cancado and colleagues further clarified that the presence of a single, unsplit 2D peak indicates weak interlayer interactions. In such cases, the π-electron dispersion remains unsplit, confirming the turbostratic nature of the material.[13] Practically, distinguishing graphene from turbostratic graphite can be challenging since both materials produce a symmetrical Lorentzian 2D peak.[144–146] However, based on moderate I_D/I_G ratios in synthesized samples compared to graphene (I_D/I_G <0.1), this profile is typical of the 2D band that appears in turbostratic graphite, where the graphene layers lack long-range stacking order along the c-axis.[13,144]

As the graphite seed content increases in Figure 3.14, particularly at 3 wt.% and 5 wt.%, the 2D band in the Raman spectrum begins to exhibit a bi-Lorentzian profile, indicating a change in structural properties. The 2D band shape changes from a symmetrical Lorentzian in single-layer graphene to a more complex form involving multiple bands in multi-layer graphite. [144–146] This change reflects the transition from a turbostratic or disordered stacking to a more organized, multilayered graphitic structure. In multilayer graphene and bulk graphite, the 2D band typically splits into two Lorentzian components due to stronger interlayer interactions and the development of three-dimensional stacking.

The appearance of this dual-peak structure indicates improved stacking order in the graphitic carbon due to seeding. However, it is crucial to consider that the graphite seeds themselves might also contribute to the observed 2D band features, potentially affecting the peak splitting and overall spectral shape.

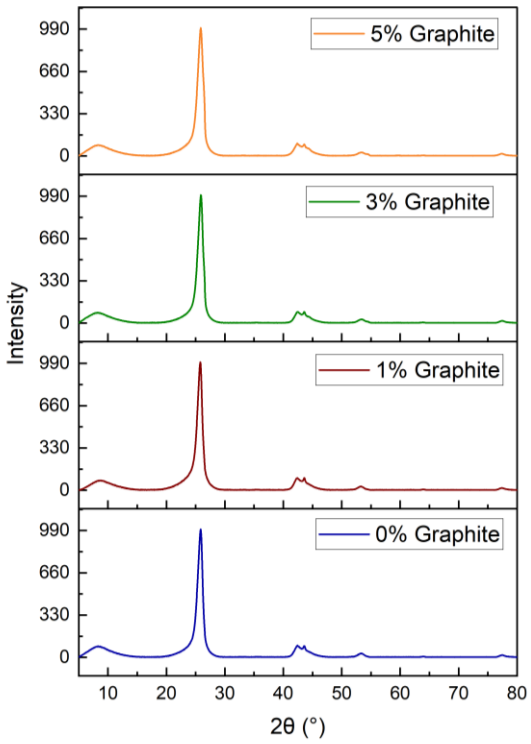

Figure 3.15: XRD patterns of activated carbon graphitized with magnesium at 1000 °C for 24 hours, showing the effect of varying graphite seeding ratios.

Table 3.7: XRD analysis of graphitization with the seeding technique.

Sample	**Peak position (°)**	**$d_{(002)}$ (nm)**	**L_c (nm) (Stacking height)**	**L_a (nm) (Crystallite size)**
MgAC 1000 °C 24 hrs with 5 wt% graphite seeding	25.9	0.3439 ± 0.0001	7.3 ± 0.1	21.8 ± 0.6
MgAC 1000 °C 24 hrs with 3 wt% graphite seeding	25.9	0.3437 ± 0.0007	7.8 ± 0.0	20.9 ± 0.1
MgAC 1000 °C 24 hrs with 1 wt% graphite seeding	25.8	0.3450 ± 0.0002	8.3 ± 0.0	21.7 ± 0.4
MgAC 1000 °C 24 hrs with 0 wt% graphite seeding	25.9	0.3400 ± 0.0001	8.2 ± 0.1	20.7 ± 0.5

The XRD analysis of graphitic carbon synthesized via the seeding technique is shown in Figure 3.15 and Table 3.7. At first glance, all the spectra display the (002) peak, along with the (100), (101), and (004) reflections, indicating the formation of graphitic carbon. The spectral profiles are relatively consistent among the samples in terms of peak sharpness and intensity.

Table 3.7 offers additional details on the structural features of the synthesized carbon. The (002) peak appears between 25.8° and 25.9° in all samples, indicating a turbostratic structure. The narrow range of peak positions, along with similar full widths at half maximum (FWHM) values, yields comparable stacking heights of 7 nm to 8.25 nm, as calculated by the Scherrer equation. The lateral crystallite sizes range from 20 nm to 22 nm, suggesting that the seeding method does not influence the crystallite size.

3.2.3.5. Effect of microwave technology on synthetic graphitization

In our investigation, microwave technology was employed to evaluate the degree of graphitization in comparison to traditional synthetic graphitization methods. The graphitization process, achieved through microwave heating, has shown promise as an alternative to traditional methods.[27,148] Microwave electromagnetic waves transmit energy to target materials at the speed of light while reducing energy loss in the surrounding medium.[149]

The XRD patterns of carbon samples treated with microwave-assisted graphitization at a 2:1 weight ratio of activated carbon to magnesium appear in Figure 3.16. The XRD patterns in subfigures (a), (b), and (c) show different graphitization conditions at 1200 °C for 3 hours, 1200 °C for 1 hour, and 1000 °C for 3 hours. The X-ray diffraction patterns display the (002) peak and (100), (101), and (004) reflections, which confirm graphitic features.

The (002) peak positions and interlayer spacing (d-spacing) values calculated by Bragg's law are shown in Table 3.8. The d-spacing measurements are greater than those of commercial graphite (approximately 0.33 nm), mainly indicating amorphous material. The significant disorder in the material prevented further structural testing.

The Raman spectra of these samples are shown in Figure 3.17. They display both a broad, intense D band and a broad G band, indicating disordered carbon structures. The presence of the 2D band indicates that some layered structure persists. The Raman analysis included the I_D/I_G ratio

measurements, which are recorded in Table 3.9. Based on the calculations, the I_D/I_G ratio was above 1.0 for all three samples, indicating they mainly contained amorphous carbon structures.

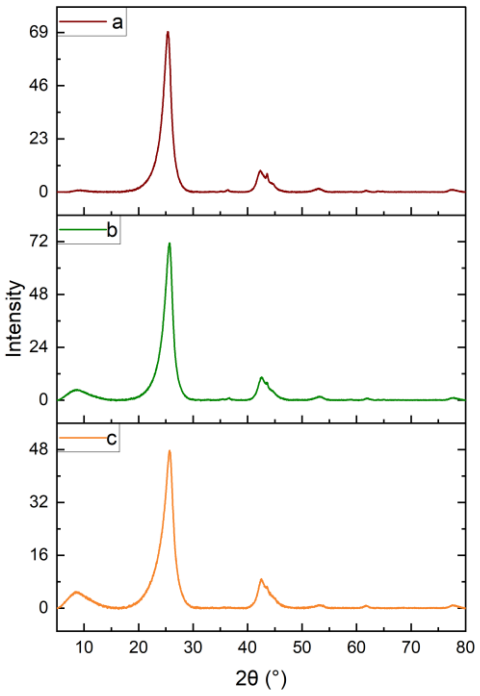

Figure 3.16: XRD analysis of graphitized activated carbon with magnesium (2:1 wt/wt) using microwave technology at various conditions: a) 1200 °C, 3 hrs, b) 1200 °C, 1 hr, c) 1000 °C, 3 hrs.

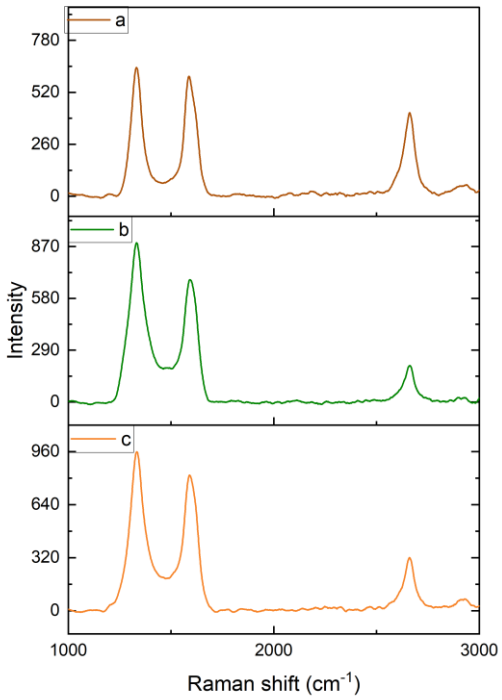

Figure 3.17: Raman spectroscopy analysis of graphitized activated carbon with magnesium (2:1 wt/wt) using microwave technology at various conditions: a) 1200 °C, 3 hrs, b) 1200 °C, 1 hr, c) 1000 °C, 3 hrs.

The 2:1 (wt/wt) activated carbon to magnesium ratio produced minimal graphitization; therefore, the magnesium content was increased to establish a 1:1 (wt/wt) ratio, which represents the composition of the conventional graphitization method discussed in Chapter 3. The research aimed to determine if higher magnesium content would improve microwave absorption and result in better graphitization. The evaluation of structural changes and improvements in graphitic ordering was conducted using XRD and Raman spectroscopy, following the same procedures as in previous experiments.

The XRD patterns of microwave-treated carbon samples with a 1:1 weight ratio of activated carbon to magnesium are shown in Figure 3.18. The three subfigures (a), (b), and (c) represent different graphitization conditions, including 1200 °C for 3 hours, 1200 °C for 1 hour, and 1000 °C for 3 hours. The XRD patterns display both (002) and (100), (101), and (004) reflections, confirming graphitic features.

Compared to the samples with lower magnesium content shown in Figure 3.18, the (002) peak in the microwave-graphitized samples with higher magnesium content exhibits a slight blue shift to 25.8° after a 1200°C treatment for 1 hour. The structure maintains its disordered nature because the d-spacing remains large but shows a slight reduction compared to the low-magnesium samples.

Raman analysis results, summarized in Table 3.9, show the lowest I_D/I_G ratio of 0.75 ± 0.07 after 3 hours of microwave treatment at 1200 °C, indicating a slight improvement in structural order. The broad and poorly separated D and G bands in all spectra confirm that the carbon remains primarily in an amorphous state.

The XRD and Raman analysis results indicate that microwave-assisted graphitization under these conditions failed to produce rapid or significant graphitic ordering.

Table 3.8: XRD analysis of microwave-assisted graphitization.

Sample	**(002) Peak position (°)**	**$d_{(002)}$ (nm)**
MW graphitized AC with Mg (1:1) 1000 °C 3 hrs	25.83	0.3446
MW graphitized AC with Mg (1:1) 1200 °C 1 hr	25.83	0.3446
MW graphitized AC with Mg (1:1) 1200 °C 3 hrs	25.79	0.3452
MW graphitized AC with Mg (2:1) 1000 °C 3 hrs	25.67	0.3468
MW graphitized AC with Mg (2:1) 1200 °C 1 hr	25.73	0.3460
MW graphitized AC with Mg (2:1) 1200 °C 3 hrs	25.34	0.3512

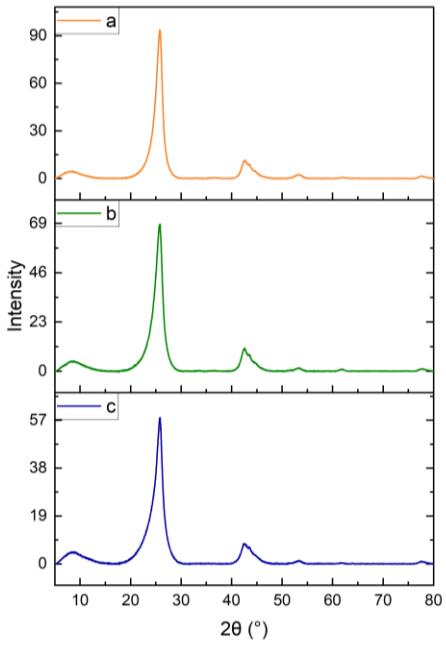

Figure 3.18: XRD analysis of graphitized activated carbon with magnesium (1:1 wt/wt) using microwave technology at various conditions: a) 1200 °C, 3 hrs, b) 1200 °C, 1 hr, c) 1000 °C, 3 hrs.

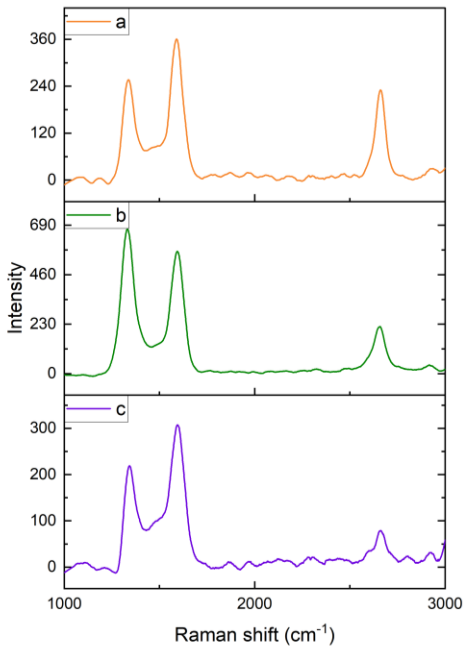

Figure 3.19: Raman spectroscopy analysis of graphitized activated carbon with magnesium (1:1 wt/wt) using microwave technology at various conditions: a) 1200 °C, 3 hrs, b) 1200 °C, 1 hr, c) 1000 °C, 3 hrs.

Table 3.9: Raman analysis of microwave-assisted graphitization.

Sample	I_D/I_G ratio
MW graphitized AC with Mg (1:1) 1000 °C 3 hrs	0.75 ± 0.07
MW graphitized AC with Mg (1:1) 1200 °C 1 hr	1.28 ± 0.16
MW graphitized AC with Mg (1:1) 1200 °C 3 hrs	0.71 ± 0.19
MW graphitized AC with Mg (2:1) 1000 °C 3 hrs	1.19 ± 0.05
MW graphitized AC with Mg (2:1) 1200 °C 1 hr	1.24 ± 0.15
MW graphitized AC with Mg (2:1) 1200 °C 3 hrs	1.09 ± 0.14

3.2.4. Textural characterization

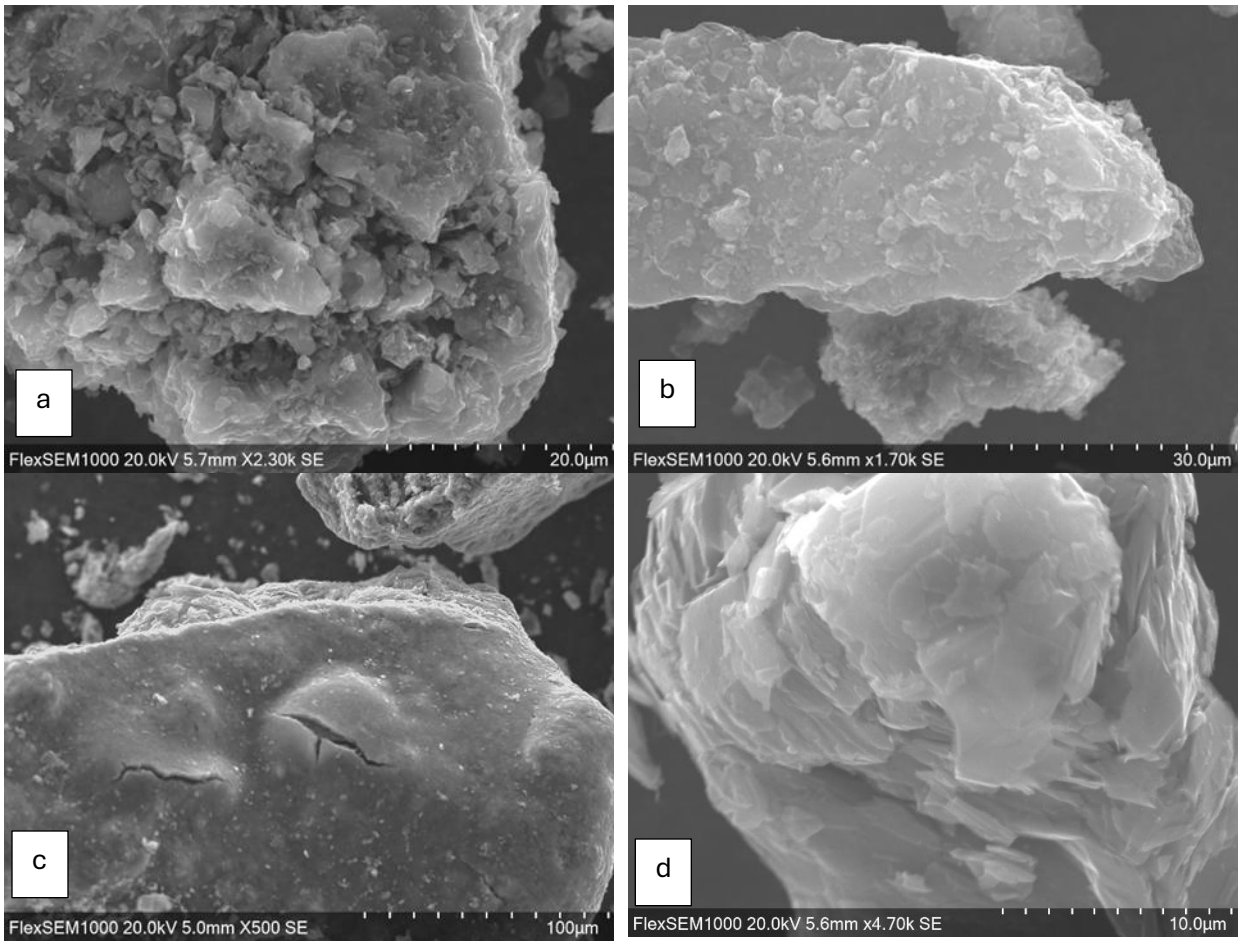

Figure 3.20: SEM images of a) heated petroleum coke without magnesium, b) graphitized activated carbon, c) graphitized petroleum coke at 1000 °C for 3 hours, d) graphite (Sigma Aldrich).

The surface morphology and structural arrangement of graphitic carbon were studied using SEM imaging. Figure 3.20 compares the morphology of heated petroleum coke without magnesium, magnesium-assisted graphitized products, and commercial synthetic graphite. SEM analysis effectively improves our understanding of the effect of magnesium on the graphitization process. The surface of heated petroleum coke without magnesium, heated at 1000 °C for three hours, appears coarse. Many small particles cluster on the surface, aligning with Raman and XRD

observations of this material's amorphous characteristics. The surface of graphitized activated carbon (MgAC 1000 °C, 3 hours) appears smoother, with fewer tiny particles visible. The appearance of a more pronounced lamellar structure indicates the formation of graphitic structures. Figure 3.20c shows the surface morphology of graphitized petroleum coke (MgPC 1000 °C, 3 hours), where cracks are visible, although the rest of the surface area is smoother than that of the heated petroleum coke blank. The cracks may result from sulfur removal, as petroleum coke contains 5-7 wt% sulfur.[1] Figure 3.20d shows a scanning electron micrograph of commercial graphite, emphasizing its smooth surface and the fine, tightly packed layers. This microstructure indicates a highly ordered crystalline structure, typical of well-graphitized carbon materials. The absence of visible porosity, cracks, or irregular features.[18,27,150]

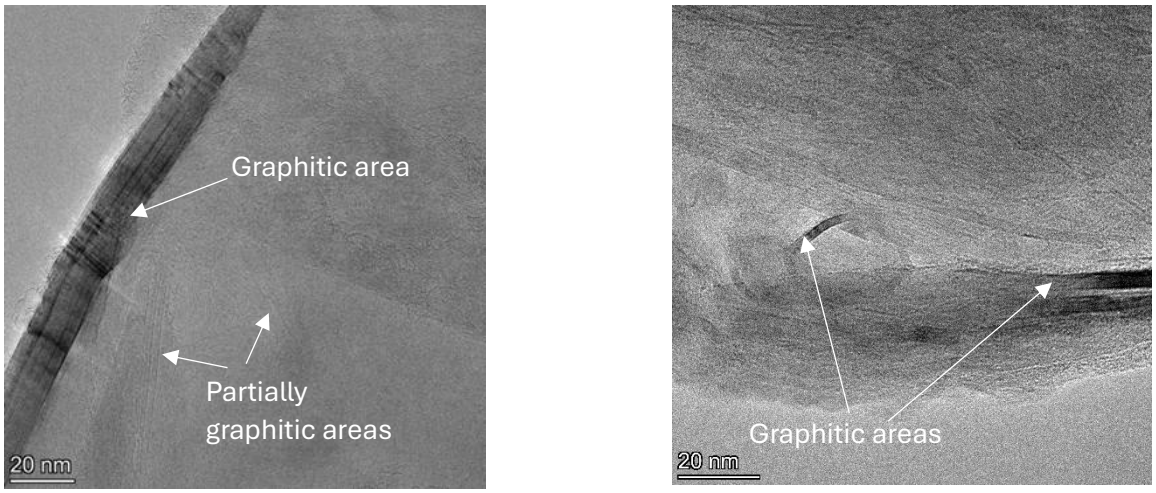

Figure 3.21: TEM images of graphitized activated carbon sample at 1000 °C for 24 hours (MgAC 1000 °C, 24 hours).

TEM images were taken of the graphitized activated carbon sample (MgAC 1000 °C, 24 hours), which showed the highest degree of graphitization and a lower level of disorder as determined by XRD and Raman spectroscopy analyses. Figure 3.21 illustrates the formation of graphitic ribbons forming layered structures. Additionally, partially stacked layers are visible as lighter layered structures, indicating polycrystallinity. However, amorphous carbon structures coexist with graphitic structures, supporting the structural analyses.

Table 3.10: Surface area analysis of graphitized activated carbon with magnesium at different dwell times.

Sample	**BET surface area (m^2/g)**	**Total pore volume (cm^3/g)**	**Micropore volume (cm^3/g)**	**Mesopore volume (cm^3/g)**
MgAC 1000 °C, 24 hrs	47.3 ± 1.0	0.1 ± 0.0	0.002 ± 0.000	0.06 ± 0.00
MgAC 1000 °C, 12 hrs	192.7 ± 29.2	0.2 ± 0.0	0.02 ± 0.01	0.15 ± 0.03
MgAC 1000 °C, 6 hrs	262.7 ± 9.5	0.2 ± 0.1	0.05 ±0.01	0.17 ± 0.06
MgAC 1000 °C, 3 hrs	259.6 ± 9.2	0.3 ± 0.1	0.04 ± 0.00	0.26 ± 0.05
MgAC 1000 °C, 30 mins	277.3 ± 0.4	0.2 ± 0.0	0.04 ± 0.00	0.18 ± 0.00
Activated carbon (precursor)	1260.3	0.5	0.43	0.10
Commercial graphite	7	Non-detectable	Non-detectable	Non-detectable

The surface area, total pore volume, and micropore volume were measured to gain further insights into the arrangement of the porous structure and the graphitization process. Table 3.10 presents the characteristics of graphitized activated carbon (MgACs) samples heated at 1000 °C for different durations. Overall, the surface area decreased during the graphitization process, which aligns with the inherently low surface area of commercial graphite (~7 m^2/g), indicating the formation of more ordered, compact structures. The activated carbon precursor has a surface area of 1260.3 m^2/g, which drops to (277.3 ± 0.4) m^2/g after just 30 minutes of graphitization with magnesium. This decrease in surface area occurs because pores collapse during graphitization, which lowers the level of disorder. Overall, the surface area decreases with more graphitization time. Notably, there is no significant change in surface area until 6 hours. However, the graphitization of activated carbon after 12 hours shows a substantial reduction in surface area to (192.7 ± 29.2) m^2/g.

Interestingly, the standard deviation increases again at this stage. The lowest surface area is recorded as (47.3 ± 1.0) m^2/g after 24 hours of graphitization at 1000 °C. The transition stages of porous structure reduction, such as 12 hours of graphitization, contain a wider range of porous structures as indicated by the standard deviation. Additionally, the plateau of graphitization was supported by the lowest standard deviation observed at 24 hours. The average total pore volume and micropore volume measurements also follow the same pattern. Specifically, there is a sharp drop in micropore volume from 0.43 cm^3/g to (0.04 ± 0.00) cm^3/g after 30 minutes of graphitization. Interestingly, the MgAC 1000 °C, 24 hours sample exhibits the lowest average total pore volume and micropore volume, measuring (0.1 ± 0.0) and (0.002 ± 0.00) cm^3/g, respectively. The zero standard deviation here highlights the uniformity of the structure.

In contrast, the surface area and pore volume analysis agree with the Raman spectroscopy results. The MgAC sample heated to 1000 °C for 24 hours had the lowest I_D/I_G ratio and, consequently, the lowest surface area and pore volume. This indicates that as the carbon structure reorganizes and the level of disorder decreases, both the surface area and pore volume decline.

3.2.5. Electrical Conductivity

Table 3.11: Electrical conductivity of MgAC and MgPC pellets.

Sample	**Conductivity (S/m) at 10 mA**	**Sample**	**Conductivity (S/m) at 10 mA**
MgAC 1000 °C, 24 hrs	3552 ± 79	MgPC1000 °C, 24 hrs	1118 ± 0
MgAC 1000 °C, 12 hrs	2548 ± 40	MgPC 1000 °C, 12 hrs	1061 ± 0
MgAC 1000 °C, 6 hrs	1485 ± 35	MgPC 1000 °C, 6 hrs	1014 ± 0
MgAC 1000 °C, 3 hrs	1252 ± 8	MgPC 1000 °C, 3 hrs	870 ± 0
MgAC 1000 °C, 30 mins	1258 ± 14	MgPC 1000 °C, 30 mins	830 ± 5
Activated carbon (precursor)	Non-conductive	Petroleum coke (precursor)	Non-conductive
Commercial graphite (Sigma Aldrich)	7374 ± 0		

The electrical conductivity increases as the degree of graphitization in carbon products rises, although contaminants can affect conductivity. The formation of a graphitic structure creates pathways for electrical conductivity through delocalized electrons. Table 3.11 shows that the increase in electrical conductivity of pelletized MgAC and MgPC samples coincides with longer dwell times. In MgAC pellets, the lowest electrical conductivity measured is (1252 ± 8) S/m after 3 hours of graphitization at 1000 °C. A higher level of disorder, as indicated by Raman and surface area analysis, can impede conductive pathways. The electrical conductivity reaches a plateau at 3 hours and only slightly increases after 6 hours of graphitization (1485 ± 35) S/m. The highest electrical conductivity is expected in the graphitized activated carbon sample that has been processed for 24 hours. This pellet recorded an electrical conductivity of (3552 ± 79) S/m, nearly half of a commercial graphite pellet's conductivity (7374 ± 0) S/m. It's crucial to attain high electrical conductivity through a moderate temperature graphitization process.

In contrast, graphitized petroleum coke samples show relatively lower electrical conductivity at each graphitization time compared to graphitized activated carbon pellets. For example, the MgPC 1000 °C, 24 hrs sample exhibited nearly one-third of the electrical conductivity of the MgAC 1000 °C, 24 hrs pellet. It is worth noting that the graphitized petroleum coke sample, heated to 1000 °C for 24 hours, exhibited a lower degree of disorder, as determined by Raman spectroscopy analysis. However, despite these similarities, the activated carbon samples demonstrated better crystallite development, which enhances electron mobility through the delocalized π-electron cloud, a key factor in electrical conductivity.[9,11,134,151] Additionally, a significant percentage of contaminants, especially sulfur in petcoke, impairs the electrical conductivity of graphitic carbons. The chemical composition of petroleum coke is discussed thoroughly in Chapter 5. In summary, the purity and structural refinement of graphitized carbon materials are crucial for their electrical conductivity, with activated carbon having a clear edge in crystallite formation and electron transport efficiency.

3.3. Summary

This chapter aims to identify the specific performance of magnesium as a metal catalyst in the graphitization of petroleum coke and activated carbon, thereby reducing process time and heat requirements. The research examines multiple variables, including temperature, duration, particle size, seeding methods, and microwave-assisted heating, to assess their effects on both graphitization levels and the structural transformations of carbon materials.

The low melting point of magnesium makes it a suitable choice because it promotes the graphitization process at moderate temperatures. Research data showed that graphitization with magnesium is effective at 1000 °C, where prolonged heat exposure (up to 24 hours) increases the carbon's structural order to turbostratic levels. Raman spectroscopy combined with XRD analysis revealed that graphitic domains formed more prominently in petroleum coke than in activated carbon, based on I_D/I_G ratios and structural crystallinity measurements.

Medium-sized carbon precursor particles generated the most advantageous graphitic structures because they created a perfect link between surface area and metal-carbon bond strength. The seeding approach, which included small additions of synthetic graphite, showed limited nucleation but improved stacking order. However, the 2D band profiles indicated more noticeable enhancements in stacking layers than changes in the I_D/I_G ratio. The analysis of microwave-assisted graphitization showed limited structural ordering even when the magnesium content was increased under current conditions.

The morphological investigations using SEM and TEM were conducted only on MgAC and MgPC samples produced by conventional heating. Spectroscopic analyses indicate that graphitized activated carbon with magnesium forms layered graphitic structures, while its porosity gradually decreases. Electrical conductivity measurements reveal a direct correlation with the degree of graphitic ordering. The 24-hour graphitization process at 1000 °C produced activated carbon samples with conductivities approximately half those of commercial graphite. In contrast, petroleum coke samples maintained lower conductivities due to sulfur-based impurities.

Overall, the findings of this chapter confirm magnesium as an effective catalyst for moderate-temperature graphitization, offering valuable insights into process improvements and material behaviour for future energy storage and conductive carbon applications.

4. Raney nickel alloy-assisted graphitization of activated carbon: Efficacy of bimetallic mediators in graphitization

4.1 Introduction

This section assesses the efficacy of bimetallic alloys using the aluminum-nickel (Al-Ni) system in promoting synthetic graphitization and enhancing structural ordering in carbon materials. Bimetallic alloys have attracted broad interest because of their versatile uses[7] across hydrogen production,[70] production of carbon nanotubes and hydrodeoxygenation reactions.[69]

A notable example is the Raney nickel catalyst, which is produced by selectively leaching aluminum from binary Al-Ni alloys using aqueous alkaline solutions.[76] This process produces a high surface area nickel structure that greatly enhances catalytic activity.[110]

Our focus is on the binary Al-Ni precursor alloy with an equal (1:1) ratio of aluminum to nickel. The performance of this alloy in promoting graphitization was examined using activated carbon (purified petroleum coke), which was previously shown in Chapter 3 to outperform untreated petcoke in facilitating graphitic transformations.

In this chapter, we assess the efficacy of Raney nickel alloy as a metal mediator in the graphitization of activated carbon. A detailed overview of experimental methods, including synthesis procedures and characterization techniques used to evaluate the resulting graphitic materials, is provided. For clarity, the Al-Ni precursor alloy will be designated as Raney nickel alloy, and graphitic materials synthesized from mixtures of activated carbon and Raney nickel alloy will be referred to as Raney nickel alloy-assisted graphitized activated carbon (RNiACs) throughout the discussion.

4.1.1 Bimetallic mediator: Raney nickel alloy

Raney nickel, first developed by Murray Raney in 1927, is synthesized by dissolving nickel in molten aluminum using pyrometallurgical methods at a 1:1 mass ratio, followed by a rapid quenching step. Next, aluminum is selectively leached from the nickel-aluminum alloy with concentrated bases such as sodium hydroxide or potassium hydroxide. The resulting nickel product is highly porous and exhibits a unique metallic framework. This process creates a three-

dimensional metallic nickel matrix embedded with residual aluminum and voids resulting from the removal of aluminum, leading to an extensive surface area. This high surface area (~53 m^2/g) significantly contributes to the exceptional catalytic performance of Raney nickel, especially in the heterogeneous hydrogenation of organic reactions.[76,110]

Beyond hydrogenation, nickel has also shown a significant effect on the graphitization of disordered carbon, while aluminum's role in such processes has been minimal. Before leaching, the Raney nickel alloy contains roughly equal weight fractions of nickel and aluminum (50 wt.% each), making it a promising bimetallic system for synthetic graphitization.[6,35,37]

In Chapter 3, we established that activated carbon (purified petcoke) enables the formation of ordered carbon structures at a relatively modest temperature of 1000 °C, significantly lower than the typical synthetic graphitization conditions (>2500 °C). Building on these findings, Chapter 4 introduces the use of Raney nickel alloy in promoting the graphitization of activated carbon. To our knowledge, this represents a novel application of Raney nickel alloy in the synthesis of graphite. This chapter thoroughly analyzes the efficacy of Raney nickel alloy in improving the structural order and graphitic content of activated carbon.

4.2. Experimental

4.2.1. Synthesis of graphite incorporating Raney nickel

Activated carbon was ground for 15 minutes with Raney nickel alloy (Sigma-Aldrich) in a 1:1 carbon-to-metal mass ratio using a mortar and pestle. The schematic diagram of the graphitization process is displayed in Figure 4.1. These resulting mixtures were placed in closed alumina crucibles and heated in nitrogen at 1400 °C, 1500 °C, and 1600 °C in the tube furnace (CARBOLITE GERO) to determine the optimal working temperature. Graphitization was further refined by adjusting dwell times from 1 hour to 12 hours at the chosen temperature. The heating and cooling rates were set to 4 °C per minute. For the post-graphitization treatment, approximately 8 g of heated RNiAC mixture was reacted with 150 ml of 3M HCl (prepared from 37 wt.% HCl, Sigma Aldrich) and stirred for 2 hours at 80 °C. Afterwards, the products were vacuum filtered and thoroughly washed with deionized water. This was followed by a base treatment, where 50 ml of 20% KOH (~4.31 M) was reacted at 80 °C for 2 hours to remove any residual aluminum or aluminum oxide. Subsequently, the products were filtered and washed repeatedly with deionized

water until the pH of the supernatant reached about 6.5 to 7. Finally, the products were air-dried overnight at 120 °C.

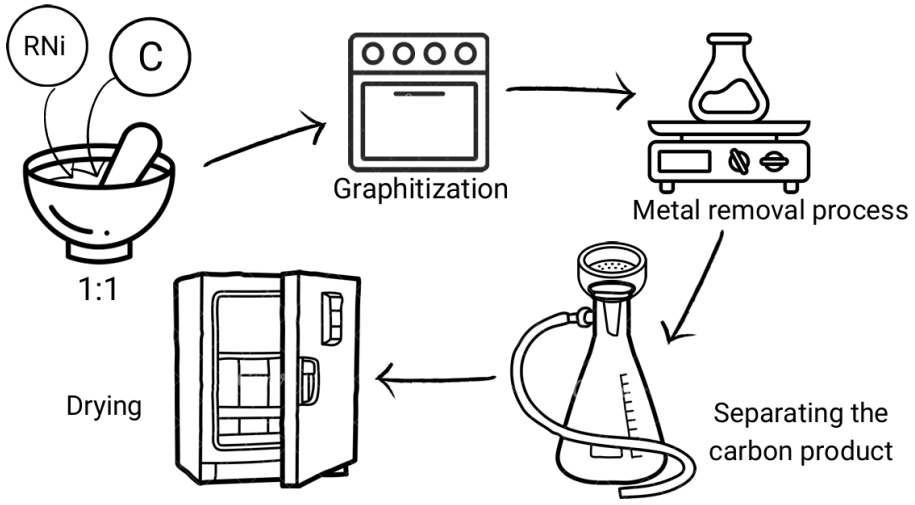

Figure 4.1: Schematic diagram of Raney nickel-assisted graphitization process.

4.2.2. Electrical conductivity

Pelletization and electrical conductivity measurements were performed using the same procedure outlined in Section 3.2.2.

4.2.3. Characterization

The synthesized carbon products were characterized using several techniques, including Raman spectroscopy, X-ray diffraction (XRD), Brunauer-Emmett-Teller (BET) surface area analysis, X-ray photoelectron spectroscopy (XPS), and four-point probe. These techniques are comprehensively discussed in Chapter 2.

4.3. Structural Characterization

4.3.1. Effect of temperature on the graphitization process

The study on temperature optimization aimed to identify the optimal conditions for enhanced graphitization. The temperature must exceed the metal's melting point to enable the dissolution-precipitation mechanism.[31] Although pure nickel melts at 1455 °C, the exact melting point of commercial Raney nickel alloy has not been reported. Therefore, the experimental temperature range started at 1400 °C and increased to 1600 °C. The heat treatment was performed at 1400 °C, 1500 °C, and 1600 °C to observe potential changes across this temperature range. The resulting

materials are named RNiAC 1400 °C 3hrs, RNiAC 1500 °C 3hrs, and RNiAC 1600 °C 3hrs, indicating their synthesis temperatures and processing durations.

The Raman spectral analysis of Raney nickel alloy-assisted graphitization of activated carbon at different temperatures for three hours appears in Figure 4.2. The Raman spectrum of the 1400 °C-treated sample (RNi AC 1400 °C 3hrs) revealed two broad peaks, indicating the graphitic structure was not well developed at this temperature.

Interestingly, the structural order improved significantly when the temperature reached 1500 °C, as indicated by the D and G bands becoming more distinct and sharper. The corresponding I_D/I_G ratio measured 0.84 ± 0.22, indicating a decrease in disorder. Although the I_D/I_G ratio increased to 0.91 ± 0.19 at 1600 °C, the improvement in graphitic order remained minimal after 1500 °C. The results suggest that the optimal graphitization occurs at 1500 °C, and heating beyond this temperature does not provide substantial benefits under the current treatment duration.

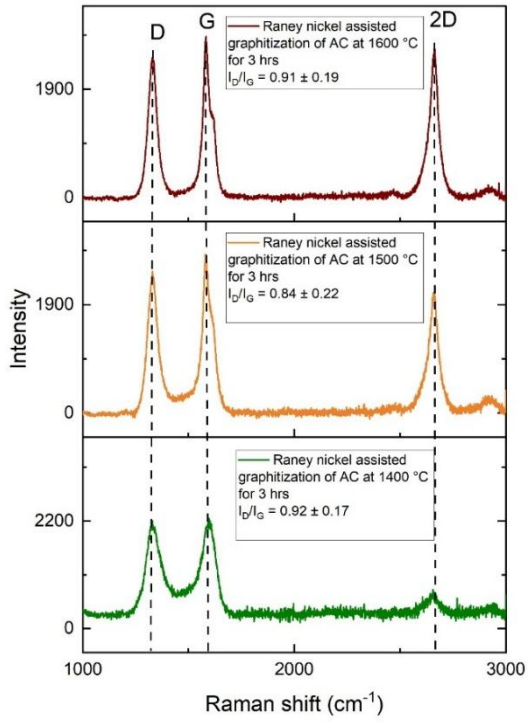

Figure 4.2: Raman spectroscopy analysis of Raney nickel assisted graphitization over temperature.

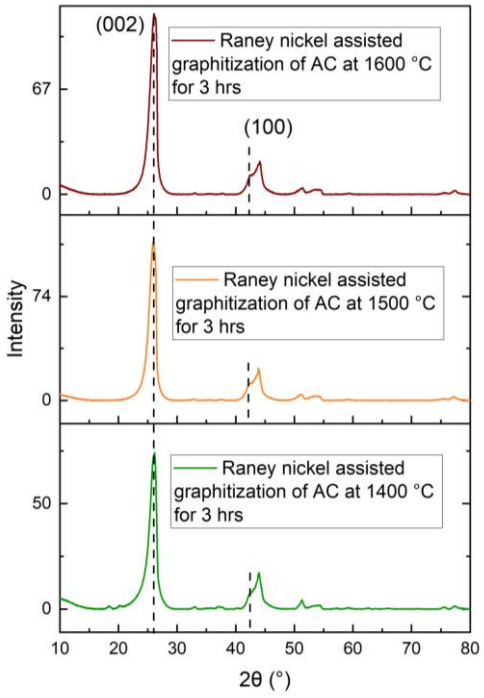

Figure 4.3: XRD analyses of Raney nickel assisted graphitization of activated carbon over various temperatures.

Table 4.1: Crystal structure analysis of Raney nickel alloy-assisted graphitization over temperature based on XRD.

Sample	**Peak position of (002) peak (°)**	**$d_{(002)}$ (nm)**	**L_c (nm) (Stacking height)**	**L_a (nm) (Crystallite size)**
RNi AC, 1400 °C, 3 hrs	25.8 ± 0.5	0.3457 ± 0.0007	6.7 ± 0.0	14.7 ± 1.1
RNi AC, 1500 °C, 3 hrs	26.1 ± 0.2	0.3413 ± 0.0006	13.6 ± 0.2	18.9 ± 2.1
RNi AC, 1600 °C, 3 hrs	26.1 ± 0.4	0.3418 ± 0.0009	13.1±1.3	18.0 ± 3.8

Figure 4.3, the X-ray diffraction (XRD) patterns of activated carbon samples subjected to Raney nickel alloy-assisted graphitization across various temperature profiles. Structural parameters, including interlayer spacing ($d_{(002)}$), the stacking height (L_c), and the crystallite size (L_a), were evaluated and summarized in Table 4.1. To obtain these values, the (002) peak and (100) diffraction peaks were analyzed using Voigt profile fitting. The stacking height (L_c) was derived from the (002) reflection, while the crystallite size (L_a) was obtained from the (100) peak.[151]

A significant reduction in the average interlayer spacing ($d_{(002)}$) was observed at 1500 °C, reaching (0.3413 ± 0.0006) nm after 3 hours of thermal treatment. In contrast, a broader spacing of (0.3457 ± 0.0007) nm was recorded at 1400 °C, indicating the presence of amorphous carbon. When the temperature was increased to 1600 °C, the $d_{(002)}$ value increased slightly to (0.3418 ± 0.0009) nm, compared to 1500 °C. Although the change in $d_{(002)}$ was minimal, this can be attributed to the structural inconsistency of the precursor and the limited extent of amorphous-to-crystalline transformation during the fixed 3-hour dwell time.

This trend is also reflected in the crystallographic parameters: both the average stacking height (L_c) and the average crystallite size (L_a) showed a similar progression. The lowest values for these parameters were observed in the sample treated at 1400 °C, which aligns well with the Raman spectroscopy findings, indicating minimal graphitic ordering at this temperature. As the temperature increases, both the average L_c and L_a values improve significantly, stabilizing around

1500 °C. Under this optimal condition, the highest average L_c and L_a values recorded were (13.6 ± 0.2) nm and (18.9 ± 2.1) nm at 1500 °C, respectively.

These results verify a strong correlation between the XRD and Raman analyses, as both indicated that 1500 °C is the most effective temperature for promoting graphitic structure formation in the presence of Raney nickel alloy. Based on these findings, 1500 °C was chosen for further studies on dwell time optimization, which are discussed in detail in the next section.

4.3.2. Effect of dwell time on the graphitization process

The Raman spectra of activated carbon treated with Raney nickel alloy at 1500 °C are shown in Figure 4.4, where the sample undergoes various dwell time durations. All carbon products underwent a washing treatment before Raman spectroscopy to eliminate remaining metallic substances. The graphitization of the activated carbon mixture with Raney nickel alloy was carried out for 1, 3, 6, and 12-hour periods. The G peak, along with the 2D peak, indicates the formation of crystalline carbon structures. The one-hour sample shows a low-intensity, broad 2D peak, along with wide D and G bands. The corresponding I_D/I_G ratio is recorded at 1.15 ± 0.11. The broad peaks and minimal 2D peak intensity result from insufficient graphitization and the formation of small graphene structures. The higher I_D/I_G ratio is consistent with the fact that the first hour of the process did not produce significant graphitization.

Raman spectroscopy reveals that the 2D peak intensity increases over time at 1500 °C, indicating the formation of graphene-like structures. Heat treatment for three hours results in a decrease in the I_D/I_G ratio to 0.84 ± 0.22, indicating a reduction in structural disorder. Notably, the ratio ranges from 0.58 to 1.10, suggesting that the sample contains both ordered and disordered carbon domains.

The Raman bands became more intense and sharper over longer heating times, indicating better structural ordering. The I_D/I_G ratio was recorded at 0.64 ± 0.53 after 6 hours; however, this value varied widely across five measured samples, ranging from 0 to 1.34. The ratio close to zero suggests the formation of highly ordered carbon domains matching pristine graphite structures for the first time in this series. The I_D/I_G ratio showed a decrease in standard deviation after 12 hours, with an average value of 0.74 ± 0.23. The improved consistency, along with reduced intensity ratios of the D peak and the G peak, occurred between 0.48 and 0.98.

The extended graphitization process at 1500 °C, using a Raney nickel alloy (1:1 wt./wt.), produces structurally ordered carbon with improved reproducibility, as indicated by consistent D and G peak intensity ratios.

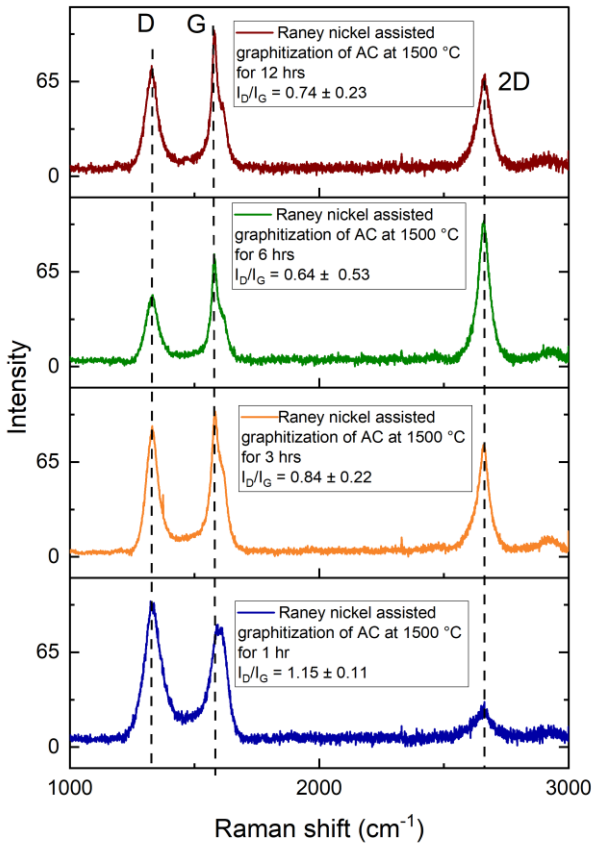

Figure 4.4: Raman spectroscopy analysis of Raney nickel-assisted graphitization over time.

Figure 4.5 (a) displays the XRD analysis of the Raney nickel alloy-assisted samples. The (002) peak and (100) peaks were fitted using Voigt profiles to determine the stacking height (L_c) and crystallite size (L_a), respectively. The (002) peaks in Figure 4.5 (b) were fit using the Voigt functions between the angles 22° and 29°, with a combination of multiple Voigt peaks with positions in the range of 25.5°-26.5°, indicating the polycrystallinity in the synthesized carbon products. Interestingly, a sharp Voight peak appears at 26.5° of the 2θ position after 6 hours of graphitization, which is characteristic of pristine graphite. These results align with the Raman spectroscopy analysis of the samples, which showed signals of pristine graphite.

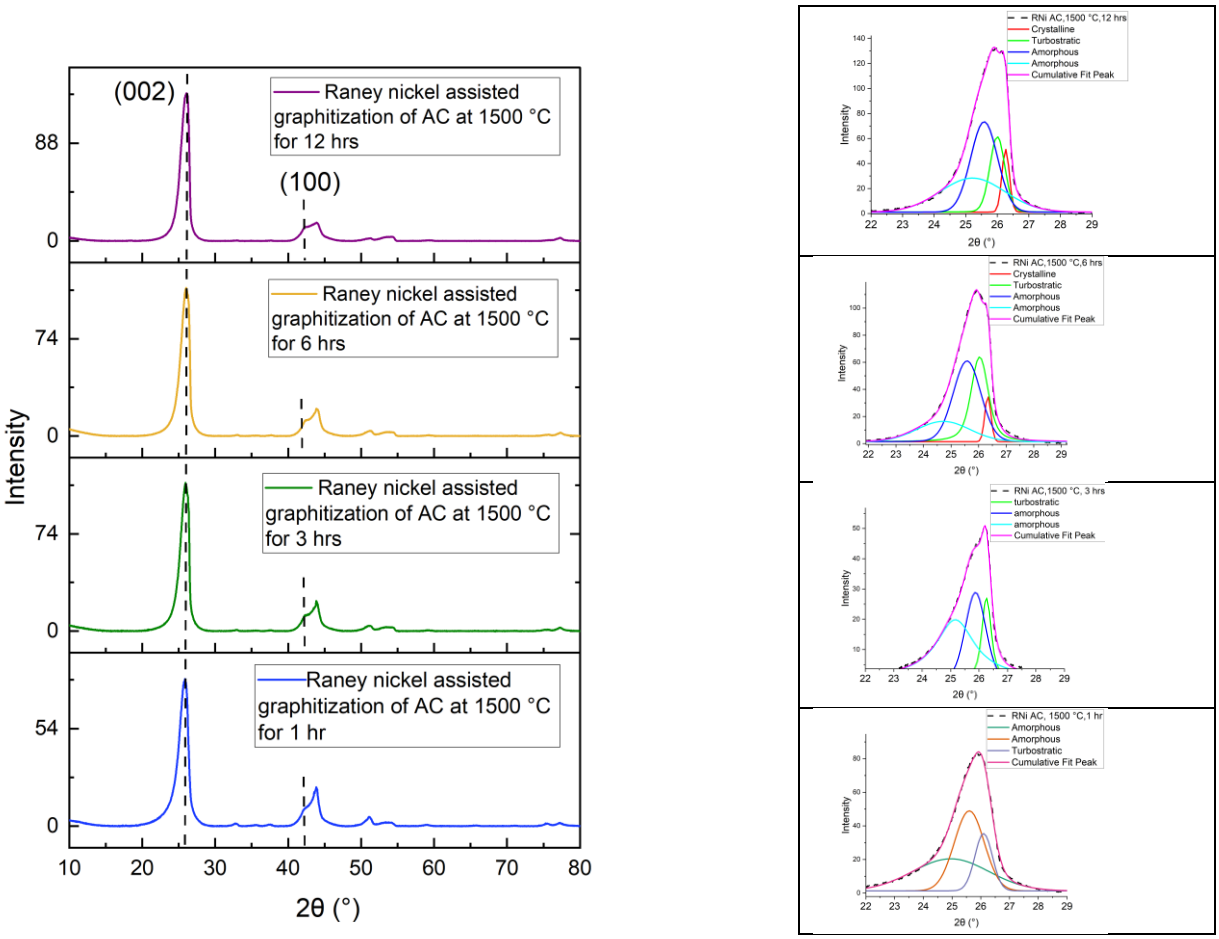

(a) (b)

Figure 4.5: a) XRD analysis of Raney nickel assisted graphitization of activated carbon over various dwell times b) Fitted (002) peaks using Voigt profiles.

Table 4.2: Crystal structure analysis of Raney nickel alloy-assisted graphitization over time based on XRD.

Sample	**Peak position of (002) peak (°)**	**$d_{(002)}$ (nm)**	**L_c (nm) (Stacking height)**	**L_a (nm) (Crystallite size)**
RNi AC, 1500 °C, 1 hr	25.9 ± 0.0	0.3441 ± 0.0003	5.7 ± 0.0	9.6 ± 0.2
RNi AC, 1500 °C, 3 hrs	26.1 ± 0.2	0.3413 ± 0.0006	13.6 ± 0.2	18.9 ± 2.1
RNi AC, 1500 °C, 6 hrs	26.0 ± 0.3	0.3417 ± 0.0002	20.2 ± 11.3	11.4 ± 1.1
RNi AC, 1500 °C, 12 hrs	26.0 ± 0.4	0.3417 ± 0.0000	20.5 ±7.3	11.0 ± 0.6

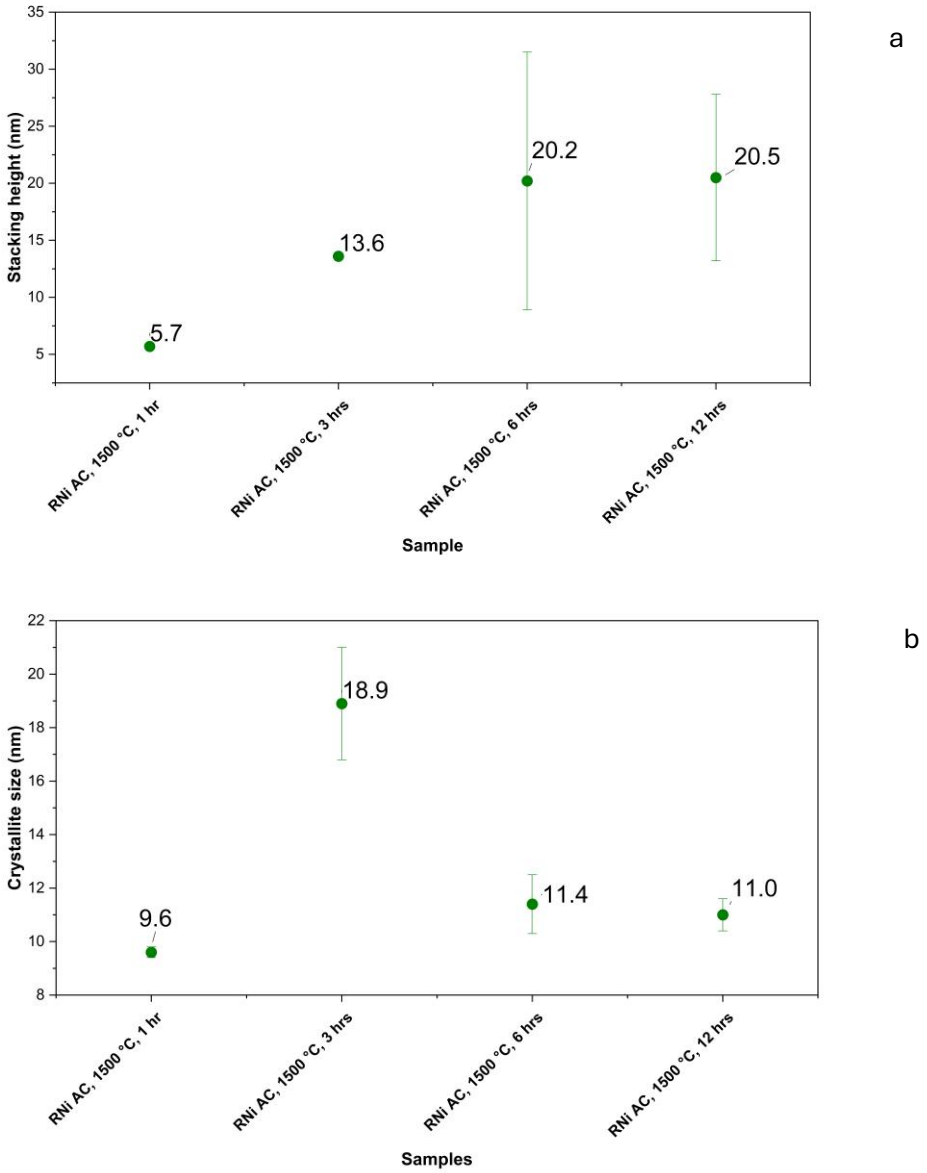

Figure 4.6: a) the average stacking height (L_c), and b) the average crystallite size (L_a).

Based on the fitting results, key structural parameters, including interlayer spacing ($d_{(002)}$), stacking height (L_c), and crystallite size (L_a), were evaluated and are presented in Table 4.2 and Figure 4.6. As the heat treatment duration increased, a higher degree of graphitization was achieved. Table 4.2 shows how the interlayer spacing ($d_{(002)}$) values vary at different dwell times at 1500 °C. The decrease in $d_{(002)}$ from 1-hour to 3-hour dwell time was 0.0028 nm. After 6 hours, the average $d_{(002)}$ stabilizes at around 0.3417 nm. However, there was a significant standard deviation, attributed to

the polycrystalline nature of the synthesized products. For example, at the 6-hour point, $d_{(002)}$ ranges from 0.3369 nm to 0.3480 nm, indicating a coexistence of pristine and amorphous carbon.

The standard deviation of $d_{(002)}$ shows a slight decrease after 12 hours of heat treatment, indicating improved structural uniformity. The development of structural parameters such as the average stacking height (L_c) and the average crystallite size (L_a) values, as shown in Figure 4.6 a) and Figure 4.6 b) respectively. The average L_c appeared to level off after 6 hours of heat treatment, reaching (20.24 ± 11.34) nm. A significant standard deviation persisted in L_c analysis, ranging from 5.60 nm to 33.42 nm, again indicating the polycrystalline nature of the material. After 12 hours of graphitization, the standard deviation decreased slightly, with an average L_c of (20.46 ± 7.28) nm.

The crystallite size (L_a) generally increased with longer dwell times. The highest average value of L_a, (18.90 ± 2.05) nm, was observed after 3 hours of graphitization. However, this value did not follow the expected trend and was not seen at 6 or 12 hours. As a result, the 3-hour data points were considered outliers and excluded from trend analysis. Such deviations may result from the intrinsic polycrystallinity of the samples and limitations in peak fitting, where even minor discrepancies in XRD analysis can lead to significant variations in calculated parameters. Overall, the average L_a stabilized after 6 hours of heat treatment at 1500 °C.

4.4. Textural characterization

The analysis of surface area, total pore volume, and micropore volume of Raney nickel alloy-assisted graphitization of activated carbon products at 1500 °C (RNi AC, 1500 °C) is summarized in Table 4.3 with the average specific surface area, average total pore volume, and average micropore volume of synthesized carbon products over various dwell times.

The average surface area of activated carbon decreased markedly from 1260.3 m^2/g to (280.0 ± 7.3) m^2/g after just 1 hour of Raney nickel alloy-assisted graphitization at 1500 °C. As the heating time increased, the specific surface area further decreased to (205.8 ± 0.8) m^2/g after 3 hours of graphitization. A higher standard deviation indicates a partial collapse of pores in activated carbon. The overall pattern shows that the specific surface area decreases with increasing dwell time. The

lowest average surface area was recorded at 12 hours, measuring (185.3 ± 6.2) m^2/g. Interestingly, the average surface area after 6 hours of graphitization (optimal conditions) is (196.6 ± 10.5) m^2/g.

Table 4.3: Surface area analysis of graphitized activated carbon with Raney nickel alloy at different dwell times.

Sample	**Specific surface area (m^2/g)**	**Total pore volume (cm^3/g)**	**Micropore volume (cm^3/g)**	**Mesopore volume (cm^3/g)**
RNi AC, 1500 °C, 1 hr	280.0 ± 7.3	0.26 ± 0.03	0.03 ± 0.00	0.23 ± 0.03
RNi AC, 1500 °C, 3 hrs	205.8 ± 0.8	0.18 ± 0.05	0.02 ± 0.00	0.14 ± 0.05
RNi AC, 1500 °C, 6 hrs	196.6 ± 10.5	0.20 ± 0.03	0.02 ± 0.00	0.19 ± 0.03
RNi AC, 1500 °C, 12 hrs	185.3 ± 6.2	0.20 ± 0.03	0.01 ± 0.00	0.18 ± 0.03
Activated carbon (precursor)	1260.3	0.53	0.43	0.10

The average total pore volume stabilized at about 0.2 cm^3/g after 3 hours of graphitization. By 12 hours, the average total pore volume remained unchanged, indicating stability in the pore network structure. In contrast, the initial micropore volume of activated carbon was measured at 0.43 cm^3/g. A significant reduction in microporosity was observed following graphitization, as presented in Table 4.3. After just 1 hour of heat treatment, the micropore volume decreased by about 90%, indicating that the Raney nickel alloy-assisted graphitization process begins rapidly within the first hour.

The evolution of micropore volume with increasing dwell time mirrored the trend observed for the specific surface area. Both parameters showed a significant decline with prolonged heat treatment, especially up to 3 hours. By 12 hours, the micropore volume reached a minimum of 0.01 cm^3/g. This steady reduction indicates structural densification and pore collapse commonly linked to graphitization. Notably, the consistency in micropore volume across three experimental replicates demonstrates the reproducibility of the graphitization process.

4.5. Electrical Conductivity

The electrical conductivity of graphitized carbon products is a crucial parameter for their use as electrode materials in energy storage devices.

Table 4.4: The electrical conductivity of graphitized carbons with Raney nickel alloy at 1500 °C over various dwell times.

Sample	**Conductivity (S/m) at 10 mA**
RNi AC, 1500 °C, 1 hr	1208 ± 0
RNi AC, 1500 °C, 3 hrs	959 ± 7
RNi AC, 1500 °C, 6 hrs	2472 ± 8
RNi AC, 1500 °C, 12 hrs	2314 ± 2
Activated carbon	Non-conductive
Commercial graphite (Sigma Aldrich)	7375 ± 0

Graphite has an anisotropic structure, characterized by high in-plane electrical conductivity due to delocalized π electrons within graphene layers, and significantly lower conductivity perpendicular to the layers, resulting from weak van der Waals interactions between them.[152] Activated carbon is non-conductive as measured by the process described in section 2.5.

The results of electrical conductivity measurements are summarized in Table 4.4. Notably, the sample subjected to 1 hour of graphitization showed an electrical conductivity of 1208 S/m. Although there was a general trend of increasing conductivity with longer graphitization times, deviations were observed in the 3-hour and 12-hour samples. Compared to the surface area analysis in the previous section, the 12-hour sample showed the lowest specific surface area, indicating a higher level of structural organization. The electrical conductivity characterization aligns with the XRD analysis, as the highest electrical conductivity was observed at 6 hours of graphitization, with a value of (2472 ± 8) S/m.

Understanding the sources of variability in electrical conductivity is essential. One contributing factor may be the presence of residual impurities in the structure, which can interfere with electron

transport. Variations in the concentration and distribution of these impurities may significantly affect the bulk electrical properties and conductivity. XPS analysis, as shown in Table 5.4, confirms the presence of residual aluminum and nickel, both at concentrations below 1 atomic%. A more detailed examination reveals the formation of nickel aluminate ($NiAl_2O_4$) during heat treatment. While forming an electrically insulating oxide layer can decrease overall conductivity, its impact may be negligible at impurity levels below 1 atomic%.

4.6. Benchmarking graphitic carbon against commercial electrode materials

The structural and surface analysis showed that both magnesium-treated graphitic carbon and Raney nickel alloy-based graphitic carbon exhibit turbostratic carbon characteristics. Comparing our materials with standard electrode materials that have similar traits would be beneficial. Vulcan XC-72 carbon black and commercial graphite stand out as promising electrode materials because of their structural and conductive properties. The stable, fluffy structure of carbon black allows electron tunnelling to be the primary contributor to its electrical conductivity.[154] Vulcan XC-72 has a surface area of 236-250 m^2/g,[155,156] an electrical conductivity of 277 S/m,[156] and a high I_D/I_G ratio of 1.43.[155] The previous sections showed that Sigma Aldrich commercial graphite has a minimal surface area of 7 m^2/g and a high electrical conductivity of 7374.6 S/m. The Raney nickel alloy treated graphitic carbon produced a surface area of 196.6 ± 10.5 m^2/g, comparable to Vulcan XC-72. However, the synthesized graphitic carbon showed better electrical conductivity at 2472.3 ± 8.4 m^2/g and improved crystallinity (I_D/I_G: 0.64 ± 0.53) compared to Vulcan XC-72. Its surface area is in the middle range, while its electrical conductivity reaches about one-third of that of commercial graphite. Magnesium-assisted graphitized carbon samples achieved a surface area of 47.3 ± 1.0 m^2/g, which is lower than that of Raney nickel alloy-assisted samples, primarily due to the longer 24-hour treatment. Interestingly, its electrical conductivity (3552.0 ± 78.5) S/m is approximately half that of commercial graphite. Overall, the characteristics of our graphitic carbon materials fall between those of amorphous Vulcan XC-72 and commercial graphite electrode materials, opening up new opportunities for electrode material development.

4.7. Summary

This chapter explored the performance of Raney nickel alloy as a catalyst for converting activated carbon into graphite. The study built on magnesium results by examining the ability of Raney nickel alloy to enhance the structural organization of carbon materials while improving their electrical properties during high-temperature processing.

Raney nickel alloy combined with activated carbon was thermally treated at temperatures ranging from 1400 °C to 1600 °C. The optimal temperature was 1500 °C, yielding the greatest structural improvements and development of graphitic content. Raman spectroscopy revealed a decrease in the I_D/I_G ratio and the emergence of a distinct 2D band, while XRD analysis confirmed the formation of layered carbon structures with graphite-like interlayer distances.

The graphitic structures formed were mainly turbostratic, characterized by disordered stacking of graphene layers along the c-axis. The turbostratic nature was evident through broad (002) peaks and irregular d-spacing measurements, indicating limited three-dimensional crystallinity despite the presence of partially ordered structures. The combination of Raman spectroscopy features and XRD diffraction patterns in some samples treated at 1500 °C for six hours showed initial signs of ordered graphitic structures, although turbostratic features remained predominant.

The graphitization process led to a gradual collapse of micropores, resulting in a decrease in BET surface area measurements over extended treatment durations. The electrical conductivity results aligned with the observations, as the 6-hour treated sample exhibited the highest conductivity of 2472 S/m and the most improved structural order. Some variability was observed, likely due to residual impurities and inconsistencies in the pelletization process. Overall, the trend confirmed that Raney nickel alloy-assisted graphitization significantly improves the electrical performance of carbon materials.

In summary, treating activated carbon at 1500°C with Raney nickel alloy resulted in the formation of turbostratic graphite structures. The process significantly improved structural order and electrical properties without achieving full graphitization, but it provided a valuable method for producing conductive carbon materials with moderate processing demands.

5. Metal removal in post-graphitization

5.1. Introduction

Building on earlier findings, metallic mediators such as magnesium and Raney nickel alloy significantly reduce the temperature and duration needed for synthetic graphitization compared to traditional thermal treatments. Conventional methods often need temperatures above 2500 °C and extended dwell times that can last several days or even weeks.[26,50] In contrast, extensive studies have shown that catalytic graphitization, usually carried out between 900 °C and 1600 °C, can be effectively achieved using transition metals, their salts, and oxides as catalysts. These materials help reorganize disordered carbon structures into graphitic domains by increasing atomic mobility and lowering the activation energy needed for the crystallization process.[3]

Despite their effectiveness, a major drawback of transition metal mediators is the difficulty in removing them after graphitization. Residual metallic contaminants are especially problematic in applications that require high-purity graphite, such as nuclear materials, battery anodes, or high-performance electronic devices.[3] In this context, magnesium offers a clear advantage: it can be removed relatively easily through acid leaching techniques after graphitization, making it a more appealing candidate for scalable and environmentally friendly production processes.[3,49]

We further examined the efficacy of Raney nickel alloy in the synthetic graphitization process. Raney nickel alloy consists of a 1:1 mass ratio of aluminum to nickel. To our knowledge, there is no existing literature on the use of Raney nickel alloy in graphitization. However, Raney nickel catalysts are often produced by leaching aluminum from the aluminum-nickel alloy using a strong base wash.[76] Based on this information, experiments with both acid and base treatments were conducted and discussed in this section regarding the removal of Raney nickel alloy in the post-graphitization process.

The effective removal of metals after graphitization is therefore crucial in achieving high-purity graphitic carbon. Various decontamination methods have been developed, most often involving acid leaching at room temperature or under heated or refluxing conditions to improve metal solubilization.[141,157] However, the effectiveness of these methods heavily depends on the chemical properties and structure of the metal species that are incorporated.

This section explains the post-graphitization metal removal strategies designed explicitly for magnesium and Raney nickel alloy.

5.2. Experimental

5.2.4. Magnesium extraction

To facilitate the removal of residual magnesium from the graphitized carbon matrix, an acid leaching protocol was employed with hydrochloric acid as the leaching agent. For that, 4 g of the synthesized magnesium-carbon composite was treated with 100 mL of 2M HCl under magnetic stirring. To improve the leaching efficiency, two experimental conditions were tested.

In the first approach, the mixture was maintained at room temperature (23 °C) while being stirred at 400 rpm for extended periods, up to 66 hours. This low-temperature, extended process allowed magnesium to dissolve gradually through proton-mediated surface reactions. In the second approach, the suspension was heated to 70 °C to accelerate the kinetics of the acid-metal reaction, and leaching was performed over different time intervals to evaluate the impact of thermal treatment on metal removal.

After acid treatment, the carbonaceous material was carefully washed with deionized (DI) water using a Büchner filtration setup. Washing continued until the pH of the filtrate remained stable between 6.5 and 7.0, confirming the removal of residual acid and soluble metal ions. The samples were then oven-dried at 120 °C overnight to produce dry powders for further characterization.

The efficiency of magnesium removal was first evaluated using X-ray Photoelectron Spectroscopy (XPS). X-ray Diffraction (XRD) was conducted to confirm the XPS results by detecting any crystalline magnesium-containing phases that might remain after treatment.

5.2.5. Raney nickel extraction

The removal protocol involved a two-step chemical treatment process, starting with acid leaching followed by alkaline digestion. The carbon-Raney nickel composite underwent the initial chemical stage, where it was treated with 3M hydrochloric acid (HCl) at 80 °C with continuous stirring at 400 rpm. Acid leaching served as the first step to break down nickel compounds dissolved in solution while also disrupting surface-bound metal structures through proton-mediated complexation reactions.

The base treatment was applied to acid-treated samples to remove aluminum-nickel residues, which had formed stable or passivated states. To optimize alkaline conditions, two different solutions of 20% sodium hydroxide (NaOH) and 20% potassium hydroxide (KOH) were used at 80 °C with matching stirring parameters. After each chemical washing step and upon completing the entire process, the samples were subjected to vacuum-assisted filtration with deionized (DI) water until the filtrate pH was stabilised between 6.5 and 7.0, indicating the effective removal of residual acids and bases. The dried carbon products were then dried overnight at 120 °C.

The efficiency assessment of Raney nickel alloy removal primarily relied on X-ray Photoelectron Spectroscopy (XPS). X-ray Diffraction (XRD) analysis supported XPS results and verified the remaining crystalline phases after the analysis.

5.3. Results

5.3.4. Magnesium extraction

The main reason for using magnesium as a metallic reactant in petcoke and activated carbon graphitization is its anticipated easy removal after the process. The authors Zhao et al. demonstrated that magnesium removal was facilitated after graphitization, particularly from structures featuring Voronoi tessellations and spheroidal shells composed of hexagonally arranged graphite platelets, as determined by XRD analysis.[3] Tsoufis T. successfully extracted magnesium oxide from synthesized carbon nanotubes (CNTs) through an acid treatment.[68] The research employed X-ray photoelectron spectroscopy (XPS) alongside X-ray diffraction (XRD) to evaluate magnesium extraction through acid washing. The elemental analysis of magnesium-assisted graphitized petcoke samples presents the percentages of carbon (C atomic%), oxygen (O atomic%), and magnesium (Mg atomic%) in Table 5.1. Moreover, Table 5.2 presents the elemental composition results for magnesium-assisted graphitized carbon samples and acid-treated samples.

Table 5.1: XPS results of **graphitized petcoke** samples after the magnesium removal treatments at various conditions.

Temperature (°C)	Time of acid wash (hrs)	Carbon Atomic%	Oxygen Atomic%	Magnesium Atomic%	Minor elements Atomic%
23	12	90.65	6.34	Non-detectable	S-1.1 Si- 0.86 N-0.43
		88.61	6.68	Non-detectable	S-1.08 Si- 1.55 N-1.32
		87.88	5.45	1.15	S-1.19 Si- 1.61 N-1.12
23	66	87.38	6.69	Non-detectable	S-1.14 Si- 2.41 N-1.53
		87.63	7.04	Non-detectable	S-0.88 Si- 2.47 N-1.06
		89.65	5.39	0.71	S-0.78 Si- 1.94 N-1.03
70	0.5	93.99	4.09	Non-detectable	S-1.01 Si 0.91
		92.10	4.11	Non-detectable	S-0.98 Si- 0.94 N-1.84
		88.94	7.81	0.43	S-1.08 Si- 1.55 N-1.32
70	1	90.16	5.90	Non-detectable	S-0.64 Si- 1.79 N-1.30
		92.37	4.80	Non-detectable	S-0.62 Si- 1.40 N-0.80
		91.32	5.25	Non-detectable	S-1.31 Si- 1.11 N-1.02

Table 5.2: XPS results of **graphitized activated carbon** samples after the magnesium removal treatments at various conditions.

Temperature (°C)	Time of acid wash (hrs)	Carbon Atomic %	Oxygen Atomic %	Magnesium Atomic%	Minor elements Atomic%
23	12	97.92	2.08	Non-detectable	Non-detectable
		96.22	2.71	Non-detectable	Si-1.07
		98.44	1.39	Non-detectable	Si- 0.17
23	66	97.67	1.88	Non-detectable	Si-0.45
		97.05	2.29	Non-detectable	Si-0.35 S- 0.32
		97.75	1.66	Non-detectable	Si-0.58
70	0.5	98.40	1.38	Non-detectable	Si-0.22
		98.63	1.37	Non-detectable	Non-detectable
		95.66	3.37	Non-detectable	Si-0.28 S – 0.68
70	1	96.96	1.98	Non-detectable	S-0.14 Si-0.38 N-0.53
		96.87	2.13	Non-detectable	S-0.25 Si-0.27 N-0.49
		98.28	1.44	Non-detectable	S-0.14 Si-0.13

The acid leaching tests were conducted under four different conditions varying in treatment duration and temperature to assess magnesium extraction efficiency. The data analysis required multiple independent sample sets because each condition needed three samples to verify both data reproducibility and robustness. The acid treatment process reduced magnesium content from 1.15 atomic% after 12 hours to 0.71 atomic% after 66 hours of acid leaching.

The combination of a higher temperature of 70 °C with a leaching period of 1 hour was chosen as the method for removing magnesium residues because it reduced processing time without losing effectiveness. XPS results indicated that this increased temperature completely removed all magnesium traces. The 70 °C, 1-hour acid treatment procedure was selected for subsequent experiments based on these results.

The graphitized petcoke samples contained sulfur ranging from 0.62 atomic% to 1.31 atomic% across all treatment conditions. This was attributed to sulfur contamination in the raw petcoke feedstock, as revealed by the XPS survey of unprocessed material (Figure 5.2). In contrast, the

XPS analysis of activated carbon (Figure 5.1) demonstrated that the sulfur content was minimal at 0.13 atomic%, which matched the results for the final graphitized activated carbon samples. The acid treatment proved successful in removing any remaining magnesium residues from the graphitized carbon materials based on these findings.

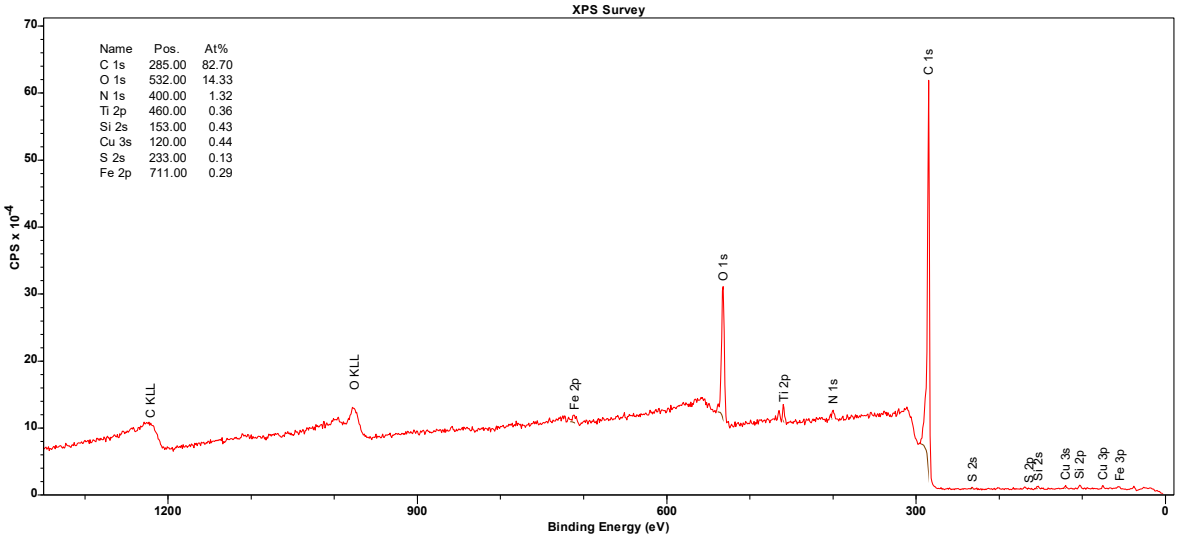

Figure 5.1 : XPS survey of activated carbon.

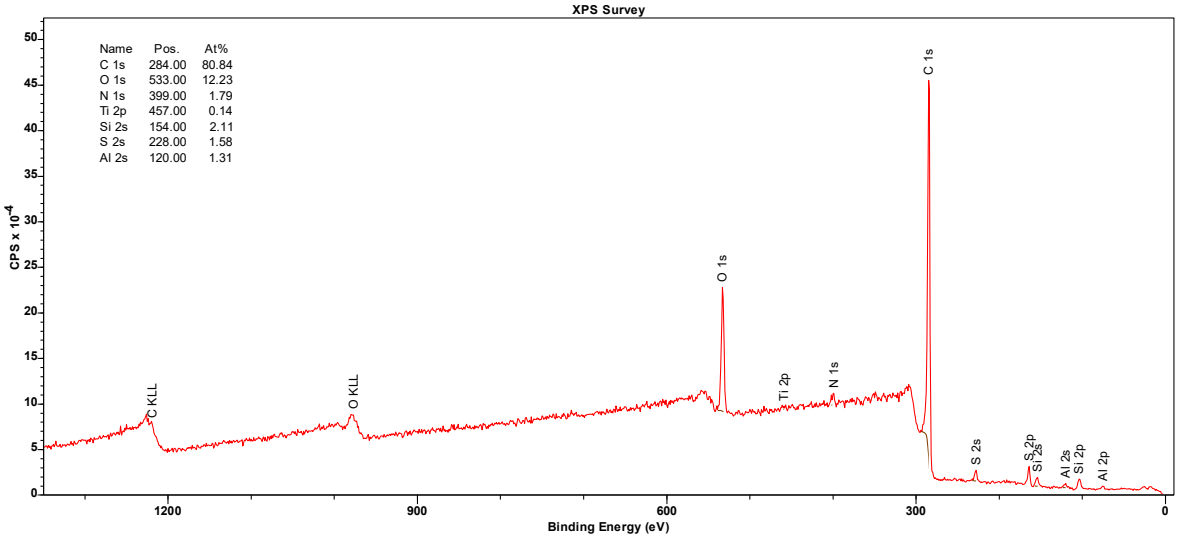

Figure 5.2: XPS survey of petcoke.

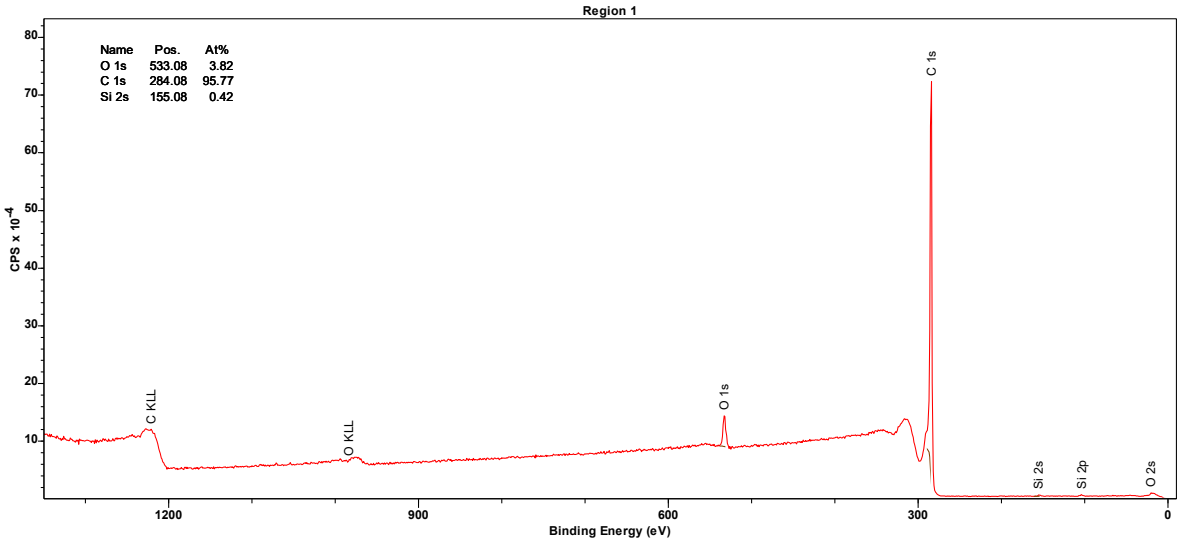

Figure 5.3: XPS survey of commercial graphite.

X-ray diffraction (XRD) patterns shown in Figure 5.4 illustrate the graphitized carbon samples after purification. The most intense peak at 26°-26.5° corresponds to the (002) reflection of graphitic structures, accompanied by observable (100), (101), and (004) planes at 42°, 44°, and 54°, respectively.

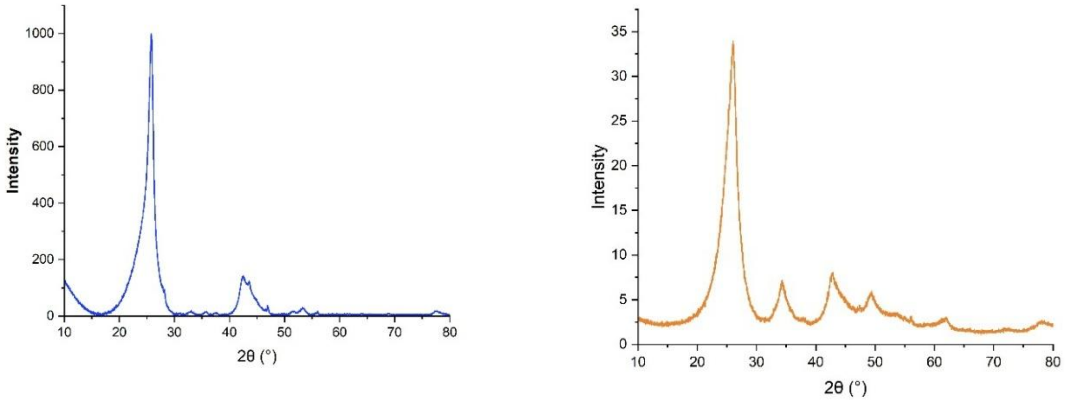

a b

Figure 5.4: XRD spectra of washed carbon samples at 70 °C for 1 hour with 2M HCl: a) graphitized activated carbon, b) graphitized petcoke.

The diffraction pattern of the acid-washed graphitized activated carbon sample in Figure 5.4a showed a well-ordered graphitic framework with minimal contaminants. However, the graphitized petcoke in Figure 5.4b revealed several diffraction peaks that remain visible after washing. The additional reflections observed in the spectra are caused by impurities, which include sulfur and silicon, since they are present in large amounts in the original petcoke material.

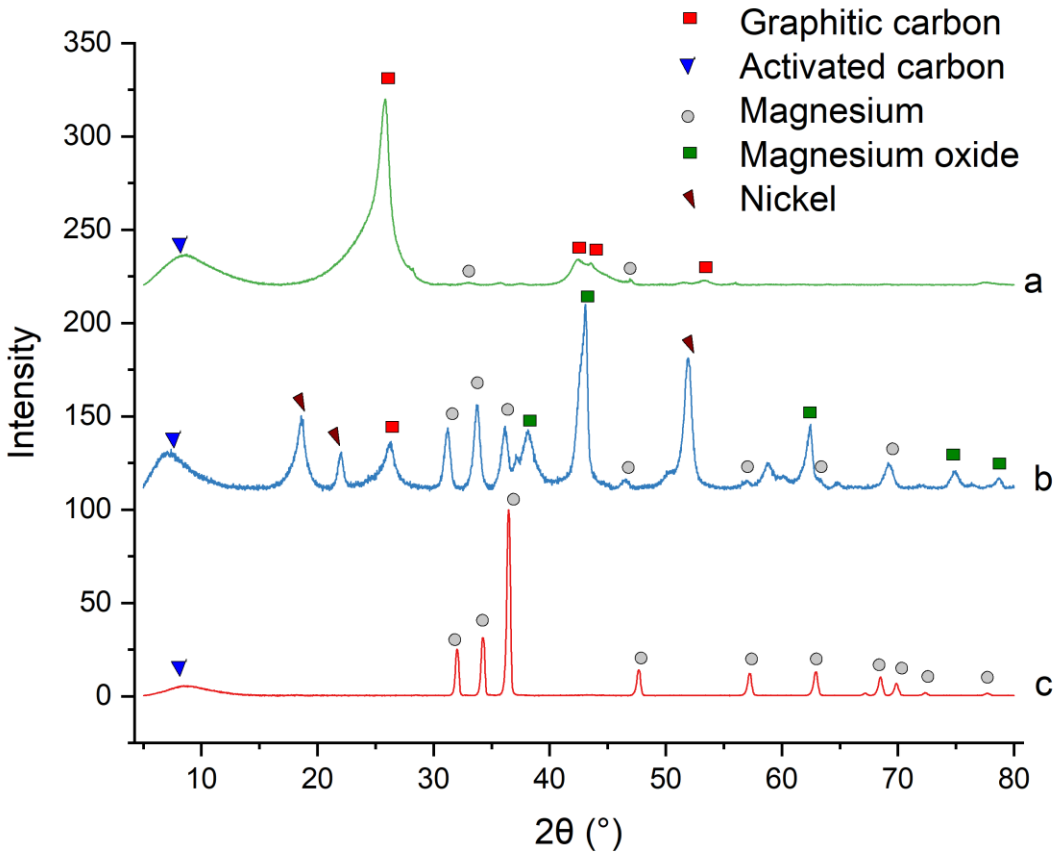

Figure 5.5: XRD spectra of magnesium-assisted graphitization at 1000 °C after a) the complete purification process b) just the graphitization process before washing, and c) magnesium and activated carbon composite before the graphitization process.

The efficacy of magnesium removal using 2 M HCl at 70 °C for 1 hour is shown in Figure 5.5. The mixture of magnesium and activated carbon in Figure 5.5c experienced significant changes when heated. Notably, the formation of magnesium oxide (MgO) during graphitization is evident in Figure 5.5b.[68] The presence of side oxidation reactions caused by oxygen impurities in the

precursor carbon material remains possible because magnesium exhibits high reactivity at elevated temperatures.[3]

The XRD analysis showed nickel diffraction signals in graphitized carbon products containing magnesium. These contaminants likely resulted from equipment cross-contamination, as the same crucibles were used for both the Raney nickel alloy and the magnesium-based graphitization. The nickel contaminants were removable through acid treatment, as demonstrated in Figure 5.5a.

The XRD analysis reveals that acid leaching effectively removes both magnesium and magnesium oxide from the carbon matrix, confirming the success of the purification method. The data indicated that treating at 70 °C for 1 hour with acid successfully eliminates magnesium-based phases while producing purified graphitic carbon through a simple post-treatment process.

5.3.5. Raney nickel alloy extraction

As outlined in the introduction, Raney nickel alloy is typically composed of aluminum and nickel in a 1:1 mass percent ratio. In its as-cast form, this alloy typically contains a heterogeneous mixture of intermetallic phases, including Al_3Ni, Al_3Ni_2, AlNi, as well as Al-Al_3Ni eutectic structures.[76] The melting point of the aluminum-nickel bimetallic system was experimentally determined to be approximately 1500 °C. According to the mechanism of carbon dissolution precipitate, the graphitization temperature must be higher than the melting point of the metal mediator to enable effective graphitic transformation.[18] Besides the melting and re-solidification of the metallic mediator during heat treatment, there is a risk of oxidation or other parasitic reactions. Particularly if residual impurities are present in the carbon precursor or if atmospheric contaminants occur during processing.

Considering the factors mentioned above, the washing process started with 3M HCl, following the procedure outlined in the section 5.2.5. Theoretically, aluminum-nickel alloy dissolves in HCl through the following possible chemical reactions.

Equation 5.1 : $Al_3Ni_{(s)}$ reaction in HCl

$$2Al_3Ni_{(S)} + 22HCl_{(aq)} \rightarrow 6AlCl_{3(aq)} + 2NiCl_{2(aq)} + 11H_{2(g)}$$

Equation 5.2: $Al_3Ni_{2(s)}$ reaction in HCl

$$2Al_3Ni_{2(S)} + 26HCl_{(aq)} \rightarrow 6AlCl_{3(aq)} + 4NiCl_{2(aq)} + 13H_{2(g)}$$

Equation 5.3 : $AlNi_{(s)}$ reaction in HCl

$$2AlNi_{(S)} + 10HCl_{(aq)} \rightarrow 2AlCl_{3(aq)} + 2NiCl_{2(aq)} + 5H_{2(g)}$$

Equation 5.4*:* $Al_{(s)}$+$Al_3Ni_{(s)}$ reaction in HCl

$$Al_{(s)} + Al_3Ni_{(S)} + 14HCl \rightarrow 4AlCl_{3(aq)} + NiCl_{2(aq)} + 7H_{2(g)}$$

These reactions are thermodynamically possible, where heating could increase reactivity.

Table 5.3: XPS analysis of washed carbon products only with 3M HCl at 80 °C.

Trial	Carbon Atomic%	Oxygen Atomic%	Nickel Atomic%	Aluminum Atomic%	Minor elements Atomic%
1	64.62	17.65	0.26	11.95	nitrogen 4.46, chlorine 0.35, silicon 0.72
2	60.04	19.87	0.36	13.10	nitrogen 5.58, chlorine 0.49, silicon 0.56
3	58.34	20.06	0.35	14.41	nitrogen 5.58, chlorine 0.48, silicon 0.77

Table 5.3 displays the percentages of residual elements in the acid-washed carbon products. A significant amount of aluminum (11-14 atomic%) and oxygen (17-20 atomic%) indicates the formation of aluminum oxide, which remains even after the acid wash. Aluminum oxide (Al_2O_3) has an amphoteric nature, reacting with both acids and bases.[158] Therefore, a subsequent base wash was performed using potassium hydroxide (KOH) and sodium hydroxide (NaOH) separately. The base treatment was conducted at 80 °C for 2 hours.

Table 5.4 presents the XPS analysis of carbon products after a hydrochloric acid wash followed by a base wash. Potassium hydroxide and sodium hydroxide were used to enhance the metal removal process. In each experimental trial, samples treated with potassium hydroxide (KOH) showed only trace amounts of residual aluminum and nickel, each less than 1 atomic%, which can be considered negligible. Additionally, the carbon content consistently exceeded 93 atomic%, closely approaching the typical purity level of carbon in commercial-grade graphite (~95 atomic%).

Table 5.4: XPS analysis of carbon products after a two-step washing process.

Type of base wash	Carbon Atomic%	Oxygen Atomic%	Nickel Atomic%	Aluminum Atomic%
20% KOH	93.79	5.30	0.12	0.79
	94.24	4.50	0.26	0.46
	94.28	4.75	0.30	0.50
20% NaOH	85.39	10.75	0.48	3.01
	86.77	9.77	0.47	2.87
	86.82	10.15	0.40	2.41

The presence of minor silicon impurities is due to the intrinsic composition of petcoke. In contrast, samples treated with 20% sodium hydroxide (NaOH) retained over 2 atomic% of aluminum and less than 0.3 atomic% nickel, indicating less effective leaching performance. Based on these comparative results, the 20% potassium hydroxide (KOH) solution was selected as the optimal reagent for the second stage of the Raney nickel alloy removal process.

This decision is further supported by the XRD profile of the final purified carbon product, shown in Figure 5.6a, which reveals the near-complete disappearance of characteristic diffraction peaks associated with the Raney nickel alloy following sequential treatment with HCl and KOH. The remaining low-intensity peaks are due to trace amounts of residual Al-Ni intermetallic phases, as previously discussed in this section.

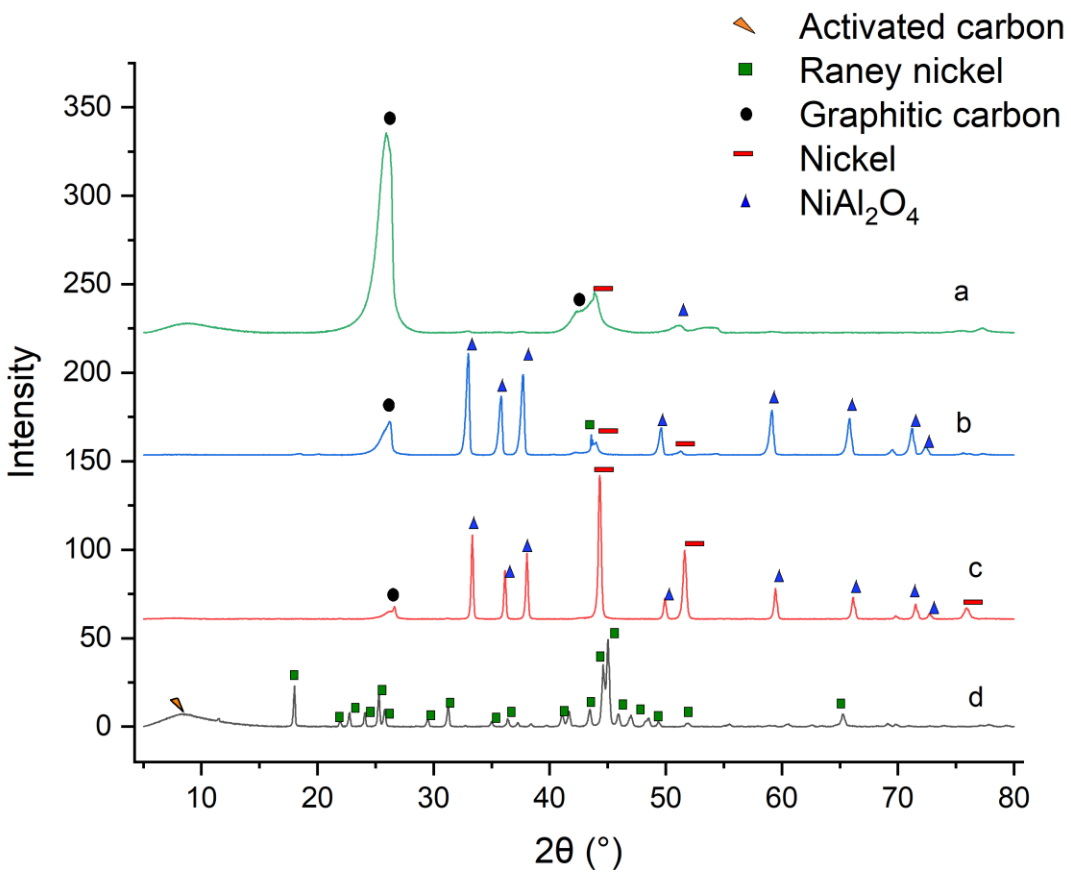

Figure 5.6: XRD spectra of Raney nickel-assisted graphitization at 1500 °C after a) the complete purification process, b) only the acid wash, c) just the graphitization process before washing, d) just mixing Raney nickel alloy and activated carbon before the graphitization process.

The XRD analysis shown in Figure 5.6b demonstrates that $NiAl_2O_4$ formed during the graphitization process. The spinel phase detected in the XRD patterns indicates that metallic species may have undergone oxidation, possibly due to the residual oxygen in the activated carbon precursor and during the heat treatment for metal removal. This aligns with the previously discussed magnesium removal process, where similar oxidative behaviour was noted.

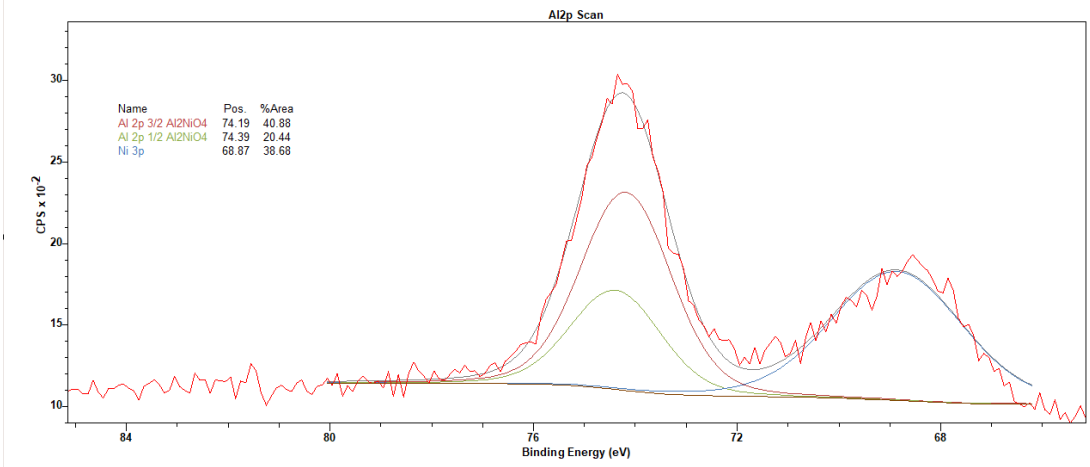

Figure 5.7: Aluminum scan from XPS analysis of residual aluminum species in Raney nickel-assisted graphitization.

Further confirmation was provided by XPS analysis in Figure 5.7, which showed that aluminum was chemically bonded with the $NiAl_2O_4$ phase.[159] Additionally, XRD signals for pure metallic nickel were clearly visible in the spectrum.[160] The XPS and XRD results together demonstrated that oxygen in the carbon matrix caused the formation of complex oxides at high temperatures, even when the experimental conditions appeared inert. The washing process with potassium hydroxide may also cause metal oxidation, in addition to the known effects of oxygen in the carbon matrix.

5.4. Summary

This chapter investigates the post-graphitization leaching behaviour of magnesium and Raney nickel alloy. The removal of metal mediators and surface contamination was primarily assessed with X-ray Photoelectron Spectroscopy (XPS). The X-ray Diffraction (XRD) measurements were used to verify the XPS results.

The results confirmed the complete removal of magnesium after a 2 M HCl acid wash at 70 °C for 1 hour. The thermal process caused partial oxidation of magnesium, and XRD analysis further confirmed the formation of MgO during the graphitization process. A two-step purification process removed most of the Raney nickel alloy. Treating with optimized conditions of 3 M HCl followed by 20% KOH at 80 °C for 2 hours resulted in negligible detection of nickel and aluminium, which were considered insignificant. As observed in magnesium-assisted graphitization, oxidation of the Al-Ni alloy during the process was detected.

6. Conclusion

6.1. Summary

This thesis focused on petroleum coke and activated carbon derived from petroleum coke, which underwent metal-assisted synthetic graphitization under moderate temperatures. Research on the graphitization process was conducted using magnesium and Raney nickel alloy based on a comprehensive literature review.

Chapter 1 offered an overall introduction to the thesis, including a literature review. Background information was provided on research while reviewing current studies focused on this specific area. The high-temperature synthetic graphitization process converted amorphous carbon into crystalline graphite. Metal-assisted graphitization techniques reduce the energy required and shorten the time needed for graphitization compared to the traditional graphitization process. The post-treatment process of magnesium has become easier, while the introduction of Raney nickel alloy introduces a new bimetallic system that may produce synergistic effects. This research evaluated microwave-assisted graphitization because of its rapid heating properties. The main precursor in this study is petroleum coke, a carbon-rich byproduct, with efforts focused on improving its graphitization and purity. The chapter laid a foundation for evaluating magnesium and Raney nickel alloy as metal mediators and their potential methods for post-graphitization removal. The research focus and main objectives of the thesis were presented at the end of Chapter 1.

Chapter 2 provided a detailed overview of research characterization methods used for graphitization analysis. The research employed X-ray diffraction (XRD) to determine crystallinity and interlayer spacing, utilizing Bragg's law and the Scherrer equation for calculating structural parameters. Raman spectroscopy was used to assess molecular vibrations and disorder levels by analyzing the D, G, and 2D peaks. SEM and TEM techniques offered surface morphology analysis by producing high-resolution images of surface features and internal structures. The four-point probe technique measured electrical conductivity while minimizing contact resistance. Surface area and pore features were analyzed using nitrogen adsorption isotherms, as determined by the Brunauer–Emmett–Teller (BET) technique. X-ray photoelectron spectroscopy (XPS) was used to examine the elemental composition and oxidation states of surface materials through quantitative

chemical measurements. These evaluation methods allowed researchers to gain a comprehensive understanding of the structural, chemical, and functional properties of graphitized carbon samples.

Chapter 3 evaluated magnesium's role as a monometallic catalyst in the graphitization of petroleum coke and activated carbon, with a focus on achieving efficient structural changes at moderate temperatures. The study investigated the impact of various factors, including temperature, dwell time, particle size, graphite seeding, and microwave-assisted heating, on the degree of graphitization. Raman and XRD analyses revealed that longer dwell times at 1000 °C significantly enhance graphitic ordering, particularly in medium-sized carbon particles. Microwave-assisted graphitization had limited success, with higher magnesium content providing slight improvements. Morphological studies using SEM and TEM confirmed the formation of layered structures, while BET analysis indicated a decrease in surface area and pore volume associated with increased graphitization. Electrical conductivity measurements supported these results, demonstrating that longer dwell times and greater structural order improve conductivity, although petroleum coke samples performed lower due to residual impurities. Overall, magnesium proved to be an effective catalyst for producing graphitic carbon with promising structural and functional properties.

Chapter 4 examined the use of Raney nickel alloy, a bimetallic system made of aluminum and nickel, in graphitizing activated carbon derived from petroleum coke. The study examined the impact of temperature and dwell time on the structural transformation of carbon, with a focus on 1500 °C as the optimal temperature for promoting graphitic growth and ordering. Raman and XRD analyses indicated that longer dwell times, especially 6 to 12 hours, improve crystallinity and decrease structural disorder, with signs of pristine graphite signals appearing after 6 hours of graphitization, despite the average analysis showing polycrystallinity. BET surface area and pore volume measurements demonstrated a consistent decline with increasing graphitization, indicating pore collapse and densification. Electrical conductivity increased with structural ordering, reaching 2472 S/m after 6 hours of graphitization; however, deviations arose due to residual impurities and inconsistencies in pelletization. Overall, Raney nickel alloy demonstrated strong potential as a bimetallic mediator for producing conductive, graphitized carbon at moderate temperatures.

Chapter 5 covered the post-graphitization purification of carbon materials made using magnesium and Raney nickel alloy as metal catalysts. While both metals effectively promoted graphitization

at moderate temperatures, removing them is essential for obtaining high-purity graphite. Magnesium was successfully extracted through a simple acid leaching process using 2 M HCl at 70 °C for one hour, as confirmed by XPS and XRD analyses. Raney nickel alloy required a more detailed two-step process: initial acid leaching followed by a 20% KOH wash, which effectively removed residual aluminum and nickel to nearly undetectable levels. The study also showed that metal species can oxidize during heat treatment due to residual oxygen in the carbon precursors, forming compounds such as MgO and $NiAl_2O_4$. These findings highlighted the necessity of specific purification methods to eliminate metal contaminants and produce structurally ordered, high-purity graphitic carbon.

6.2. Future work

1. Magnesium-assisted graphitization was evaluated considering temperature, dwell time, and particle size of the precursor. Additionally, microwave graphitization and seeding techniques were employed to further enhance the degree of graphitization. The latter techniques were performed with a dwell time of 24 hours, which was the maximum duration used in the process. Further experiments could be designed to optimize the dwell time, although such experiments might take months.

2. Both magnesium and Raney nickel alloy were combined with a carbon precursor at a consistent ratio of 1:1 (wt./wt.%) to limit the scope of the thesis. Investigating the metal-to-carbon ratio could further improve the graphitic properties of the produced materials.

3. The graphitization process could be further enhanced by applying heat treatment under high pressure, which promotes the rearrangement of organized carbon structures.[161]

4. Structural characterizations were primarily conducted using Raman spectroscopy and XRD analysis. However, some studies suggested that relying on conventional Bragg's law, Scherrer's equation, and empirical formulas might not be effective for analyzing turbostratic carbon. Therefore, implementing an advanced model for evaluating turbostratic carbon is advisable.

5. This thesis focuses on the material synthesis or graphitization of petroleum coke and activated carbon. Developing experiments to perform electrochemical analysis will help assess the effectiveness of the synthesized graphitic products for energy storage.

6.3. Contribution to Science

Conference Presentations

1. Exploring the synergistic effect of Raney nickel alloy on low-energy graphitization of petroleum coke, The World Conference on Carbon (Carbon 2025); France, **2025**

2. Magnesium-Assisted Synthetic Graphitization of Petroleum Coke: Mechanistic Insights, Carbon Structural Evolution, And Identification of Process Limitations. Canadian Chemistry Conference and Exhibition (CSC 2025); Canada, **2025**

3. Moderate Temperature Graphitization of Petroleum Coke with Magnesium. Canadian Chemistry Conference and Exhibition (CSC 2024); Canada, **2024**

7. References

1. Strong OKL, Nazari E, Roy T, Scotland K, Pede PR, Vreugdenhil AJ. Transforming micropores to mesopores by heat cycling KOH activated petcoke for improved kinetics of adsorption of naphthenic acids. *Heliyon*. 2023;9(2). doi:10.1016/j.heliyon.2023.e13500

2. Veluri PS, Katchala N, Anandan S, et al. Petroleum Coke as an Efficient Single Carbon Source for High-Energy and High-Power Lithium-Ion Capacitors. *Energy and Fuels*. 2021;35(10):9010-9016. doi:10.1021/acs.energyfuels.1c00665

3. Zhao L, Zhao X, Burke LT, Bennett JC, Dunlap RA, Obrovac MN. Voronoi-Tessellated Graphite Produced by Low-Temperature Catalytic Graphitization from Renewable Resources. *ChemSusChem*. 2017;10(17):3409-3418. doi:10.1002/cssc.201701211

4. Nugroho A, Nursanto EB, Pradanawati SA, Oktaviano HS, Nilasary H, Nursukatmo H. Fe based catalysts for petroleum coke graphitization for Lithium Ion battery application. *Mater Lett*. 2021;303. doi:10.1016/j.matlet.2021.130557

5. Yang F, Chen H, Guo J, Zheng P. Catalytic graphitization of anthracite-derived carbon as the anode for Li/K-ion batteries. *Journal of Materials Science: Materials in Electronics*. 2022;33(8):4862-4868. doi:10.1007/s10854-021-07675-8

6. Kim J, Son S, Choe M, Lee Z. In situ TEM investigation of nickel catalytic graphitization. *Mater Today Adv*. 2024;22. doi:10.1016/j.mtadv.2024.100494

7. Ji C, Liu Y, Xu J, Li Y, Shang Y, Su X. Enhanced microwave absorption properties of biomass-derived carbon decorated with transition metal alloy at improved graphitization degree. *J Alloys Compd*. 2022;890. doi:10.1016/j.jallcom.2021.161834

8. Osawa T, Kizawa T, Lee IYS, et al. Durability enhancement of chirally modified metallic nickel catalysts for enantioselective hydrogenation. *Catal Commun*. 2011;15(1):15-17. doi:10.1016/j.catcom.2011.08.006

9. conductivity of graphite.

10. März B, Jolley K, Marrow TJ, et al. Mesoscopic structure features in synthetic graphite. *Mater Des*. 2018;142:268-278. doi:10.1016/j.matdes.2018.01.038

11. Rattanaweeranon S, Limsuwan P, Thongpool V, Piriyawong V, Asanithi P. Influence of bulk graphite density on electrical conductivity. In: *Procedia Engineering*. Vol 32. Elsevier Ltd; 2012:1100-1106. doi:10.1016/j.proeng.2012.02.061

12. Zhao L, Bennett JC, Obrovac MN. Hexagonal platelet graphite and its application in Li-ion batteries. *Carbon N Y*. 2018;134:507-518. doi:10.1016/j.carbon.2018.03.017

13. Cançado LG, Takai K, Enoki T, et al. Measuring the degree of stacking order in graphite by Raman spectroscopy. *Carbon N Y*. 2008;46(2):272-275. doi:10.1016/j.carbon.2007.11.015

14. Shi Z. *Iron-Catalyzed Graphitization of Biochar to Produce Graphitic Carbon Materials*.

15. Zhang L, Zhao XS. Carbon-based materials as supercapacitor electrodes. *Chem Soc Rev*. 2009;38(9):2520-2531. doi:10.1039/b813846j

16. Li J, Zhang Z, Wang Z, Cao Q, Guo F, Cao Q. Low temperature graphitization and electrochemical properties of porous carbon catalyzed with bimetal Ni-Mo. *Diam Relat Mater*. 2022;123. doi:10.1016/j.diamond.2022.108862

17. Shi Z. *Iron-Catalyzed Graphitization of Biochar to Produce Graphitic Carbon Materials*.

18. Hunter RD, Takeguchi M, Hashimoto A, et al. Elucidating the Mechanism of Iron-Catalyzed Graphitization: The First Observation of Homogeneous Solid-State Catalysis. *Advanced Materials*. Published online 2024. doi:10.1002/adma.202404170

19. Thompson E, Danks AE, Bourgeois L, Schnepp Z. Iron-catalyzed graphitization of biomass. *Green Chemistry*. 2015;17(1):551-556. doi:10.1039/c4gc01673d

20. Magnesium citrate induced growth of noodle-like porous graphitic.

21. Ratynski M, Hamankiewicz B, Krajewski M, Boczar M, Ziolkowska D, Czerwinski A. Impact of natural and synthetic graphite milling energy on lithium-ion electrode capacity and cycle life. *Carbon N Y*. 2019;145:82-89. doi:10.1016/j.carbon.2019.01.019

22. Zhang J, Liang C, Dunn JB. Graphite Flows in the U.S.: Insights into a Key Ingredient of Energy Transition. *Environ Sci Technol*. 2023;57(8):3402-3414. doi:10.1021/acs.est.2c08655

23. Ouzilleau P, Gheribi AE, Chartrand P, Soucy G, Monthioux M. Why some carbons may or may not graphitize? The point of view of thermodynamics. *Carbon N Y*. 2019;149:419-435. doi:10.1016/j.carbon.2019.04.018

24. Nugroho A, Nursanto EB, Pradanawati SA, Oktaviano HS, Nilasary H, Nursukatmo H. Fe based catalysts for petroleum coke graphitization for Lithium Ion battery application. *Mater Lett*. 2021;303. doi:10.1016/j.matlet.2021.130557

25. Yang F, Chen H, Guo J, Zheng P. Catalytic graphitization of anthracite-derived carbon as the anode for Li/K-ion batteries. *Journal of Materials Science: Materials in Electronics*. 2022;33(8):4862-4868. doi:10.1007/s10854-021-07675-8

26. Nuriskasari I, Zulfia Syahrial A, Wahyuadi J, Soedarsono M. Catalytic Graphitization of Biomass as a Potential Method Produce Graphite In The Future : A Review. 2023;01(02). doi:10.59511/riestech.v1i0

27. Zhao L. *CATALYTIC GRAPHITIZATION BY LIGHT METALS*.; 2019.

28. Oya A, Marsh H. *Review Phenomena of Catalytic Graphitization*. Vol 17.; 1982.

29. Asao~ya S, ~tani. *CATALYTIC GRAPHITIZATION OF CARBONS BY VARIOUS METALS*. Vol 17.

30. Gomez-Martin A, Schnepp Z, Ramirez-Rico J. Structural Evolution in Iron-Catalyzed Graphitization of Hard Carbons. *Chemistry of Materials*. 2021;33(9):3087-3097. doi:10.1021/acs.chemmater.0c04385

31. Hunter RD, Ramírez-Rico J, Schnepp Z. Iron-catalyzed graphitization for the synthesis of nanostructured graphitic carbons. *J Mater Chem A Mater.Royal Society of Chemistry*. 2022;10(9):4489-4516. doi:10.1039/d1ta09654k

32. Li H, Zhang H, Li K, Zhang J, Sun M, Su B. Catalytic graphitization of coke carbon by iron: Understanding the evolution of carbon Structure, morphology and lattice fringes. *Fuel*. 2020;279. doi:10.1016/j.fuel.2020.118531

33. Elucidating the Mechanism of Iron-Catalyzed Graphitization The First Observation of.

34. adma202404170-sup-0001-suppmat Elucidating the Mechanism of Iron-Catalyzed Graphitization The First Observation of.

35. adma202404170-sup-0004-videos3 Elucidating the Mechanism of Iron-Catalyzed Graphitization The First Observation of.

36. Zhang L, Liu C, Song R, Wang Q, Chen Y, Huang P. Low-temperature graphitization of carbon foam using nickel-based catalysts for enhanced thermal conductivity: application in the pyrolysis of oil-rich coal. *Journal of Porous Materials*. 2024;31(3):1087-1099. doi:10.1007/s10934-024-01562-3

37. nickel alloy graphitization.

38. Catalytic effect of nickel under carbonization of polyimide films.

39. Narkiewicz U, Podsiadły M, Jędrzejewski R, Pełech I. Catalytic decomposition of hydrocarbons on cobalt, nickel and iron catalysts to obtain carbon nanomaterials. *Appl Catal A Gen*. 2010;384(1-2):27-35. doi:10.1016/j.apcata.2010.05.050

40. Krivoruchko OP, Maksimova NI, Zaikovskii VI, Salanov AN. Study of multiwalled graphite nanotubes and filaments formation from carbonized products of polyvinyl alcohol via catalytic graphitization at 600-8008C in nitrogen atmosphere. *Carbon N Y*. 2000;38.

41. Zhao L. *CATALYTIC GRAPHITIZATION BY LIGHT METALS*.; 2019.

42. Murty HN, Biederman DL, Heintz$ EA. *CATALYTIC GRAPHITIZATION OF MODEL COMPOUND CHARS BY ALUMINUM AND BERYLLIUM*.

43. Jones LE, Thrower PA. *INFLUENCE OF BORON ON CARBON FIBER MICROSTRUCTURE, PHYSICAL PROPERTIES, AND OXIDATION BEHAVIOR*. Vol 29.; 1991.

44. Xu L, Wu J, Bai S. Fabrication and microstructure of boron-doped isotropic pyrolytic carbon. *Carbon N Y*. 2012;50(12):4705-4710. doi:10.1016/j.carbon.2012.05.062

45. Wen Y, Lu Y, Xiao H, Qin X. Further investigation on boric acid catalytic graphitization of polyacrylonitrile carbon fibers: Mechanism and mechanical properties. *Mater Des*. 2012;36:728-734. doi:10.1016/j.matdes.2011.11.051

46. Xu Z, Cai D, Hu Z, Wang F, Gan L. The structural optimization and high electrochemical behavior of porous carbons by graphitization in molten sodium metals. *Electrochim Acta*. 2014;117:486-491. doi:10.1016/j.electacta.2013.11.153

47. Xu Z, Xia B, Wang W, Ji T, Ma C, Gan L. Graphitization of aerogel-like carbons in molten sodium metal. *Carbon N Y.Elsevier Ltd*. 2011;49(10):3385-3387. doi:10.1016/j.carbon.2011.04.004

48. Schneider JJ, Maksimova NI, Engstler J, Joshi R, Schierholz R, Feile R. Catalyst free growth of a carbon nanotube-alumina composite structure. *Inorganica Chim Acta*. 2008;361(6):1770-1778. doi:10.1016/j.ica.2006.10.025

49. Okamoto T, Huang X, Kagawa A. Graphite nodularization and graphitization of magnesium treated cast irons solidified under argon atmosphere pressure up to 145 atm. *Metal Science*. 1984;18(4):169-176. doi:10.1179/030634584790420168

50. Viala JC, Fortier P, Claveyrolas G, Vincent H, Bouix J. *Effect of Magnesium on the Composition, Microstructure and Mechanical Properties of Carbon Fibres*. Vol 26.; 1991.

51. Yuan Y, Wang T, Chen H, et al. Ambient Temperature Graphitization Based on Mechanochemical Synthesis. *Angewandte Chemie - International Edition*. 2020;59(49):21935-21939. doi:10.1002/anie.202009180

52. Nishimiya K, Hata T, Kikuchi H, Imamura Y. Effect of aluminum compound addition on graphitization of wood charcoal by direct electric pulse heating method. *Journal of Wood Science*. 2004;50(2):177-181. doi:10.1007/s10086-003-0532-z

53. Lin QY, Feng Z, Liu ZJ, et al. Atomic scale investigations of catalyst and catalytic graphitization in a silicon and titanium doped graphite. *Carbon N Y*. 2015;88:252-261. doi:10.1016/j.carbon.2015.03.001

54. Qiu H, Han L, Liu L. Properties and microstructure of graphitised ZrC/C or SiC/C composites. *Carbon N Y*. 2005;43(5):1021-1025. doi:10.1016/j.carbon.2004.11.043

55. Niu Y, Zhang X, Wu J, Zhao J, Yan X, Li Y. Catalytic and enhanced effects of silicon carbide nanoparticles on carbonization and graphitization of polyimide films. *RSC Adv*. 2014;4(80):42569-42576. doi:10.1039/c4ra04371e

56. Imamura R, Matsui K, Takeda S, Ozaki J, Oya A. *A New Role for Phosphorus in Graphitization of Phenolic Resin*. Vol 37.; 1999.

57. Sugimoto~ Y, Derbyshke FJ, Scaroni AW. *THE EFFECT OF SULFUR EVOLUTION ON THE PROPERTIES OF HIGH-TEMPERATURE CARBONS-I. THIANTHRENE AND THIANTHRENE-ANTHRACENE PRECURSORS*. Vol 23.

58. Yang G, Han H, Li T, Du C. Synthesis of nitrogen-doped porous graphitic carbons using nano-CaCO 3 as template, graphitization catalyst, and activating agent. *Carbon N Y*. 2012;50(10):3753-3765. doi:10.1016/j.carbon.2012.03.050

59. Peng J, Chen N, He R, Wang Z, Dai S, Jin X. Electrochemically Driven Transformation of Amorphous Carbons to Crystalline Graphite Nanoflakes: A Facile and Mild Graphitization Method. *Angewandte Chemie - International Edition*. 2017;56(7):1751-1755. doi:10.1002/anie.201609565

60. Jin X, He R, Dai S. Electrochemical Graphitization: An Efficient Conversion of Amorphous Carbons to Nanostructured Graphites. *Chemistry - A European Journal*. 2017;23(48):11455-11459. doi:10.1002/chem.201701620

61. Hu X Bin, Cheng G, Zhao BY, Wang HM, Hu KA. Catalytic effect of dopants on microstructure and performance of MCMB-derived carbon laminations. *Carbon N Y*. 2004;42(2):381-386. doi:10.1016/j.carbon.2003.11.010

62. Tang J, Wang T, Sun X, et al. Effect of transition metal on catalytic graphitization of ordered mesoporous carbon and Pt/metal oxide synergistic electrocatalytic performance. *Microporous and Mesoporous Materials*. 2013;177:105-112. doi:10.1016/j.micromeso.2013.04.027

63. Sinclair R, Itoh T, Chin R. In situ TEM studies of metal-carbon reactions. In: *Microscopy and Microanalysis*. Vol 8. Cambridge University Press; 2002:288-304. doi:10.1017/s1431927602020226

64. Yan Z, Zhang M, Xie J, Shen PK. Vanadium carbide and graphite promoted Pd electrocatalyst for ethanol oxidation in alkaline media. *J Power Sources*. 2013;243:336-342. doi:10.1016/j.jpowsour.2013.06.063

65. Tang K, Li Y, Cao H, et al. Integrated electrospun carbon nanofibers with vanadium and single-walled carbon nanotubes through covalent bonds for high-performance supercapacitors. *RSC Adv*. 2015;5(50):40163-40172. doi:10.1039/c5ra02237a

66. Sevilla M, Fuertes AB. Catalytic graphitization of templated mesoporous carbons. *Carbon N Y*. 2006;44(3):468-474. doi:10.1016/j.carbon.2005.08.019

67. Shi Z, Jin Y, Han T, et al. Bio-based anode material production for lithium–ion batteries through catalytic graphitization of biochar: the deployment of hybrid catalysts. *Sci Rep*. 2024;14(1). doi:10.1038/s41598-024-54509-8

68. Xia S, Cai N, Lu W, et al. Reaction kinetics, mechanism, and product analysis of the iron catalytic graphitization of cellulose. *J Clean Prod*. 2021;329. doi:10.1016/j.jclepro.2021.129735

69. Tsoufis T, Xidas P, Jankovic L, et al. Catalytic production of carbon nanotubes over Fe-Ni bimetallic catalysts supported on MgO. *Diam Relat Mater*. 2007;16(1):155-160. doi:10.1016/j.diamond.2006.04.014

70. Yao D, Wang CH. Pyrolysis and in-line catalytic decomposition of polypropylene to carbon nanomaterials and hydrogen over Fe- and Ni-based catalysts. *Appl Energy*. 2020;265. doi:10.1016/j.apenergy.2020.114819

71. Marshall CP, Wilson MA. Ball milling and annealing graphite in the presence of cobalt. *Carbon N Y*. 2004;42(11):2179-2186. doi:10.1016/j.carbon.2004.04.028

72. Iwazaki T, Semba T, Konishi S, et al. Catalytic excavation and graphitization of activated carbon by cobalt nanoparticles. *Chem Lett*. 2008;37(12):1194-1195. doi:10.1246/cl.2008.1194

73. Inagaki M, Fujita K, Takeuchi Y, Oshida K, Iwata H, Konno H. *Formation of Graphite Crystals at 1000-12008C from Mixtures of Vinyl Polymers with Metal Oxides*. Vol 39.; 2001.

74. Kim J, Lee J, Choi Y, Jo C. Synthesis of hierarchical linearly assembled graphitic carbon nanoparticles via catalytic graphitization in SBA-15. *Carbon N Y*. 2014;75:95-103. doi:10.1016/j.carbon.2014.03.039

75. Wen Y, Chi L, Wen X, Chen X, Mijowska E. Nitrogen/Oxygen Enriched Hierarchical Porous Carbons Derived from Waste Peanut Shells Boosting Performance of Supercapacitors. *Adv Electron Mater*. 2020;6(10). doi:10.1002/aelm.202000450

76. Yang F, Zhao H, Li R, et al. *Growth Modes of Single-Walled Carbon Nanotubes on Catalysts*. Vol 8.; 2022. https://www.science.org

77. Zeifert B, Blásquez JS, Moreno JGC, et al. *RANEY-NICKEL CATALYSTS PRODUCED BY MECHANICAL ALLOYING*. Vol 18.; 2008.

78. Catalytic effect of nickel under carbonization of polyimide films.

79. Khosh MS, Xu X, Trumbore SE. Small-mass graphite preparation by sealed tube zinc reduction method for AMS 14C measurements. *Nucl Instrum Methods Phys Res B*. 2010;268(7-8):927-930. doi:10.1016/j.nimb.2009.10.066

80. Tang J, Salunkhe RR, Zhang H, et al. Bimetallic metal-organic frameworks for controlled catalytic graphitization of nanoporous carbons. *Sci Rep*. 2016;6. doi:10.1038/srep30295

81. Schneider JJ, Maksimova NI, Engstler J, Joshi R, Schierholz R, Feile R. Catalyst free growth of a carbon nanotube-alumina composite structure. *Inorganica Chim Acta*. 2008;361(6):1770-1778. doi:10.1016/j.ica.2006.10.025

82. Zhang B, Song H, Chen X, Yang W, Li Z, Ma Z. Transformation of Lewis acid during the carbonization and graphitization of mesophase pitches. *J Anal Appl Pyrolysis*. 2013;104:433-440. doi:10.1016/j.jaap.2013.06.001

83. Li WQ, Zhang HB, Xiong X, Xiao F. Effect of zirconium addition on the microstructure and performance of carbon foam. *Materials Science and Engineering: A*. 2010;527(12):2993-2997. doi:10.1016/j.msea.2010.01.041

84. Chen Z, Wu W, Chen Z, Cong X, Qiu J. Microstructural characterization on ZrC doped carbon/carbon composites. *Ceram Int*. 2012;38(1):761-767. doi:10.1016/j.ceramint.2011.08.002

85. Liu M, Wang T, Zhang X, et al. A facile synthesis of highly compacted, molybdenum-embedded, ordered, mesoporous, protective carbon films of graphitic structure. *Corros Sci*. 2014;87:297-305. doi:10.1016/j.corsci.2014.06.039

86. Li G, Tan S, Song R, Tang T. Synergetic Effects of Molybdenum and Magnesium in Ni-Mo-Mg Catalysts on the One-Step Carbonization of Polystyrene into Carbon Nanotubes. *Ind Eng Chem Res*. 2017;56(41):11734-11744. doi:10.1021/acs.iecr.7b02697

87. Xue G, Dong J, Zhang J. *SERS Studies of Polymers on Metal Surfaces. 4. Cyclization and Graphitization of Polyacrylonitrile on Rough Silver Surfaces*. Vol 25.; 1992. https://pubs.acs.org/sharingguidelines

88. Wang R, Lu G, Zhuang H, Yu J. Synergistic catalytic effect of light rare earth element and other additives on the degree of graphitization and properties of graphite. *J Mater Sci*. 2017;52(2):663-673. doi:10.1007/s10853-016-0359-9

89. Zhang C, Lu G, Sun Z, Yu J. Catalytic graphitization of carbon/carbon composites by lanthanum oxide. *Journal of Rare Earths*. 2012;30(2):128-132. doi:10.1016/S1002-0721(12)60008-8

90. YI S, CHEN J, XIAO X, LIU L, FAN Z. Effect of praseodymium on catalytic graphitization of furan resin carbon. *Journal of Rare Earths*. 2010;28(1):69-71. doi:10.1016/S1002-0721(09)60053-3

91. Wang R, Lu G, Qiao W, Sun Z, Zhuang H, Yu J. Catalytic effect of praseodymium oxide additive on the microstructure and electrical property of graphite anode. *Carbon N Y*. 2015;95:940-948. doi:10.1016/j.carbon.2015.09.013

92. Shi Z, Jin Y, Han T, et al. Bio-based anode material production for lithium–ion batteries through catalytic graphitization of biochar: the deployment of hybrid catalysts. *Sci Rep*. 2024;14(1). doi:10.1038/s41598-024-54509-8

93. Bacsa RR, Cameán I, Ramos A, et al. Few layer graphene synthesis on transition metal ferrite catalysts. *Carbon N Y*. 2015;89:350-360. doi:10.1016/j.carbon.2015.03.054

94. Nuriskasari I, Zulfia Syahrial A, Wahyuadi J, Soedarsono M. Catalytic Graphitization of Biomass as a Potential Method Produce Graphite In The Future : A Review. 2023;01(02). doi:10.59511/riestech.v1i0

95. Schneider JJ, Maksimova NI, Engstler J, Joshi R, Schierholz R, Feile R. Catalyst free growth of a carbon nanotube-alumina composite structure. *Inorganica Chim Acta*. 2008;361(6):1770-1778. doi:10.1016/j.ica.2006.10.025

96. Kim T, Lee J, Lee KH. Full graphitization of amorphous carbon by microwave heating. *RSC Adv*. 2016;6(29):24667-24674. doi:10.1039/c6ra01989g

97. Głowniak S, Szczęśniak B, Choma J, Jaroniec M. Advances in Microwave Synthesis of Nanoporous Materials. *Advanced Materials.John Wiley and Sons Inc*. 2021;33(48). doi:10.1002/adma.202103477

98. Islam MS, Kushwaha AK, Misra M. Review on the recycling of anode graphite from waste lithium-ion batteries. *J Mater Cycles Waste Manag.Springer*. 2024;26(6):3341-3369. doi:10.1007/s10163-024-02093-4

99. Ji C, Liu Y, Xu J, Li Y, Shang Y, Su X. Enhanced microwave absorption properties of biomass-derived carbon decorated with transition metal alloy at improved graphitization degree. *J Alloys Compd*. 2022;890. doi:10.1016/j.jallcom.2021.161834

100. Pawelski D, Plonska-Brzezinska ME. Microwave-Assisted Synthesis as a Promising Tool for the Preparation of Materials Containing Defective Carbon Nanostructures: Implications on Properties and Applications. *Materials.Multidisciplinary Digital Publishing Institute (MDPI)*. 2023;16(19). doi:10.3390/ma16196549

101. Khoshk Rish S, Tahmasebi A, Wang R, Dou J, Yu J. Formation mechanism of nano graphitic structures during microwave catalytic graphitization of activated carbon. *Diam Relat Mater*. 2021;120. doi:10.1016/j.diamond.2021.108699

102. Baghel P, Sakhiya AK, Kaushal P. Ultrafast growth of carbon nanotubes using microwave irradiation: characterization and its potential applications. *Heliyon.Elsevier Ltd*. 2022;8(10). doi:10.1016/j.heliyon.2022.e10943

103. Liu T, Xie X, Pang Y, Kobayashi S. Co/C nanoparticles with low graphitization degree: A high performance microwave-absorbing material. *J Mater Chem C Mater*. 2016;4(8):1727-1735. doi:10.1039/c5tc03874j

104. Głowniak S, Szczęśniak B, Choma J, Jaroniec M. Advances in Microwave Synthesis of Nanoporous Materials. *Advanced Materials.John Wiley and Sons Inc*. 2021;33(48). doi:10.1002/adma.202103477

105. I. MJ, Vanitha M, Camellia P, Balasubramanian N. Augmentation of graphite purity from mineral resources and enhancing % graphitization using microwave irradiation: XRD and Raman studies. *Diam Relat Mater*. 2018;88:129-136. doi:10.1016/j.diamond.2018.07.009

106. Liu D, Zhao X, Su R, et al. Highly porous graphitic activated carbons from lignite via microwave pretreatment and iron-catalyzed graphitization at low-temperature for supercapacitor electrode materials. *Processes*. 2019;7(5). doi:10.3390/pr7050300

107. Kuang D, Tian Y, Duan W, Tian Z, Sun X, Wang S. Effects of degree of graphitization of C shells on microwave absorption of Fe-C core-shell nanoparticles with excellent comparability. *J Mater Sci Technol*. 2024;179:1-8. doi:10.1016/j.jmst.2023.09.020

108. Kim T, Jo C, Lim WG, Lee J, Lee J, Lee KH. Facile conversion of activated carbon to battery anode material using microwave graphitization. *Carbon N Y*. 2016;104:106-111. doi:10.1016/j.carbon.2016.03.021

109. Kap *, Yang S, Yoon YJ, Lee S, Lee WJ, Kim JH. *Further Carbonization of Anisotropic and Isotropic Pitch-Based Carbons by Microwave Irradiation*. Vol 40.; 2002.

110. Zeifert B, Blásquez JS, Moreno JGC, et al. *RANEY-NICKEL CATALYSTS PRODUCED BY MECHANICAL ALLOYING*. Vol 18.; 2008.

111. A Pavlic BA, Adkins H. *Preparation of a Raney Nickel Catalyst*. Vol 54. UTC; 1946. https://pubs.acs.org/sharingguidelines

112. Rayhan U, Kowser Z, Islam MN, Redshaw C, Yamato T. A Review on the Recent Advances in the Reductions of Carbon–Carbon/Oxygen Multiple Bonds Including Aromatic Rings Using Raney Ni–Al Alloy or Al Powder in the Presence of Noble Metal Catalysts in Water. *Top Catal*. 2018;61(7-8):560-574. doi:10.1007/s11244-018-0994-2

113. Zhou Z, Bouwman WG, Schut H, Pappas C. Interpretation of X-ray diffraction patterns of (nuclear) graphite. *Carbon N Y*. 2014;69:17-24. doi:10.1016/j.carbon.2013.11.032

114. Thomas NW. A Fourier transform method for powder diffraction based on the Debye scattering equation. *Acta Crystallogr A*. 2011;67(6):491-506. doi:10.1107/S0108767311029825

115. Zheng G, Xu P, Sridharan K, Allen T. Characterization of structural defects in nuclear graphite IG-110 and NBG-18. *Journal of Nuclear Materials*. 2014;446(1-3):193-199. doi:10.1016/j.jnucmat.2013.12.013

116. Jain R. A Review on the Development of XRD in Ferrite Nanoparticles. *J Supercond Nov Magn.Springer*. 2022;35(5):1033-1047. doi:10.1007/s10948-022-06213-9

117. Harrington GF, Santiso J. Back-to-Basics tutorial: X-ray diffraction of thin films. *J Electroceram*. 2021;47(4):141-163. doi:10.1007/s10832-021-00263-6

118. Wu H, Gakhar R, Chen A, Marshall CP, Scarlat R. *Comparative Analysis of Microstructure and Reactive Sites for Nuclear Graphite IG-110 and Graphite Matrix A3*.; 2019. http://www.inl.gov

119. Ali A, Chiang YW, Santos RM. X-Ray Diffraction Techniques for Mineral Characterization: A Review for Engineers of the Fundamentals, Applications, and Research Directions. *Minerals*. 2022;12(2). doi:10.3390/min12020205

120. Schuepfer DB, Badaczewski F, Guerra-Castro JM, et al. Assessing the structural properties of graphitic and non-graphitic carbons by Raman spectroscopy. *Carbon N Y*. Published online 2020:359-372.

121. measuring-disorder-in-graphene-with-raman-spectroscopy-275cdubkah.

122. Eckmann A, Felten A, Mishchenko A, et al. Probing the nature of defects in graphene by Raman spectroscopy. *Nano Lett*. 2012;12(8):3925-3930. doi:10.1021/nl300901a

123. Pimenta MA, Dresselhaus G, Dresselhaus MS, Cançado LG, Jorio A, Saito R. Studying disorder in graphite-based systems by Raman spectroscopy. *Physical Chemistry Chemical Physics*. 2007;9(11):1276-1291. doi:10.1039/b613962k

124. Pimenta MA, Dresselhaus G, Dresselhaus MS, Cançado LG, Jorio A, Saito R. Studying disorder in graphite-based systems by Raman spectroscopy. *Physical Chemistry Chemical Physics*. 2007;9(11):1276-1291. doi:10.1039/b613962k

125. Papanai GS, Sharma I, Gupta BK. Probing number of layers and quality assessment of mechanically exfoliated graphene via Raman fingerprint. *Mater Today Commun*. 2020;22. doi:10.1016/j.mtcomm.2019.100795

126. Beyssac O, Lazzeri M. Application of raman spectroscopy to the study of graphitic carbons in the earth sciences. *European Mineralogical Union Notes in Mineralogy*. 2012;12(1):415-454. doi:10.1180/EMU-notes.12.12

127. Mohammed A, Abdullah A. *SCANNING ELECTRON MICROSCOPY (SEM): A REVIEW*.

128. Lam M, Schwarz C, Sharma R, Donnelly J. An Introduction to Scanning Electron Microscopy and Science Communication Skills for Undergraduate Chemistry Students. *J Chem Educ*. 2023;100(7):2802-2808. doi:10.1021/acs.jchemed.3c00076

129. Raval N, Maheshwari R, Kalyane D, Youngren-Ortiz SR, Chougule MB, Tekade RK. Importance of physicochemical characterization of nanoparticles in pharmaceutical product development. In: *Basic Fundamentals of Drug Delivery*. Elsevier; 2018:369-400. doi:10.1016/B978-0-12-817909-3.00010-8

130. Yoshida A, Kaburagi Y, Hishiyama Y. Scanning Electron Microscopy. In: *Materials Science and Engineering of Carbon: Characterization*. Elsevier; 2016:71-93. doi:10.1016/B978-0-12-805256-3.00005-2

131. Hänsch TW, Kamiya GT, Krausz TF, et al. *Springer Series in Optical Sciences*. www.springeronline.com/series/624

132. Zaefferer S. A critical review of orientation microscopy in SEM and TEM. In: *Crystal Research and Technology*. Vol 46. 2011:607-628. doi:10.1002/crat.201100125

133. Sanchez SI, Small MW, Sivraramakrishnan S, Wen JG, Zuo JM, Nuzzo RG. Visualizing materials chemistry at atomic resolution. *Anal Chem*. 2010;82(7):2599-2607. doi:10.1021/ac902089f

134. Santos TG. Characterization of FSP by electrical conductivity. In: *Surface Modification by Solid State Processing*. Elsevier Ltd; 2014:153-176. doi:10.1533/9780857094698.153

135. Wu H, Gakhar R, Chen A, Marshall CP, Scarlat R. *Comparative Analysis of Microstructure and Reactive Sites for Nuclear Graphite IG-110 and Graphite Matrix A3*.; 2019. http://www.inl.gov

136. Baig MM, Gul IH, Baig SM, Shahzad F. The complementary advanced characterization and electrochemical techniques for electrode materials for supercapacitors. *J Energy Storage.Elsevier Ltd*. 2021;44. doi:10.1016/j.est.2021.103370

137. Collins KE, Collins CH, Maroneze CM, Cappovila V, Custodio R. Evaluations of the BET, I-point, and α-plot procedures for the routine determination of external specific surface areas of highly dispersed and porous silicas. *Langmuir*. 2011;27(1):187-195. doi:10.1021/la103640z

138. Rahman MM, Shafiullah AZ, Pal A, Islam MA, Jahan I, Saha BB. Study on optimum iupac adsorption isotherm models employing sensitivity of parameters for rigorous adsorption system performance evaluation. *Energies (Basel)*. 2021;14(22). doi:10.3390/en14227478

139. Ladavos AK, Katsoulidis AP, Iosifidis A, Triantafyllidis KS, Pinnavaia TJ, Pomonis PJ. The BET equation, the inflection points of N 2 adsorption isotherms and the estimation of specific surface area of porous solids. *Microporous and Mesoporous Materials*. 2012;151:126-133. doi:10.1016/j.micromeso.2011.11.005

140. Asao~ya S, ~tani. *CATALYTIC GRAPHITIZATION OF CARBONS BY VARIOUS METALS*. Vol 17.

141. Destyorini F, Irmawati Y, Hardiansyah A, et al. Formation of nanostructured graphitic carbon from coconut waste via low-temperature catalytic graphitisation. *Engineering Science and Technology, an International Journal*. 2021;24(2):514-523. doi:10.1016/j.jestch.2020.06.011

142. Zhang S, Cui Y, Wu B, et al. Control of graphitization degree and defects of carbon blacks through ball-milling. *RSC Adv*. 2014;4(1):505-509. doi:10.1039/c3ra44530e

143. Pan F, Chen T, Cai M, Wu F, You Z, Li J. Fabrication of large-surface-area graphitized carbons by potassium hydroxide-promoted catalytic graphitization. *Mater Res Bull*. 2021;140. doi:10.1016/j.materresbull.2021.111333

144. Gorbunov A, Jost O, Pompe W, Graff A. *Role of the Catalyst Particle Size in the Synthesis of Single-Wall Carbon Nanotubes*.

145. Pardanaud C, Merlen A, Gratzer K, et al. Forming Weakly Interacting Multilayers of Graphene Using Atomic Force Microscope Tip Scanning and Evidence of Competition between Inner and Outer Raman Scattering Processes Piloted by Structural Defects. *Journal of Physical Chemistry Letters*. 2019;10(13):3571-3579. doi:10.1021/acs.jpclett.9b00564

146. Eliel GSN, Ribeiro HB, Sato K, et al. Raman Excitation Profile of the G-band Enhancement in Twisted Bilayer Graphene. *Brazilian Journal of Physics*. 2017;47(6):589-593. doi:10.1007/s13538-017-0526-8

147. Herziger F, Tyborski C, Ochedowski O, Schleberger M, Maultzsch J. Tunable quantum interference in bilayer graphene in double-resonant Raman scattering. Published online December 18, 2018. http://arxiv.org/abs/1812.07305

148. Kim T, Jo C, Lim WG, Lee J, Lee J, Lee KH. Facile conversion of activated carbon to battery anode material using microwave graphitization. *Carbon N Y*. 2016;104:106-111. doi:10.1016/j.carbon.2016.03.021

149. Kap *, Yang S, Yoon YJ, Lee S, Lee WJ, Kim JH. *Further Carbonization of Anisotropic and Isotropic Pitch-Based Carbons by Microwave Irradiation*. Vol 40.; 2002.

150. Arregui-Mena JD, Worth RN, Bodel W, et al. Multiscale characterization and comparison of historical and modern nuclear graphite grades. *Mater Charact*. 2022;190. doi:10.1016/j.matchar.2022.112047

151. electrical conductivity of Graphite 2.

152. Steele R, Mata A, Dunzik-Gougar M Lou, Van Rooyen I. *Identification and Quantification of Carbon Phases in Conversion Fuel for the Transient Reactor Test Facility Nuclear Fuels and Structural Materials (NFSM-2016) Identification and Quantification of Carbon Phases in Conversion Fuel for the Transient Reactor Test Facility*.; 2016.

153. Schultrich B. Carbon. In: *Springer Series in Materials Science*. Vol 263. Springer Verlag; 2018:3-40. doi:10.1007/978-3-662-55927-7_1

154. Sánchez-González J, MacÍas-García A, Alexandre-Franco MF, Gómez-Serrano V. Electrical conductivity of carbon blacks under compression. *Carbon N Y*. 2005;43(4):741-747. doi:10.1016/j.carbon.2004.10.045

155. Fruehwald HM, Melino PD, MacLean BJ, Zenkina O V., Easton EB. Carbon materials functionalized by nitrogenous ligands for dual application in energy storage and production: Fuel cells and supercapacitors. *Electrochim Acta*. 2022;414. doi:10.1016/j.electacta.2022.140209

156. TANG S, SUN G, QI J, et al. Review of New Carbon Materials as Catalyst Supports in Direct Alcohol Fuel Cells. *Chinese Journal of Catalysis*. 2010;31(1):12-17. doi:10.1016/s1872-2067(09)60034-6

157. Dey SC, Lower L, Vook T, et al. Catalytic graphitization of pyrolysis oil for anode application in lithium-ion batteries. *Green Chemistry*. 2024;26(15):8840-8853. doi:10.1039/d4gc01647e

158. Wang CC, Chou YC, Yen CY. Hydrogen generation from aluminum and aluminum alloys powder. In: *Procedia Engineering*. Vol 36. Elsevier Ltd; 2012:105-113. doi:10.1016/j.proeng.2012.03.017

159. BATTI NR, MANDRE NR. Nickel and aluminium recovery from spent reforming catalyst through selective leaching, crystallization and precipitation. *Transactions of Nonferrous Metals Society of China (English Edition)*. 2022;32(1):345-353. doi:10.1016/S1003-6326(22)65799-6

160. Richardson JT, Scates R, Twigg M V. X-ray diffraction study of nickel oxide reduction by hydrogen. *Appl Catal A Gen*. 2003;246(1):137-150. doi:10.1016/S0926-860X(02)00669-5

161. Zhang L, Deng F, Chen X, Zhang S, Xing X, Liu Z. Catalytic role of high pressure in the graphitization of amorphous carbon. *Fullerenes Nanotubes and Carbon Nanostructures*. 2023;31(12):1171-1179. doi:10.1080/1536383X.2023.2259515